BRNO UNIVERSITY OF TECHNOLOGY

VYSOKÉ UČENÍ TECHNICKÉ V BRNĚ

CENTRAL EUROPEAN INSTITUTE OF TECHNOLOGY BUT

STŘEDOEVROPSKÝ TECHNOLOGICKÝ INSTITUT VUT

MAGNETICALLY ASSEMBLED NANOPARTICLE STRUCTURES AND THEIR EFFECT ON MECHANICAL RESPONSE OF POLYMER NANOCOMPOSITES

MAGNETICKY USPOŘÁDANÉ STRUKTURY V POLYMERNÍCH NANOKOMPOZITECH A JEJICH VLIV NA MECHANICKOU ODEZVU

DOCTORAL THESIS
DIZERTAČNÍ PRÁCE

AUTHOR — **Ing. Marek Zbončák**
AUTOR PRÁCE

SUPERVISOR — **prof. RNDr. Josef Jančář, CSc.**
ŠKOLITEL

BRNO 2018

Had I the heavens' embroidered cloths
Enwrought with golden and silver light
The blue and the dim and the dark cloths
Of night and light and the half-light
I would spread the cloths under your feet
But I, being poor, have only my dreams
I have spread my dreams under your feet
Tread softly because you tread on my dreams

William Butler Yeats

ZBONČÁK, M. *Magneticky uspořádané struktury v polymerních nanokompozitech a jejich vliv na mechanickou odezvu.* Brno: Vysoké učení technické v Brně, Středoevropský technologický institut VUT, 2018. 110 s. Vedoucí dizertační práce prof. RNDr. Josef Jančář, CSc..

……..
Signature of author

Acknowledgement

Work on this thesis was financially supported by the grant from Czech Grant Agency under the grant number: 15-18495S.
Part of the work was carried out with the support of CEITEC Nano Research Infrastructure (ID LM2015041, MEYS CR, 2016–2019), CEITEC Brno University of Technology.
Also, Brno University of Technology supported this work financially by junior student grant under number: STI-J-17-4295.

I would like to thank all the people who have participated by their effort of some kind in the process of creation of this work. I would like to thank my colleagues from CETEC, namely: Vojtech Uhlíř for discussions of magnetic properties and help with a modeling of magnetic interactions, Jiří Liška for assistance during training and measuring of magnetic properties, Ondrej Man for advices and training for SEM sample preparation, Petr Poláček for support and patience, and entire CEITEC infrastructure. I would also like to thank Mrs. Dobromila Klemová for the help with a preparation of ultra-thin sections for STEM observations, professor Jürgen Stampfl and Daniel Wagner for the opportunity to be part of their research teams during my internships at TU Wien and Weizmann Institute of Science. I would like to thank all the people who have supported me not only professionally, but mainly mentally, these people are Vladimír Šobich, Martin Sabela, Václav Štursa, Lency (the dog) and my colleagues František Ondreáš, Petr Lepcio and Klára Zárybnická. Special thanks for absolutely everything is for my brother, mother and grandmother. I would like to thank my supervisor professor Josef Jančář for his guidance, advices and outstanding experiences, for the opportunity to work in his team and for his support in difficult moments. Last but not least I would like to thank all the people who endured my nature and have not given up upon me yet.

List of Contents

Abstract

Magnetically directed self-assembly in polymer nanocomposites is studied in this dissertation thesis. Structuring of the polymer nanocomposites by application of relatively weak external magnetic fields (B=0-50 mT) has been proven to be convenient method for the control of their nano- and microstructure. The effect of the field strength, particle loading, viscosity and assembling time on the resulted structure was studied in different systems such as photopolymer, polyurethane or colloidally dispersed magnetic nanoparticles in acetone with a small amount of dissolved polymer. Self-assembled structures – without application of the external magnetic field exhibit a multi-step aggregation into nanoparticle assemblies with a complex shape. By the calculation of interaction energies between the nanoparticles, magnetic interactions were attributed to be mainly responsible for the aggregation in self-assembled systems. With an increasing magnetic field, magnetic nanoparticles are rapidly arranged into high aspect ratio one-dimensional particle chains with a homogenous orientation in the bulk polymer matrix. After prolonged assembling time, the structures gradually grow from small submicro structures to large microscopic superstructures. This method exhibits large potential to be used for controlled creation of wide variety of structures in polymer nanocomposites suitable for technological applications and/or for fundamental studies. Magnetically structured polymer nanocomposites show significant directional anisotropy of composite's stiffness at the temperatures above glass transition of the system while there is no effect on the mechanical response in glassy state. Longitudinally oriented structures exhibit much stronger effect on the composite's stiffness. Reinforcing effectivity exhibits temperature dependent course with a maximum obtained approximately 60 °C above glass transition. The structure of magnetically assembled polymer nanocomposites was described by multi-level hierarchic model of material. Micromechanics was used to address the orientation dependent reinforcement and temperature dependent stiffness of the hybrid nanoparticle-polymer structures. Load carrying capability, deformation and non-zero stiffness of the hybrid structures were attributed to be responsible for the reinforcement of the polymer nanocomposites. The presence of polymer bridges between nanoparticles transmitting the stress through the magnetic structures is proposed to be essential for the mechanical properties of polymer nanocomposites and for stiffness of the hybrid structures.

Keywords: Polymer nanocomposites, Self-assembly, Magnetic directed self-assembly, Bottom-up assembly, Aggregation, Magnetic interaction, Thermo-mechanical properties, Anisotropy, Multi-level hierarchy, Polymer immobilization, Structure-property relationships

Abstrakt

Magneticky řízené samo-uspořádávání v polymerních nanokompozitech je studováno v této dizertační práci. Strukturování polymerních nanokompozitů pomocí relativně slabých magnetických polí (B=0-50 mT) bylo prokázáno jako praktická metoda pro kontrolu jejích nano a mikrostruktury. Vliv intenzity magnetického pole, množství nanočástic, viskozity a času uspořádávání na výslednou strukturu byl studován v různých systémech jako fotopolymer, polyuretan nebo koloidně dispergované nanočástice v acetonu s malým množstvím rozpuštěného polymeru. Samo-uspořádané struktury – bez aplikace vnějšího magnetického pole vykazují vícekrokovou agregaci nanočástic do uskupení s komplexním tvarem. Magnetické interakce byly označené jako odpovědné za agregaci nanočástic v samo-uspořádaných systémech pomocí výpočtů energii mezi-částicových interakcí. S rostoucím magnetickým polem, magnetické nanočástice jsou rychle uspořádané do jednorozměrných částicových řetězů s vysokým aspektním poměrem a homogenní orientaci v polymerní matrici. S prodluženým časem uspořádaní, tyto struktury postupně rostou z malých submikrometrových struktur do velkých mikroskopických super struktur. Táto metoda vykazuje velký potenciál pro kontrolovanou přípravu široké škály struktur v polymerních nanokompozitech vhodných pro technologické aplikace a také pro fundamentální studie. Magneticky uspořádané polymerní nanokompozity vykazují značnou směrovou anisotropii tuhosti kompozitu nad jeho skelným přechodem přičemž, pod skelným přechodem systému není pozorován žádný efekt. Podélně orientované struktury vykazují větší příspěvek k tuhosti kompozitů. Efektivnost vyztužení vykazuje teplotně závislý průběh a maximum je pozorováno přibližně 60 °C nad skelným přechodem. Struktura magneticky uspořádaného polymerního nanokompozitu byla popsána vícero-úrovňovým hierarchickým modelem materiálu. Mikromechanika byla využitá k popisu směrově závislého vyztužení polymerních nanokompozitů a k popisu teplotně závislé tuhosti hybridních struktur složených z nanočástic a polymeru. Schopnost nést napětí, deformovat se a nenulová tuhost hybridních struktur je odpovědná za vyztužení polymerních nanokompozitů. Přítomnost polymerních přemostění mezi nanočásticemi, které přenášejí napěti skrze magnetické struktury je označená jako nezbytná pro mechanickou odezvu polymerních nanokompozitů a pro tuhost hybridních struktur.

Klíčové slova: Polymerní nanokompozity, Samo-uspořádávání, Magneticky řízené samo-uspořádávání, Bottom-up uspořádávání, Agregace, Magnetická interakce, Termo-mechanické vlastností, Anisotropie, Více úrovňová hierarchie, Imobilizace polymeru, Vztah mezi strukturou a vlastnostmi

1 State of Art – Introduction to topic

1.1 Self-assembly in polymer nanocomposites

Self-assembly process involves a transition of disordered components into ordered structures at various length and time scales. It is best characterized by the definition from Whitesides and Grzyzbowski (1):

„Self-assembly is the autonomous organization of components into patterns or structures without human intervention.“

These processes commonly occur in living organisms and their cells, during a macromolecular ordering or a protein crystallization, during bio-mineralization, colloidal assembly, technological processes such as nano- and microfabrication or arrangement of particles and polymers in polymer nanocomposites (PNCs) (1, 2). The research of self-assembly phenomenon is driven by the inspiration from the natural occurring processes which create complex hierarchic structures with unique properties and functions. Formation of well-defined structures with a controlled anisotropy and/or orientation composed from simple nano building blocks is in the great interest of various technological applications (3) such as electric conductors, light, thermal, electrically or magnetically responsive soft materials, soft-robotic, nanotechnology, nano/microfabrication, sensors and/or bottom-up construction of the mechanically robust biomimetic materials.

As stated in the upper quote, common self-assembly processes are driven by the interaction forces between the components in the system, such as electrostatic, magnetic, steric repulsion or van der Waals interactions (2, 4). Importantly for the definition of self-assembly, these interactions origin from the nature of the system and they are not induced or created by any external impulses triggered by the human intervention such as shear, electric or magnetic field during the assembly process. Components are simply let to reach the energetically preferable configuration and resulted structure solely depends on the delicate interaction balance between the components. The creation of the thermodynamically stable – low energetic configuration is also conditioned by the kinetic nature of the assembling process. In other words, the motion of components through the space to reach a stable configuration requires a certain period of time. Rapidly vitrified (or solidified) structures may be entrapped in non-equilibrium metastable state.

Self-assembly processes commonly take a place in technologies for the processing of the polymer nanocomposites either on the industrial or laboratory scales. Although relentless efforts of researchers, experimental control over the arrangement of nanoparticles (NPs) in the polymer matrix is not fully handled yet and “*trial-error*” approaches are usually necessary to undertake during the processing. Full understanding of driving mechanisms, equilibrium forces and kinetics aspects are the key elements to utilize the full potential of self-assembly for the fabrication of well-defined and complex structures which may pave a way for the future technological and material advance. Usually, methods based on the mutual miscibility, some

sort of phase separation governed or tuned by the chemical modification/functionalization of components seems to be the only practical tools for the structure control so far. In PNCs, three main types of NPs arrangements are distinguished in the literature: *i*) particle aggregate, *ii*) cluster and *iii*) dispersion. These structures are schematically illustrated in the Figure 1A.

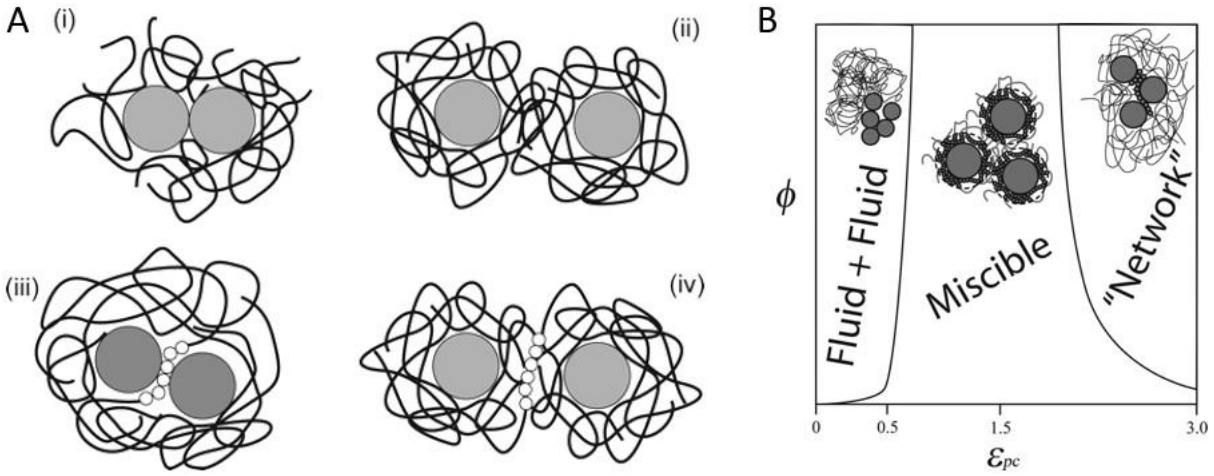

Figure 1 (A) Four structure types for PNCs distinguished by Hooper and Schweitzer: (*i*) direct contact aggregation, (*ii*) dispersion - steric stabilization with non-interpenetrating adsorbed polymer chains, (*iii*) particle bridged with one polymer segment and (*iv*) tele-bridging where adsorbed layers coexist with a long-range polymer bridging. Bridging and tele-bridging arrangements are cluster type structures. Reprinted with permission from ref. (5). Copyright 2005 American Chemical Society. (B) Phase diagram for obtained structure states in particle volume fraction (ϕ) vs. interaction strength (ε_{pc}) normalized to thermal energy (k_BT) representation. Reprinted with permission from ref. (6). Copyright 2007 American Chemical Society.

Terms cluster, aggregate and agglomerate are commonly freely interchanged in the scientific literature. Basic difference between these structural variations needs to be addressed for clarification. It may be needed further in this work. Term "*aggregate*" is used for the strongly joined primary particles by direct particle-particle contacts (Figure 1A*i*). "*Agglomerate*" is on the other hand higher hierarchical structural level composed from the individual loosely bound aggregates either by direct aggregate-aggregate contact or spaced by polymer chains. The interconnection of the aggregates in backbone of the agglomerate is usually considered as much weaker than stabilizing forces in the aggregate. Agglomerates can be thus reversibly broken for example by application of moderate shear forces (7). The breakdown of the particle aggregates is more complex problem. In the case that aggregate falls apart by the application of the external force, the particle dispersion is stable only for limited period of time when the stimulus is maintained. After its removal, particles aggregate rapidly. The aggregation results from the unfavourable chain adsorption onto the particle surface due to weak polymer-particle interactions. Both, particle-particle and polymer-polymer interaction strengths are much stronger than their polymer-particle combination. In such case, polymer chains and NPs rather tend to keep together and phase separate. The concentration of the polymer locally increases

which promotes the aggregation of the particles by pressure of the surrounding polymer coils – so called polymer-depletion attraction.

Hooper and Schweizer developed the polymer reference interaction site model (PRISM) to predict an interparticle potential mean force on hard spheres incorporated into polymer melts (5, 6, 8, 9). Various parameters such as particle to monomer size ratio, particle volume fraction, degree of polymerization – molecular weight, van der Waals attraction, monomer-particle interaction strength (ε_{pc}) and range of these interactions have been studied by the authors. Polymer-particle interaction strength plays the most crucial role for resulted structure (Figure 1B). The mutual attraction between the polymer chains and NPs surface is essential for good and stable dispersion of NPs in the bulk (Figure 1A*ii*). Polymer segments interact via different physico-chemical interactions with a surface and large number of the polymer segments may remain anchored on the surface (10). Adsorbed chains may occupy different conformations resulting in modification of the polymer coil radius, chain dynamic and relaxation times as a function of interaction strength and distance from the surface reaching as far as couple of nanometres from the solid surface (11-13). Development of such polymer shell is pivotal for stable dispersion due to steric repulsion of polymer segments shielding direct particle-particle contact (14).

Clusters are assemblies of primary particles with spacing polymer chains creating a bridge between two (or more) particles and preventing their solid contact (Figure 1A*iii, iv*). Polymer chains may occupy flattened or straightened conformation confined between the particle surface. Whole nano scaled cluster can be idealized by single rigid inclusion of higher hierarchy transmitting the stress via bridge stretching. Particles can be bridged via single chain (Figure 1A*iii*) while tele-bridging occurs at longer distances between dispersed particles with sufficiently long chains that can interconnect multiple particles and can be a part of multiple adsorbed layers (Figure 1A*iv*).

Steric stabilisation seems to be an effective method to govern the NPs organisation and dispersion. Low molecular weight organic molecules, such as fatty acids, siloxanes and/or macromolecules with higher molecular weights either covalently bonded or physico-chemically adsorbed onto NP's surface can be employed. Grafted molecules create a shell of different compressibility which repeals other shells due to entropic effect and preventing direct NP-NP contact. Surface density of grafts, their molecular weight and molecular weight of host polymer matrix seems to be controlling parameters for PNC structuring (*15*). Akcora et al. (*16*) controlled the structure of PNCs by varying the parameters of grafting and matrix molecular weight in the system composed from polystyrene (PS) grafted silica nanoparticles and PS matrix. Wide range of different iso- and more anisotropic particle assemblies such as chains, sheets, dendrites or strings were formed in the PS melt during annealing (Figure 2A-C). In addition, fairly well agreement between the experiments and simulations has been found for this system and phase diagram for the observed structures is in Figure 2D. However, reaching the thermodynamic equilibrium seems to be kinetic process which lasts couple of days at the

temperatures far above T_g of the matrix as the result of slow diffusion of grafted NPs in high viscous polymer melt.

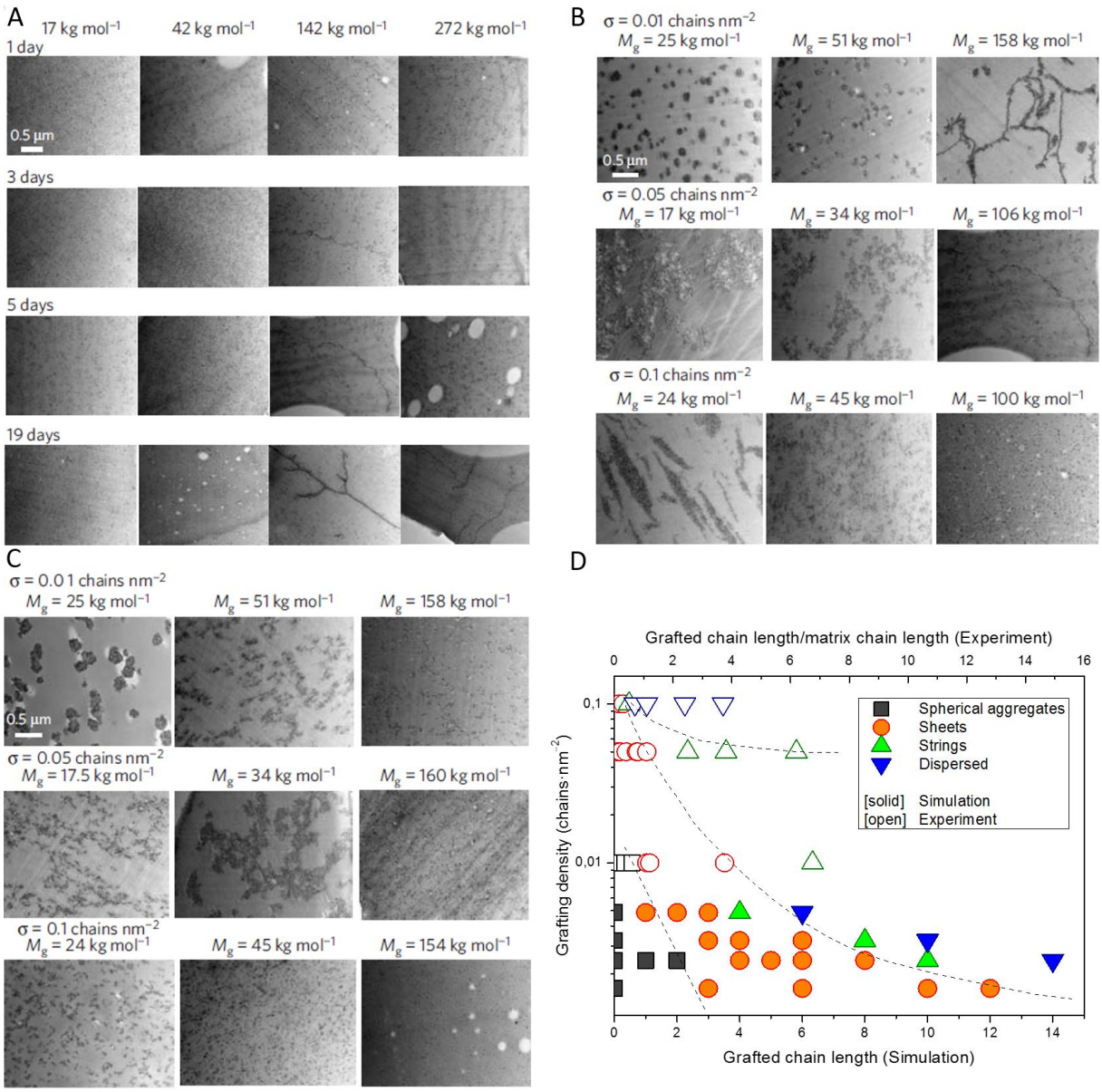

Figure 2 TEM micrographs of PS filled with 5 wt. % of PS-grafted silica nanoparticles. (A) Time evolution of structure from 1-19 days after annealing at 150 °C in the PS matrix with M_w=17-272 kg/mol, graft molecular weight M_g=106 kg/mol and grafting density σ=0.05 chain/nm^2. Structure of PS grafted silica nanoparticles after 5 days of annealing at 150 °C in PS matrix with a molecular weight (B) 142 kg/mol and (C) 42 kg/mol as a function of grafting density (σ) and graft's molecular weight (M_g). Reprinted by permission from Springer Nature (16) Copyright 2008. (D) Phase diagram for the experimentally obtained and simulated structures as a function of grafting density and graft length, data acquired from the ref. (16).

Common processing protocols for the PNCs employ a melt or liquid state processing (17-20). Traditional melt processing technologies, for example injection moulding, extrusion or calandering are industrially preferable due to fast processing cycles but extent of the particle dispersion is rather worse when compared to liquid routes (21). Also, the addition of NPs may

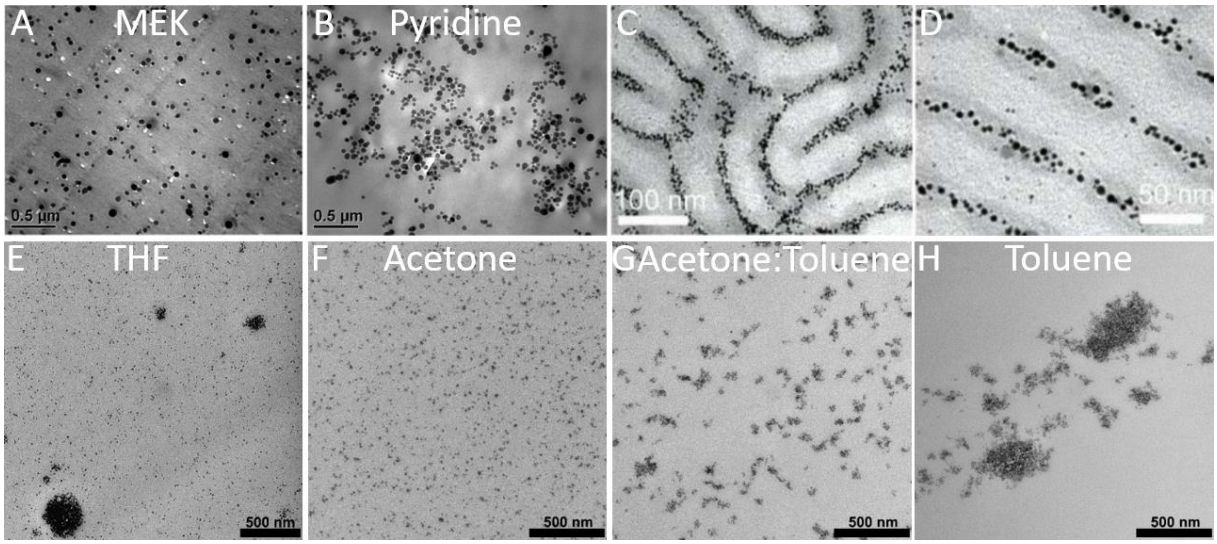

Figure 3 TEM micrographs of 10 wt. % of 50 nm bare silica NPs in P2VP prepared by solvent casting method using (A) MEK and (B) pyridine. Reprinted with permission from ref. (14). Copyright 2014 American Chemical Society. (C,D) TEM micrographs of PS-b-P2VP/Au nanocomposite annealed under vacuum at 170 °C for 30 min. and quenched. Reprinted with permission from ref. (22). Copyright 2008 John Willey and Sons. TEM images of PMMA PNCs filled with 1 vol.% of nanosilica with various structures prepared by solution blending method from: (E) THF, (F) acetone, (G) acetone-toluene 1:1 mixture and (H) toluene. Reproduced from ref. (23) with permission from The Royal Society of Chemistry.

increase the viscosity of the polymer melt beyond the processing capacity. Low viscous wet methods such as solution blending/casting and/or *in-situ* polymerization in the bulk offer more options for the control of the spatial arrangement of the components and ability to add different processing chemicals dispersible at a molecular scale and relatively low temperatures. In addition, selection of proper solvent/dispersion medium has been proven to be important controlling parameter for achieving of desired structure. Jouault, et al. (14) achieved control over the spatial organization of bare silica nanoparticles in poly(2-vinylpyridine) (P2VP) based on two different solvents – methyl ethyl ketone (MEK) and pyridine with a resulting aggregated structure in pyridine (Figure 3A) and dispersed NPs in MEK (Figure 3B). Authors proposed that absence of P2VP layer on the silica NPs in the pyridine solvent and consequently no steric stabilization led to gradual aggregation of NPs. Zhao, et al. (24) proposed that creation of adsorbed layer is a result of delicate interplay between polymer-NP and solvent-NP interactions. And it may result in more favoured adsorption of solvent molecules rather than polymer chains. The interplay between the components was also studied by Lepcio, et al. (23) and showed that polymer-NP and solvent-NP enthalpy of Lewis acid-base (donor-acceptor) adsorption can be used as a controlling parameter for the successful governing of the NPs arrangement in PNCs. Chemical composition of PMMA and silica NPs was kept constant while using of different solvents (tetrahydrofuran, acetone, ethyl acetate and toluene) resulted in creation of different structure types (dispersion, aggregates, clusters or their combination) which are shown in Figure 3E-H. Mackay, et al. (25) also proposed an important effect of

diameter ratio between NP and polymer coil on the NP dispersion. This mechanism is most probably valid for systems with weak interactions (authors studied fullerenes in nonpolar polymer and cross-linked PS particles in PS matrix). Despite beneficial usage of solutions and liquid states in controlling of the PNC's structure, removing of solvents or free monomer is slight drawback requiring additional technological precautions.

Using of block copolymers or polymer blends of defined architectures is an elegant method for nanofabrication. Various lamellar, cylinder, island-like, rod-like, etc. domains with nano scale geometries are composed from individual chain segments. The creation of such morphologies is driven by molecular immiscibility of the individual polymers resulting in their nanoscale phase separation. Incorporation of NPs with a specific affinity to certain chain segments into such materials results in NPs separation and dispersion according to higher affinity. NPs can be distributed on the polymer phase interfaces or dispersed in individual polymer block domains. These methods were reviewed in detail for example by Kao, et al. (26) and representative example of PNC with Au nanoparticles dispersed in PS-b-P2VP block copolymer can be seen in Figure 3C,D (22). Au nanoparticles are distributed in P2VP domains.

1.2 Directed self-assembly

Assembling of nano building blocks into anisotropic assemblies attracted a large attention due to possible utilization of these structures in nano and micro fabrication (2, 3, 27, 28). In comparison with traditional self-assembly methods employed during processing protocols of PNCs, directed self-assembly methods exhibit a much controllable structuring of the material and its nano- and micro morphology. An impulse of external stimulus such as electric or magnetic field is utilized for the induction of unique driving forces between the responsive components. These forces guide the building blocks into defined structures built in bottom-up way (29, 30). Directed self-assembly (or force assembly) can be defined by slight modification of self-assembly definition from the first chapter as follows:

Directed self-assembly is the autonomous organization of components into patterns or structures with human intervention.

Newly induced forces considerably overcome naturally existing interactions between the components, they dominate the particle assembly and govern the structure formation at technologically viable time scales. Sufficiently strong response to the external stimulus and dipole moment (electric or magnetic) is essential. Responsive blocks can diffuse along the field gradient into areas of the highest intensity – electro/magnetophoresis used for the separation methods (31, 32). While, keeping the field gradient zero or negligibly small, responsive building blocks tends to assemble into anisotropic geometries along the imaginary force lines. Large quantity of the fundamental studies has been done mainly dealing with dipolar microparticles or nanoparticles dispersed in colloid systems.

The *in-situ* synthesis of NPs in presence of the polymer or its monomers while simultaneous directing of their self-assembly is promising method for new generation of the materials.

1.2.1 Electric directed self-assembly

For the electric directed self-assembly, particle polarization can be induced by large mismatch in dielectric properties of particle and environment (33). As well electric charge on the surface of particles can be source of strong electric response (such as ions or charge of the double layer). For this purpose, different organic surfactants and electrolytes are used. For example, PS (34-36), PMMA (37) or silica (34, 38) micro and sub-micro particles were used for creation of particle columns in the electrolyte solutions. Gangwal, et al. (39) synthesized specifically responsive Janus PS microparticles with a response to the electric field only via one Au coated hemisphere of the particle. Similar methods utilize mainly conductors such as metals which are extremely sensitive to electric field (40). Anisotropic particles, such as metal rods (41), carbon nanotubes (CNTs) (42-48) or graphene (44, 49) rotate along the field direction and assemble into chain-like structures with a specific orientation controlled by the field direction and strength. Another interesting method is directed electrochemical assembly which utilizes a redox type reaction from the electrolyte solution (for example containing $PtCl_6^{-2}$) for synthesis of dendritic metal assemblies growing on the surface of electrodes (50-54).

1.3 Magnetic field directed self-assembly

As shown in the previous chapter, interest of researchers and engineers in self-assembly and directed self-assembly methods scales up significantly due to enormous importance of these processes in technological applications. Alongside the electric field, magnetically directed self-assembly is one of the most convenient methods for the rapid assembling of magnetic nanoparticles (MNPs) into wide range of structures. This approach represents very promising method for bottom-up micro and nanofabrication of well-defined, homogenously aligned and regularly packed (superlatticed) nano- and micro structures.

1.3.1 Physics of magnetically directed self-assembly

Generally, different sources of the magnetic field are used by researchers as the source of the external force stimulus with various strengths (55, 56). Magnetic fields with an induction (*B*) in the range of miliTeslas are reported to be strong enough to trigger the particle assembling. But this depends on multiple parameters such as particles magnetic response, viscosity of environment or thermal energy (31). Field can be generated either by permanent magnets or by electromagnets, such as solenoids, Helmholtz or Maxwell coils working in AC, DC or pulsation regimes. In the case of air solenoid, which is the simplest electromagnet used in the fundamental works, the strength of the field (*H*) can be conveniently controlled by applied electric current. In the case of permanent magnets, the intensity can be controlled only by distance from the magnet surface with high gradients of the magnetic field strength. On the other hand, permanent magnets generate relatively strong magnetic fields which may be more difficult task for the common laboratory scale electromagnets.

Sufficiently intense ordering of magnetic moments limits the usage of this assembling method only for close group of magnetic materials. Magnetic properties of the material and its response to the application of the external magnetic field is defined by the magnetic susceptibility (χ). This parameter reflects repulsive or attractive interaction of the matter with an external magnetic field as well the extent of the magnetic ordering and magnetic response – magnetization as a function of external field strength. Equation (1) defines a relationship between volume magnetization and external magnetic field strength and/or field induction (57, 58). The slope of this function defines susceptibility of material (see also Figure 4A).

$$M_{\mathrm{V}} = \chi_{\mathrm{V}} H = \chi_{\mathrm{V}} \frac{B}{\mu} \qquad \text{Equation (1)}$$

Diamagnetism is typical for materials with $\chi_{\mathrm{V}}<0$ such as for example for organic substances and polymers, paramagnetism for substance with $\chi_{\mathrm{V}}>0$ and ferro-, ferri- and superparamgnetism for $\chi_{\mathrm{V}}>>1$. In other words, materials with $\chi<0$ are repealed from the magnetic field while materials with $\chi>0$ are attracted by the field. The macroscopic magnetic response and the ordering of magnetic moments of these materials in external magnetic field is schematically depicted in Figure 4. In this field of research, cobalt, iron, nickel, ferrites, iron oxides nanoparticles are the most common building blocks with a strong magnetic response to the external magnetic field.

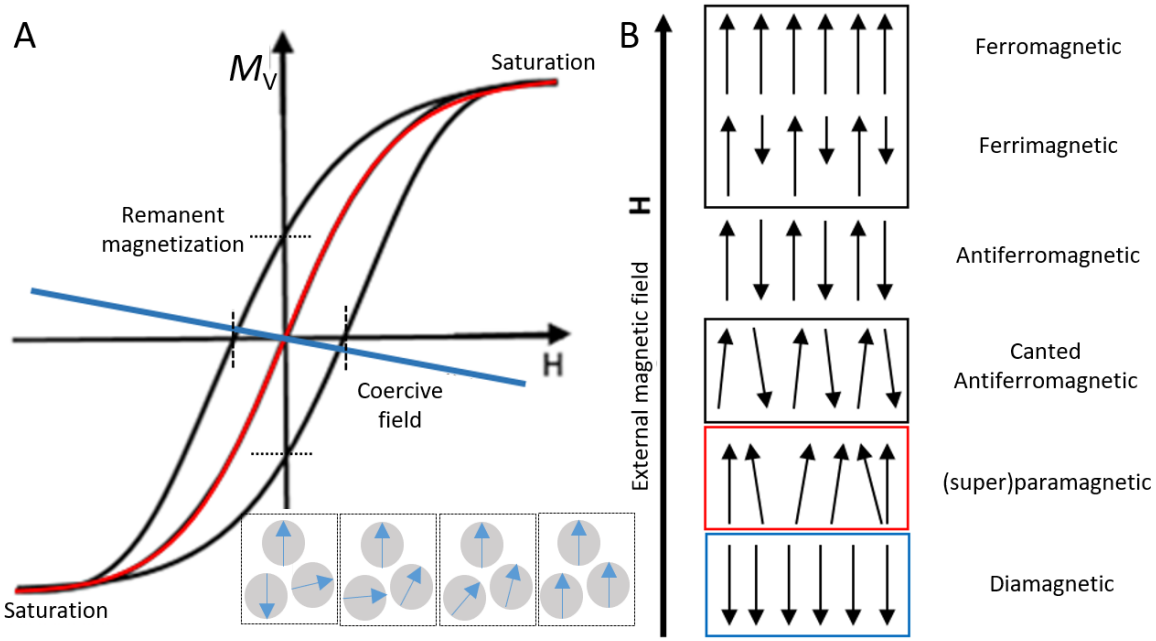

Figure 4 (A) Typical hysteresis curves for various types of magnetic materials with a schematic depiction of magnetic moments orientation in increasing external field (*H*) followed by the increase of macroscopic magnetic response – volume magnetization (M_V). (B) Magnetic domain ordering in the magnetic materials in non-zero external magnetic field. Colour lines in the plot (A) correspond to colour frames of the magnetic structures in (B).

Individual MNP represent a magnetic dipole consisted from the north and south pole (Figure 5A). Each dipole is surrounded by its magnetic field imaginary visualised by the enclosed magnetic force lines passing through the space. The highest intensity of the magnetic field strength is in very proximity of dipole's surface and decreases with a distance from the dipole. Adjacent magnetic dipoles interact with each other via their magnetic fields and assemble into complex structures, see Figure 5B-D. Overall magnetic moment of the particle aggregate or cluster of multiple MNPs is calculated as a vector summation of individual moments. Both, individual dispersed particles and complex particle assemblies will be termed as magnetic building blocks. Magnetically active blocks undergo various types of motions in the space such as:

1. The Brownian rotation of whole magnetic building block to align the magnetic moment parallel with a direction of the external magnetic field (59, 60). The orientation of magnetic moment inside the atomistic structure of MNP is controlled by magnetocrystalline anisotropy which defines the energetically preferable or un-preferable alignment of the magnetic moment in specific crystallographic axis – so called magnetic easy or hard axis (58, 61-64).

2. Translation motion caused by the interparticle magnetic forces (65) which can attract or repulse other building blocks (Figure 5B,C). In other words, opposite magnetic poles attract each other while identic poles exert the repulsion. Attractive or repulsive potential between magnets is a function of angle (θ) between a line joining centers of two interacting particles and vectors of their magnetization. These delicate interaction forces drive the assembly of the

particles into anisotropic particle assemblies. The angle $0°<\theta<54.09°$ is boundary for attractive interaction and $54.09°<\theta<125.91°$ boundaries the repulsive interaction between magnets. The situation is schematically illustrated in Figure 5. The energetic potential of magnetic interaction between two magnetic building blocks is derived in Equation (2) (4, 58, 66, 67).

$$U_{\mathrm{mag}} = \frac{\mu_0 M^2}{4\pi l^3}(1 - 3\cos^2\theta) \qquad \text{Equation (2)}$$

Where μ_0 is the permeability of environment (for vacuum, $\mu_0 = 4\pi \cdot 10^{-7}$ H·m^{-1}), M is the magnetic moment bear by particles, l is their center-to-center distance and θ is the angle between direction of their magnetization moment and line connecting their centers.

3. Magnetophoretic flow of the particles is caused by the gradient of magnetic field intensity (heterogenous magnetic fields) causing particles to diffuse to the area with the highest magnetic intensity such as surface of the permanent magnet (68, 69).

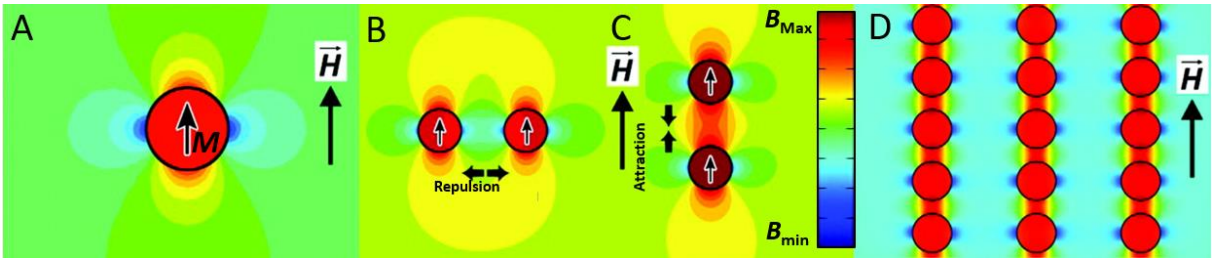

Figure 5 Simulation of (A) magnetic field around a magnetic nanoparticle. (B) Repulsive and (C) attractive interactions between magnetic dipoles driving them into (D) one-dimensional particle assembled. Colour bar shows a relative strength of local magnetic field. Reprinted with permission from (70). Copyright 2012 American Chemical Society.

1.3.2 Structure formation in magnetic fields

Usage of different types of MNPs of various sizes and shapes, stabilization methods, solvents, drying conditions, application of low, high or extremely high magnetic field was reported in the relative rich literature. Various structural assemblies are reported as well such as loops (*71, 72*), spicules (*73, 74*) or star-like assemblies (*75*). However, the most frequently reported structural morphology of the magnetic assemblies is one-dimensional high aspect ratio structure (chain like/string like/fiber like structures) (*76-83*). Two and three-dimensional superstructures can be formed under certain conditions. Ordering of magnetic building blocks and gradual transition from colloid dispersion into one-, two-, and three-dimensional superstructures was proposed to be mainly controlled by the field strength and particle concentration (55). The schematic depiction of the transition from the homogeneous dispersion to one-, two- and three-dimensional assemblies is illustrated in Figure 6A. Also, experimental examples of such structures from the literature are shown in Figure 6B-E. Although, this approximation seems to be valid only for highly stable, well dispersed, homogeneous systems dispersed in low molecular and low viscous environments and it appears that far more parameters are important for the structure control. Structural features of magnetic assemblies are highly dependent on number of energetic factors and parameters more impacting the kinetics of assembling, such as:

1. Susceptibility of magnetic building blocks
2. Strength, shape and gradient of magnetic field
3. Particle concentration and inter particle distance
4. Shape, size and size distribution of assembling blocks

} Energetic factors

5. Viscosity of environment
6. Assembling time

} Kinetic factors

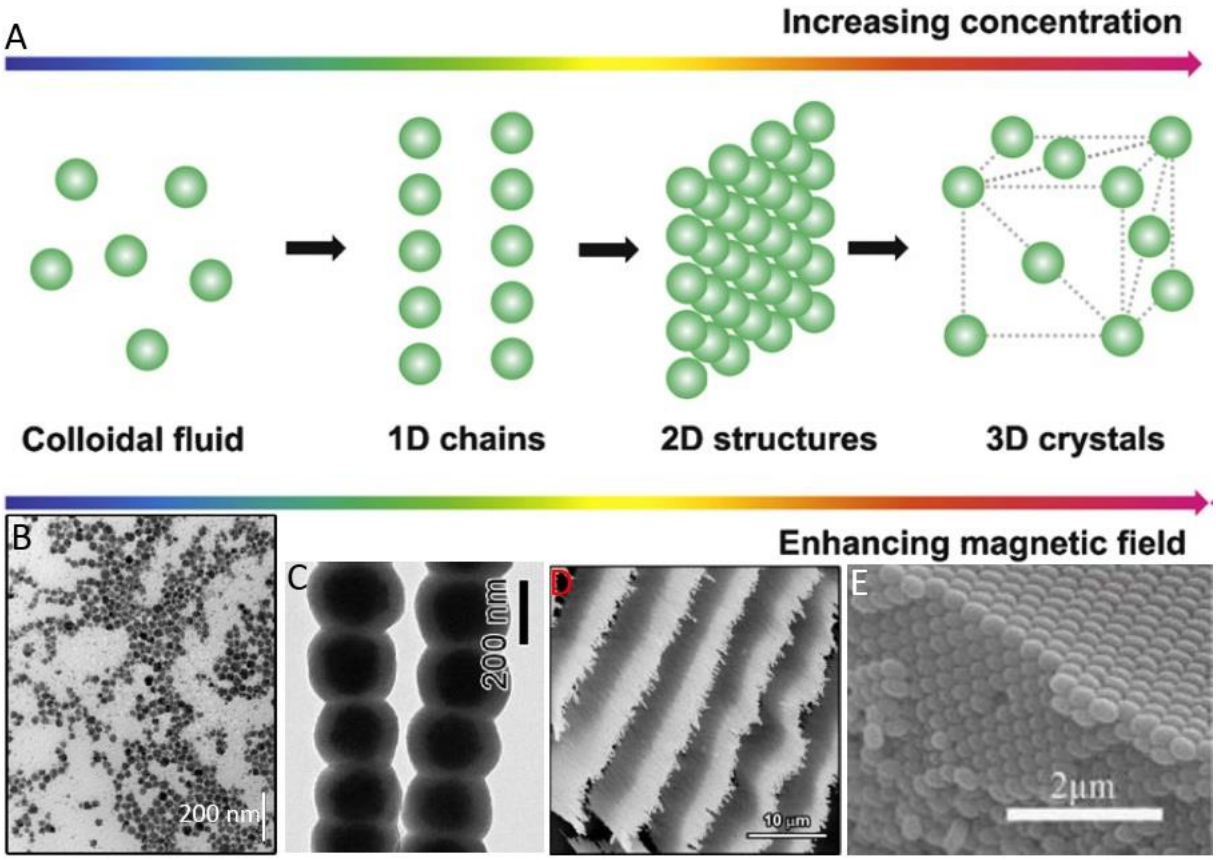

Figure 6 (A) Schematically depicted transition from colloidal system into anisotropic particle assemblies with an increasing particle concentration and/or magnetic field strength. Reprinted from ref. (*55*), Copyright (2013), with permission from Elsevier. Experimental examples of (B) colloid self-assembled structure, reprinted with permission from ref. (*84*), Copyright 2007 John Willey and Sons; (C) one-dimensional structure, reprinted with permission from ref. (*85*), Copyright 2011 John Willey and Sons; (D) two-dimensional structure, reprinted with permission from ref. (*86*), Copyright 2011 American Chemical Society; and (E) three-dimensional structure, reprinted with permission from ref. (*87*), copyright 2009 John Willey and Sons.

Various theoretical simulation methods were utilized in the order to understand the influence of various processing parameters on the assembling process of magnetic nanoparticles and the resulted morphology of their assemblies. Extensive simulation studies were done by the research team from the references (*88-95*). Parameters such as temperature, magnetic moment,

field strength, particle concentration (density of system), dimensions of assembling chamber were studied by Monte Carlo simulations. Cobalt nanoparticles with a diameter, d=10 nm and bulk magnetization M_V=14·10^5 A·m^{-1} were used as model particles. An important phase diagram for the transformation of the structures assembled in the external magnetic field is provided in Figure 7A. Diagram shows the transition from the one-dimensional particle chains into two-dimensional sheets and consequently forming the continuous magnetic films with an increasing number of particles in the system (density). In sufficiently strong magnetic fields, additional densification of structures leads to formation of the voids in the MNP film. Also, two-dimensional configurations can be occupied also if diameter of one-dimensional chain cannot fit the chamber height (*92*), the structure is then confined into elliptical shapes. These theoretical results are in good agreement with numerous experimental observations (*81*, *93*, *96-103*).

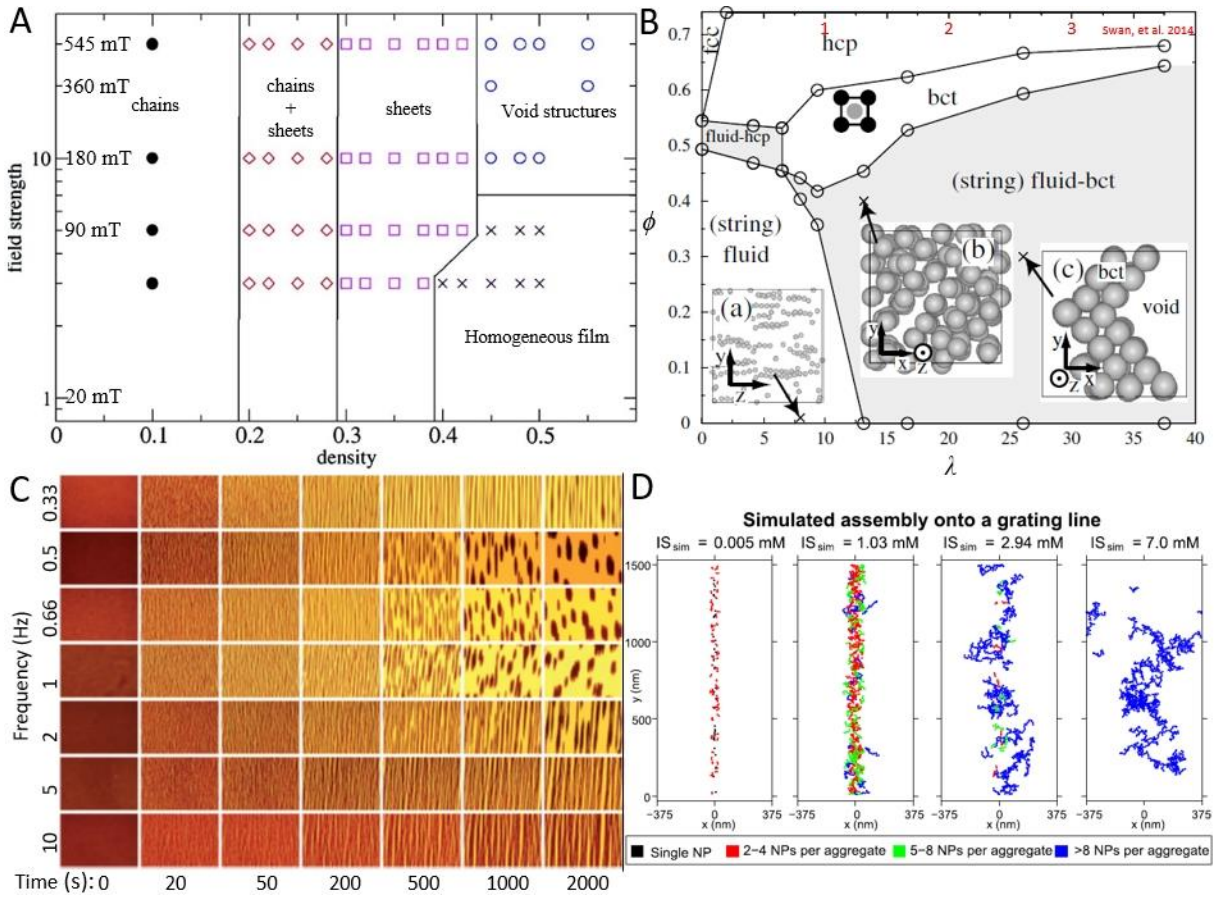

Figure 7 (A) Structural phase diagram for dipolar assemblies in reduced units of field strength vs. density of system representation. Reprinted figure with permission from ref. (*93*). Copyright 2009 by American Physical Society. (B) Phase diagram for particle packing in the dipole moment strength (λ) vs. particle volume fraction (ϕ) representation. Reprinted figure with permission from ref. (*104*). Copyright 2005 by American Physical Society. Red values at top x-axis in (B) of dipolar strength from Swan, et al. (*105*). (C) Time evolution of structure under pulsation magnetic field. Reproduced from ref. (*105*) with permission from the Royal Society of Chemistry. (D) Simulation of magnetically assembled building blocks of various aggregation morphologies. Reprinted from ref. (*106*) under open license, Copyright 2016 Springer Nature.

Hynninen and Dijkstra (*104*) used Monte Carlo simulation for the equilibrium packing of well dispersed homogeneous dipolar spheres responsive to stimulus of external electric or magnetic fields. Dimensionless strength of dipolar interactions normalized to thermal energy (λ – dipolar/thermal energy), determines the extent of the external field on the formation of the anisotropic structures. Dipolar strength (λ) and particle volume fraction (ϕ) were used as scaling parameters in equilibrium phase diagram. The diagram shows specific packing of the hard spheres within the one-dimensional string-like particle assemblies and their super latticed structures (Figure 7B). For dipolar strength $\lambda>1$, thermal diffusivity is supressed by dipolar interactions which govern the assembling process and stabilize the structure. Swan, et al. (*105*) later studied the kinetics of assembling of paramagnetic iron oxide coated PS latex particles in pulsed magnetic fields with toggling frequencies 0.33-10 Hz. Assembled particle chains gradually merge laterally and coarse the system with an increasing time (Figure 7C). In the specific frequency rage (f=0.5-2 Hz) two–dimensional ellipsoid assemblies were formed which were previously observed also by Promislow and Gast (*107*). With an increasing frequency (and thus decreasing time in field off state) structures tends to remain in linear structure regime.

The undisputable importance of the homogeneity of particle shapes, narrow particle size distribution, sufficient level of dispersion quality and stability needs to be stressed out for the creation of highly ordered superstructures with super latticed particle packing (*104, 105, 108*). The most convenient method for stabilization of MNPs in colloids is based on using of fatty acids or their salts, but also other methods are widely used such as grafting of the MNPs with polymer chains.

Keng, et al. (*109*), Hill and Pyun (*110*) created mono-particle wide nanochains interconnected by the products of surface oxidation of Co nanoparticles. Their surface stabilization by the grafting with PS chains was used to yield stable dispersion of MNPs in 1,2-dichlorobenzene. Particles were assembled in field free state by dipolar interactions due to their non-zero remanent magnetic moments. These randomly oriented particle nanochains exhibit electric conductivity and showed potential for designing of electrically conductive nano pathways. Similar approach was used for creation of $CoSe_2$ nanochains by Gao, et al. (*83*).

Several very interesting methods for synthesis of magnetic building blocks, their stabilization and controlled assembling into photonic active structures have been developed by the team of researchers from the references (*55, 70, 111*). Spherical aggregates with a diameter ranging from 30 to 180 nm and composed from individual Fe_3O_4 nanoparticles were stabilized by the layer of poly(acrylic acid) or siloxane layer (*84*). Later, siloxane surface treatment of Fe_3O_4 spherical aggregates (in their work denoted as CNCs – colloidal nanocrystal clusters) was used for surrounding of the CNCs and preventing from their direct contact with a hundreds of nanometer thick siloxane layer (*85*). After certain period of a time, magnetic field was switched on to align the aggregates into chains. Siloxane surface layer progressively glued the aligned aggregates into stable one-dimensional particle chains (Figure 6C). Magnetically responsive colloids exhibit structural coloring (*112*) due to diffraction of the light on the periodically

arranged nanochains in colloids (*85, 113-116*) or plastic films (*117, 118*). Further, they also used micro magnetic arrays to assemble coated Fe_3O_4 nanoparticles into photonic one-dimensional nanochains (*119, 120*) as well two-dimensional sheets perpendicularly standing on the micro magnetic island template creating two-dimensional labyrinth-like structures formed by zig-zag lateral merging (Figure 6D) (86).

Assembling of oleic acid (OA) stabilised γ-Fe_2O_3 nano cubes during solvent evaporation under application of the magnetic field into regular three-dimensional micro mesocrystals was studied by Taheri, et al. (*121*), Ahniyaz, et al. (*122*) and Chen, et al. (*123*). Particles were assembled from the stable MNPs dispersion and deposited on the TEM grid placed between two permanent magnets. Nanocubes are perfectly face to face packed into three dimensional cuboids (Figure 8A), nano-ribbons and/or chain-like superstructures with a sub-micro and micrometer size.

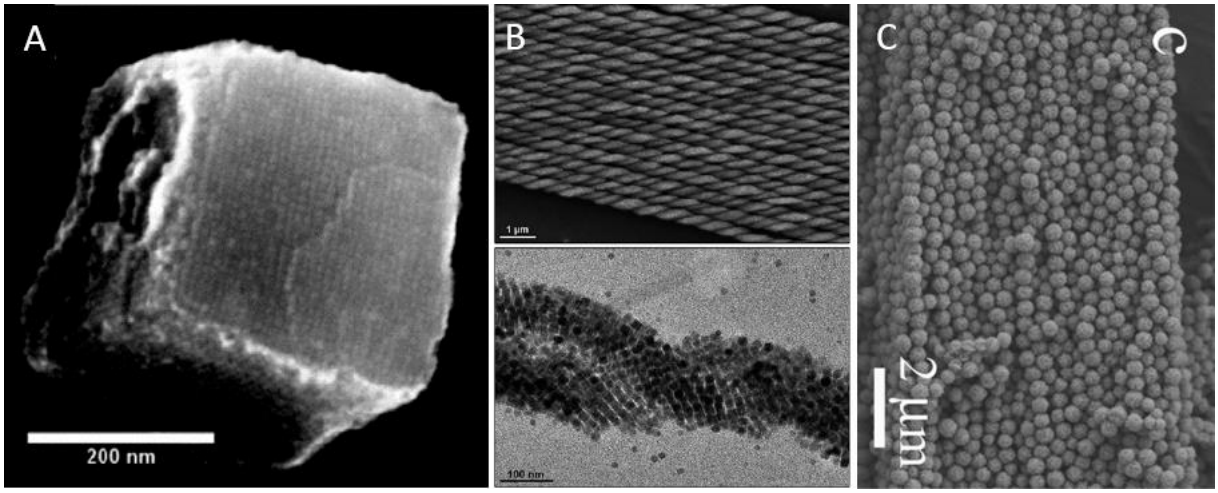

Figure 8 Magnetically assembled superlatticed superstructures. (A) SEM image of three-dimensional cuboid which consists from more than 10 000 cubic γ-Fe_2O_3 nanoparticles (8.2 nm). Reprinted with permission from ref. (*121*). Copyright 2015 National Academy of Sciences. (B) Scanning and transmission electron micrograph of helical superstructures assembled in magnetic field from 13 nm cubic Fe_3O_4. Reproduced from ref. (*124*) with the permission from Royal Society of Chemistry. (C) Hierarchic bottom-up assembled three-dimensional superstructure from the ‘‘walnut-like’’ γ-Fe_2O_3 aggregates with hexagonal packing. Reprinted from the ref. (*125*), Copyright 2015, with permission from Elsevier.

Singh, et al. (*124*, *126*) studied a similar system based on the assembling of OA stabilised Fe_3O_4 nano cubes in hexane and assembled at diethylene glycol-air interface. Magnetic field strength and particle concentration seem to be controlling parameters for the creation of single, double and/or triple helix superstructures (Figure 8B). Lower particle concentration tends to yield the chains of face to face connected nanocubes while helices are created at higher particle concentrations.

Tang, et al. (*125*) *in-situ* synthesized γ-Fe_2O_3 from the water solution of NP’s precursors in the presence of relatively strong magnetic field (0-0.4 T). Bottom-up hierarchic assembling of the magnetic building blocks proceeded during the synthesis consisted from aggregation of the

primary maghemite particles into ‘‘walnut-like’’ aggregates which further assemble into sub-micro spherical structures and these are further hexagonally or face to face packed within the chains, sheets and three-dimensional superstructures controlled by the strength of the field (Figure 8C).

In contrary to fancy superlaticed structures, literature more frequently reports on the formation of irregular structures with a random particle packing (*67, 77-81, 93, 96-102, 127-129*). Example of the microstructures with a random packing of the magnetic nanoparticles can be seen in Figure 9. Phase diagram for dipolar spheres constructed by Hynninen and Dijkstra exhibits also a region of string-like particle assemblies without specific particle packing inside the structures. This region is observed at low particle concentrations and dipolar energies – marked as fluid (Figure 7B). In the addition to particle concentration and dipolar energy guiding the assembling, the shape homogeneity of the building blocks is extremely important parameter (*91*). Previously mentioned experimental results only underline its importance. The role of homogeneity of the magnetic building blocks – size and shape on their packing was studied by Ye, et al. (*106*). Single NPs and aggregates composed from closely connected nanoparticles (more than 8 NPs per aggregate) were used as building blocks in the simulations. Here, the shape perfection and regularity of resulted structure assembled in magnetic field highly depends on the shape and size of the magnetic building block (Figure 7D). Aggregates with more random and irregular shape tends to ultimately yield branched structures with a random packing of building blocks along the chain length. This effect was experimentally observed in various colloid systems (*67, 77-81, 128-130*) suggesting that sufficient dispersion and stability of nanoparticles in initial colloid is one of the most important parameters controlling the packing of building blocks and structural parameters of resulted particle formation in the external magnetic fields.

Bharti, et al. (*67*) came up with an interesting approach of binding of assembled magnetic nanoparticles by capillary brides and preserve the assembled structure also in the field free state. Magnetic field is used for assembling of magnetic aggregates into well oriented one-dimensional particle microchains (Figure 9A). After the field removal, structures tend to curve/fold by viscous drag and/or Brownian motion but structure still holds together without disintegration. This is achieved by the fatty acid capillary bridges holding particles together. Increase of temperature above melting or glass transition of fatty acid layer on the particle surface is an important parameter. Solid like capillary bridges (bellow temperature of softening) can maintain the rigidity of the structures in viscous medium, while structures lose the rigidity above temperature of softening of the fatty bridge. Next, authors showed mechanic rupture of micro chains by sharp stylus (Figure 9B) and chain reconfiguration in water solution by the application of magnetic field (Figure 9C).

Outlined results give a great promise for usage of similar mechanisms in soft intelligent materials, gels and liquids. Commonly, guidance of MNPs by the external magnetic field is used in various biomedical applications such as separation, drug delivery, therapy and/or

imaging (*131, 132*). However, controlled deposition of magnetic material and creation of anisotropic objects might be utilized with a great promise in tissue engineering. Various authors already combined magnetic assembling with biologic material and cells. For example, Schenkel, et al. (*129*) used this approach for assembling of organic amphiphilic cyclodextrins vesicles, Li, et al. (*133*) magnetically assembled DNA decorated magnetic nanoparticles into one-dimensional chains, Choi, et al. (*134*) transported cells by Ni nanowires, Ghosh, et al. (*135*) templated magnetically decorated human prostate cancer epithelial cells into cell clusters and Souza, et al. (*136*) utilized magnetic NPs for magnetic levitation of filamentous bacteriophages.

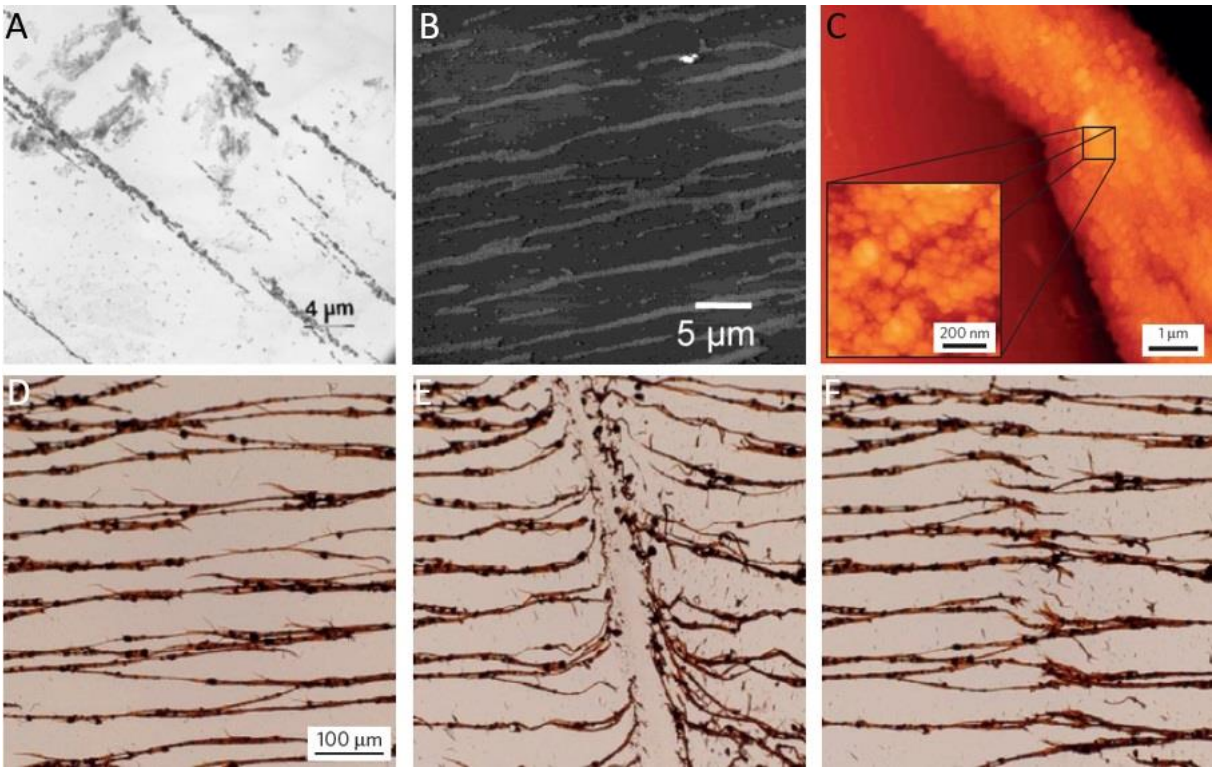

Figure 9 One-dimensional micro magnetic structures with a random particle packing within the structures. (A) Nanobands assembled from Au coated iron nanoparticles under magnetic field 0.5 T. Reprinted by permission from ref. (*78*). Copyright 2001 Springer Nature. (B) Atomic force microscopy (AFM) image of oriented magnetite particle chains assembled under magnetic field 0.8 T. Reprinted with permission from ref. (*80*), Copyright 2004 American Chemical Society. (C) The AFM scan of the particle structure of magnetically assembled fatty acid treated γ-Fe_2O_3 nanoparticles from colloid suspension. Inset shows a higher magnification. The magnetic structures (D) before, (E) after mechanical fracture by sharp stylus (both in absence of magnetic field) and (F) self-repaired structures after repeatable field application as observed in the view field of optical microscope. Reprinted by permission from the ref. (67). Copyright 2015 Springer Nature.

1.4 Magnetically directed self-assembly in polymer composites

The structure formation in polymer melts/liquids by common self-assembly processes was outlined in more detail in first chapter (1.1 Self-assembly in polymer nanocomposites). Despite relentless attempts of researchers, common isotropic particle assemblies are typical output of their efforts – dispersion, clusters, aggregates. The structuring of nano and microstructure of PNCs is in great interest of the researchers due to believe that different particle organization yields different functional and mechanical properties of PNCs. An induction of structural anisotropy in the polymer matrix may be beneficial for fundamental structure-property related studies and various applications. It was shown that only certain grafting parameters and annealing protocols were able to yield the anisotropic particle assemblies in the polymer melts. Compared to self-assembly techniques which are most commonly employed for PNCs preparation, magnetic directed self-assembly can produce various anisotropic structures with a conveniently controlled and homogenous orientation. Therefore, it is not surprise that this technique found its place among the processing protocols for PNCs.

Generally, the addition of polymer component into NP colloid system can attack the fragile interplay of forces between the NP-solvent-stabilizing agent. PNCs containing more traditional and non-magnetic NPs such as silica, calcium carbonate, hydroxyl apatite, carbon black, graphene and/or carbon nanotubes often exhibit problematic dispersion of hard inclusions. The dispersion of magnetic nanoparticle in different polymer liquids seems to be slightly more complicated when compared to the non-magnetic colloids. Arising the additional long-range magnetic interactions between the dispersed MNPs may worsen the dispersion quality considerably. Grafting and/or surface stabilisation of particles is often used in PNCs containing MNPs either structured or self-assembled to enhance the system stability. Despite various attempts for MNPs dispersion, an aggregation of MNPs in polymer liquids is often observed. Taking thermodynamically stable phase diagram for ordering of dipolar spheres in external fields proposed by Hynninen and Dijkstra (Figure 6B) into account, it is obvious that superlatticed structures are strictly conditioned by the homogeneity of dipolar building blocks and good dispersion stability. Achieving of higher volume fraction might be accompanied by the substantial worsening of NPs dispersion and thus, it is not surprise that randomly packed strings are most frequently obtained in polymer matrices.

For the fabrication of magnetically assembled PNCs, various laboratory scale processing techniques have been used by researchers. Fixing of the structures in PNCs sample with a final shape is an important requirement put on the chosen processing technology. Methods such as solution casting of thin films (*137-141*), bulk *in-situ* thermal (*142-152*) or photo (*118, 153, 154*) polymerization during magnetic irradiation of the samples are most frequently used. The most successful and promising processing methods for the fabrication of magnetically assembled PNCs will be mentioned in this chapter in more detail as an important source of the results.

1.4.1 One-dimensional magnetic structures in bulk polymer matrix

Solvent casting protocol are used for preparation of thin PNCs samples in the form of films suitable for quantitative evaporation of solvent from the bulk material. Fragouli, et al. (*138*) magnetically structured poly(ethylmethacrylate-co-methacrylate) (PEMMA) PNC from the chloroform solution in the presence of the magnetic field B=160 mT generated by two permanent magnets. Loading of γ-Fe_2O_3 MNPs in final PNC was kept as low as 1.0 wt. % (approximately ~0.25 vol. %), higher weight fraction can be found in their Supporting information. MNPs were surface treated by oleylamine and hexadecane 1,2-diol however leading to problematic aggregation in the case of self-assembled structure over the prolonged evaporation time due to quite immiscible nature of surface molecules with PEMMA matrix (Figure 10A). Magnetic micro chains were formed under magnetic field exhibiting the length ranging from ~0.7 to 15 μm and 80 nm diameter (Figure 10B) dependent on the time of the magnetic assembling. More coarse structures were obtained as particle loading increased (up to 5.0 wt. %~1.0 vol. %). Extensive coarsening of the magnetic structures in bulk PNCs were observed by various authors as result caused by compromised dispersion stability of the magnetic particles in liquid medium (*144, 146-153*).

Yuan, et al. developed flow casting protocol of Co/PS toluene colloid suspensions into thin PNCs films (*141*). Cobalt nanoparticles of two different morphologies were used: spherical (d=27 nm) and cylindrical (101x31 nm). MNPs were grafted with 2 nm layer of PS to enhance the dispersion stability. PNCs nanofilms loaded with 1-10 wt. % of MNPs (approximately ~0.15-1.5 vol. %) were assembled and vitrified in magnetic field (B=0.3 T) generated by the pair of permanent magnets. Anisotropic structures exhibit length of ~20 μm while the self-assembled MNPs remain homogeneously distributed in polymer film (see Figure 10C-F). Two populations of chains were observed: single NP thick assemblies and much wider – laterally merged assemblies (with a thickness ~ 1 μm) at certain locations of sample. Magnetic chains show stability of the alignment even at increased temperature ~60 °C above T_g of PS matrix for 24 hours.

Robbes. et al (*139*) studied the directed the self-assembly of PS grafted γ-Fe_2O_3 NPs with a various particle diameter (d=7.4, 10.2, 13 nm) in solution of PS under applied magnetic fields (B=10 and 60 mT). PNCs were vitrified bellow boiling point of dimethylacetamide solvent for 8 days. Isolated chain-like particle assemblies consisted from several particles were observed in very low particle loadings (0.05 vol. %). Percolated fractal-like particle aggregates with a structural anisotropy elongated along the field direction and interconnected by shorter lateral branches were formed at higher particle loadings (1-3 vol. %). Authors clearly demonstrated the effect of increasing particle diameter, volume fraction and magnetic field on the extent of response of MNPs to the external magnetic field and possibility to tune the morphology of magnetic PNCs by adjusting of these parameters (Figure 10G,H). As expected, large structures with well-developed anisotropy and macroscopic percolation were observed for the highest volume fraction and for the highest magnetic fields (Figure 10H).

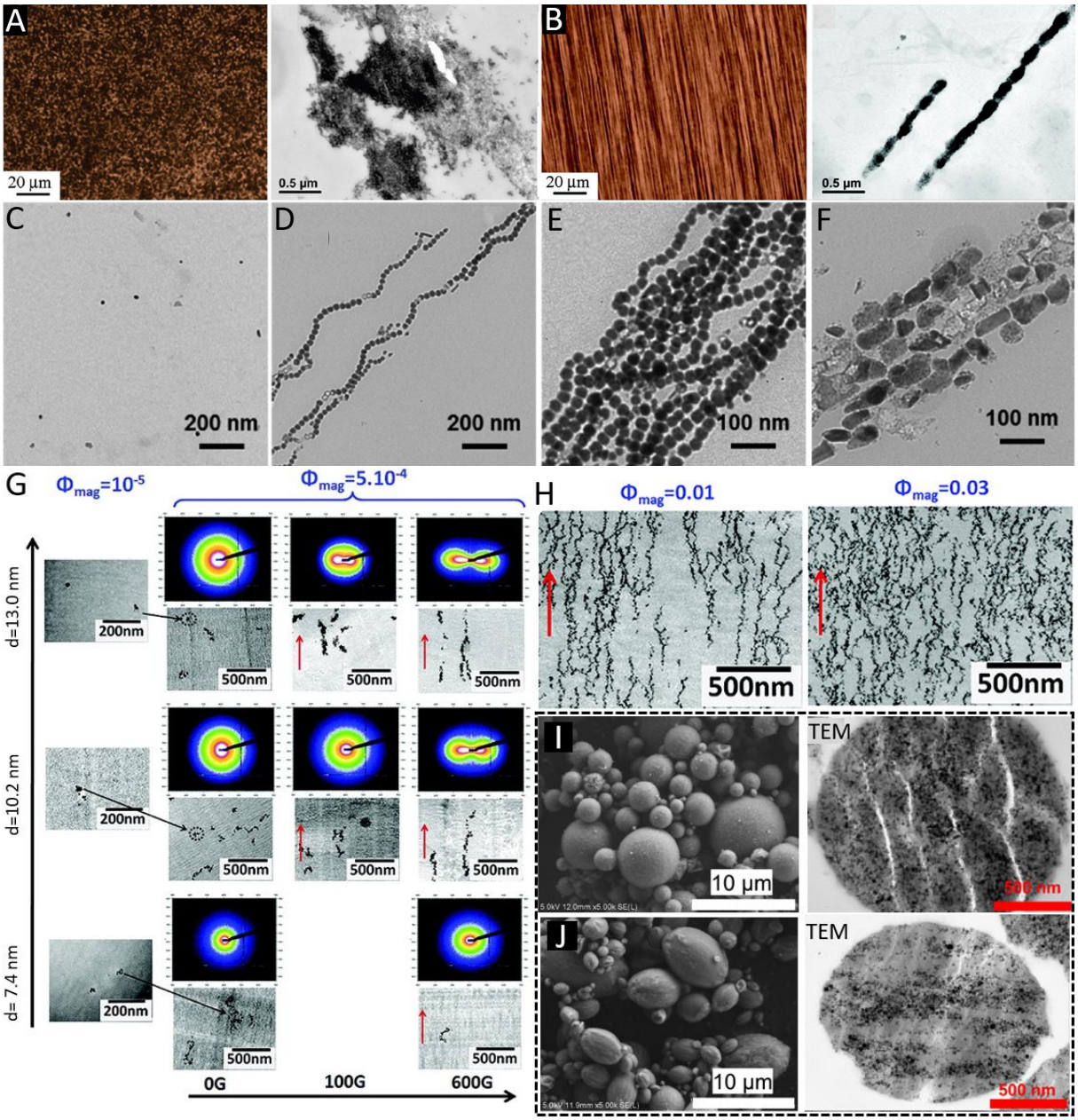

Figure 10 Optical and TEM images of (A) self-assembled and (B) magnetically assembled structure of γ-Fe_2O_3/PEMMA polymer nanocomposite. Reprinted with permission from ref. (*138*). Copyright 2011 American Chemical Society. TEM micrographs of (C) self-assembled and magnetically assembled (D) NP thick and (E) laterally merged chains from spherical Co and (F) laterally merged chains from cylindrical Co in PS matrix (loading 10 wt. %). Reprinted with permission from ref. (*141*). Copyright 2017 American Chemical Society. (G) TEM micrographs and 2-D SAXS patterns of magnetically assembled structures in PS matrix at various volume fractions (ϕ_{Mag}), particle diameters (d) and magnetic field strengths. (H) Structures with higher particle loading ϕ_{Mag}=0.01 and 0.03 assembled under 600 Gauss. Reprinted with permission from ref. (*139*). Copyright 2011 American Chemical Society. SEM and TEM micrographs of microspheres with encapsulated $CoFe_2O_4$ nanoparticles in the (I) field free state and (J) under external magnetic field. Reprinted with permission from ref. (*130*). Copyright 2014 American Chemical Society.

Magnetically structured PNCs fabricated from the liquid solutions by the aforementioned protocols need to be used in the form as prepared because they cannot be further thermally reprocessed such as for example solution blended and self-assembled PNCs. This disadvantage is slightly obviated by encapsulation of anisotropic magnetic structures in polymer micro spheres which may be used further as filler. In this case, magnetically assembled structures are permanently fixed in the thermally stable and cross-linked polymer spheres.

Ge, et al (*118*) prepared siloxane coated Fe_3O_4 spherical aggregates (CNCs) of various size encapsulated in polyethylene glycol dimethacrylate (PEGDMA) micro-emulsion dispersed in mineral or silicone oil. The surface stabilisation of spherical superparamagnetic Fe_3O_4 aggregates via siloxane coating prior the mixing with PEGDMA plays crucial role for successful dispersion of magnetic CNCs. Diameter of the resulted PEGDMA microspheres (4-150 μm) was controlled by the adjusting the viscosity of the environment and speed of mixing. One-dimensional magnetic chains were formed in the liquid micro PEGDMA phase during magnetic irradiation, then dispersed droplets were photo cured by irradiation of the emulsion by UV light.

Encapsulation of the one-dimensional magnetic structures was also studied by Abramson, et al. (*130*). $CoFe_2O_4$ (d=13.2 nm) nanoparticles were dispersed in siloxane prepolymer. Emulsification and polymerization led to formation of solid microspheres containing inner magnetic structure composed from the assembled magnetic nanoparticles (Figure 10I,J). Siloxane microspheres maintain an isotropic spherical shape in absence of the magnetic field, while rather elongated ellipsoids are synthesized due to growth of the particle structures within them when the magnetic field is applied. Polymer microspheres further assemble into microscopic chains via their remanent magnetization or additionally guided by the external magnetic field.

1.4.2 Assembling of non-magnetic particles

Particles and objects which do not show sufficiently strong magnetic response are hardly to be assembled in magnetic field of common intensities, therefore superconducting electromagnets with fields B>>1 T are required (well know experiment with levitating frog). For example, the magnetic properties of graphene exhibit weak diamagnetic behaviour (*155*). Hence, orientation and assembling of pristine graphene with the magnetic field is quite difficult to be achieved. Extremely large magnetic fields up to B=9 T were theoretically predicted to allow the alignment of the graphene sheets (*156*). Wu et al. (*157*) utilized the magnetic field with an intensity of B=10 T generated by superconducting magnet to assemble the graphene in aqueous dispersion of acrylic monomers. Magnetic fields of similar intensities were also used for the alignment of carbon nanotubes (*158*). It needs to be said that such electromagnets are not accessible in common laboratories. Despite graphene's low diamagnetic response, Lin et al. (*155*) were able to magnetically manipulate with graphene flakes by the magnetic field with a maximum intensity of B=240 mT. This was quite surprising result, and authors contributed their results to

one order of magnitude higher diamagnetic response of prepared graphene when compared to commonly reported values.

The surface decoration of nano- and microparticles such as graphene (*159-163*), CNTs (*164-166*), Al_2O_3 platelets (*167-170*), BN platelets (*171*) or Ag nanorods (*172*) with magnetic nanoparticles is frequently used to enhance their response to external magnetic field. This allows to use the magnetic fields of common strength. Le Ferrand, et al. (*162*) assembled Fe_3O_4 decorated graphene into mesh-like graphene structures and Billaud, et al. (*163*) used this approach for anisotropic deposition of the material and for enhancement of lithium storage capacity of graphite/Fe_3O_4 electrode. Erb and Studart pioneered the electrostatic deposition of the magnetic nanoparticles on the surface of Al_2O_3 micro platelets to achieve their response to magnetic stimulus (*167, 168*). The orientation of the micro platelets was controlled by the direction of the magnetic field. Also, magnetic material can be conveniently deposited into specific areas and locally increase the inorganic content by the field gradient (Figure 11A-C). This concept of orientation and/or deposition of inorganic platelets was used in the combination with various matrices such as polymers (*167, 168, 173-175*), inorganic cements (*176*), ceramics or metals (*177*). Composites exhibit improved mechanical properties according to classic micromechanics theories for composite materials. Next, Martin, et al. (*174*) and/or Kokkinis, et al. (*175*) combined this magnetically responsive material dispersed in photocurable resin with an additive manufacturing technology and 3D printed objects with complex geometries and biomimetic microstructure.

1.4.3 Patterning by the heterogeneous magnetic field

As outlined in the section above, using of the magnetic field as a contactless manipulator for increasing of the local concentration of the inorganic phase seems to be very interesting and successful method for micro structuring of the organic matter. Formation of superstructures along the lines of magnetic field and/or magnetophoretic drifting of the magnetic material along the magnetic field gradient can be used for the programmed localization/deposition of inorganic phase. Magnetic micro spicules were synthesized in the polydimethylsiloxane (PDMS) matrix by the attraction of magnetite NPs with a permanent magnet (field gradients: 0.12-0.27 $T \cdot cm^{-1}$). The height of magnetic spicules decreases with a field gradient (*178*). As well, Ghosh, et al. (*179*) later used gradient of permanent magnet to create highly concentrated magnetic micro domains in PDMS matrix. Gizynski, et al. (*180*) used 80 μm iron particles dispersed in PDMS matrix poured in rotating cylindrical tubes immersed in complex shapes of magnetic field – as for example, it is schematically depicted in Figure 11 E. In addition, parallel micro plates, single, double, triple or quaternary micro spirals were formed in complex fields. The shape of the magnetic structures is preserved by thermal polymerization of siloxane prepolymer. Contactless magnetic manipulation by aid of the field gradient led to development of the '*magnetic drawing*' in a liquid polymers or their monomers using an immiscible ferromagnetic droplet which leaves a trail of magnetic leftovers torn from the droplet during its migration in the liquid matrix controlled by external magnet (*181, 182*) (Figure 11 D).

1.4.4 Polymer bound structures – structures with high inorganic content

The achievement of high filler fraction in polymer matrix is desired (*183*) but commonly problematic for PNCs technologies. As a particle concentration in melt or liquid polymer matrix increases, the dispersion quality is usually worse and massive aggregation of NPs occurs. To obviate this problem, techniques for the stabilization and magnetic field patterning of MNPs into anisotropic structures from the colloid dispersion seems to be promising pathway for the future bottom-up construction of advanced materials. Important and reasonable step seems to be the exchange of commonly used stabilising agents such as fatty acids and/or low molecular organic substances with high molecular weight polymer chains or cross-linking/polymerizable monomers.

Motornov, et. al (*184*) assembled 30 nm γ-Fe_2O_3 NPs with a surface stabilization by pH sensitive polymer shell composed from PV2P-b-PEO. Magnetic interactions brought particles to very close contact but still distanced by the polymer chains which also interlocked particles. Long magnetic chains with a width ~25 μm are stable in pH range 5.5-3.5 to a such extent that structures can be rotated in magnetic field without disintegration.

Zahedi, et al. (*185*) assembled 9 nm $MnFe_2O_4$ magnetic nanoparticle dispersed in diluted toluene suspensions in presence of thermal initiation and methyl methacrytale monomer. At temperature 80 °C and in magnetic field 80 mT, straight micro wires with a nanometer diameter permanently bound by PMMA chains were created.

He, et al. (*85*) used spherical magnetic aggregates of Fe_3O_4 (termed as CNCs) with deposited siloxane layer as stabilizing layer to avoid the contact aggregation. After certain time, magnetic field was switched on to assemble the CNCs into straight particle chains. Later, two-dimensional labyrinth-like structures standing on the micro magnetic template (Figure 11F-H) were assembled from the ethanol solution by Zhang, et al. (*86*). Condensation of siloxane monomer during the assembling was utilized for the interconnection and preserving of the structures in the field off state. Magnetic structures hence cannot fall apart because they are glued by the polymer chains. Mechanism for creation of such unique structures is proposed as follow: *i*) assembling of silica coated spherical CNCs into one-dimensional particle chains standing perpendicular on the magnetic template, *ii*) shifting of particle chains due to instability of magnetic interactions and iii) merging of particle chains into two-dimensional sheets by their lateral attraction. Surface coverage of micro magnetic template by the perpendicularly standing structures can be controlled by changing of the concentration of CNCs in ethanol solution.

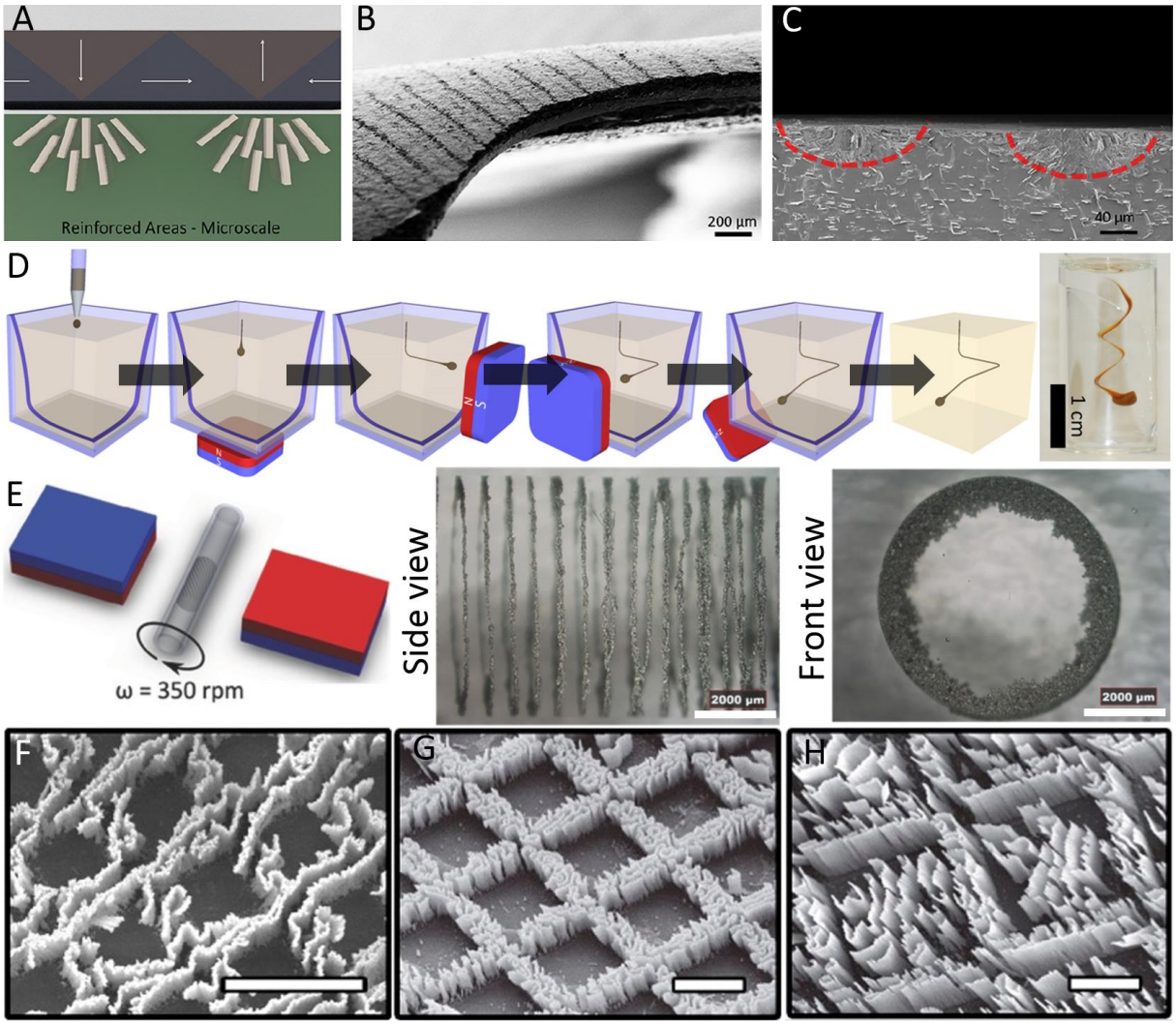

Figure 11 (A) Schematic illustrations, (B) top view and (C) cross-section of locally concentrated regions of magnetized alumina platelets in polyurethane matrix by the aid of magnetic field gradient. Regions containing high amount of inorganic phase are outlined by red line in (C). Reprinted with permission from ref. (*169*). Copyright 2012 American Chemical Society. (D) Schematic depiction of contactless magnetic manipulation with a magnetic droplet leaving trail of material in liquid PDMS matrix by positioning of permanent magnet and the snapshot of final cured object. Reproduced with permission from ref. (*182*). Copyright 2016 American Chemical Society. (E) Experimental setup – alignment of magnets and vessel containing iron microparticles in liquid PDMS and digital snapshot of resulted iron structures in cured polymer (side and front view). Reprinted with permission from ref. (*180*). Copyright 2017 John Willey and Sons. (F-H) Two-dimensional labyrinth-like structures perpendicularly standing on the micro magnetic template assembled from ethanol solution of SiO_2 coated magnetite aggregates. Scale bar is 20 µm. Reprinted with permission from ref. (*86*). Copyright 2013 American Chemical Society.

1.5 Physical properties of polymer nanocomposites

Classic polymer microcomposites (PMCs) find every-day utilization in various technological applications. PMCs were meant to decrease the price of the polymer parts by replacing of the polymer phase with much cheaper inorganic particles. However, it was found that incorporation of inorganic particles can beneficially affect the mechanical, thermal, electric, optic or magnetic properties in addition to price reduction after all. In recent years, polymer nanocomposites (PNCs) attracted a great interest of researchers and engineers due to wide range of properties and functions that can be modified by the addition of relatively small amount of NPs when compared to their microparticle (MP) counterparts. This is related to unique nanoscopic interactions and physical mechanisms offered by the nanoparticles. Special interest is paid to increasing of particle's surface required for these interactions when particle diameter decreased down to nanoscale (d<100 nm). However, processing complications and price of PNCs is more unfavorable compared to PMCs. Electric and magnetic properties of PNCs will be briefly introduced while special interest will be paid to review classic theories for mechanical properties of PNCs in following chapters.

1.5.1 Electric and magnetic properties

It is obvious that both electric and magnetic properties of PNCs depend on the addition of components with desired magnetic or electric properties. Also, alignment of magnetic moments and/or structural anisotropy, percolation and creation of electrically conductive pathways plays an important role for macroscopic response of material (*109, 164*). Magnetic particle chains exhibit higher magnetization in longitudinal direction while transverse direction shows slightly smaller magnetic response. These results can be found in exhaustive number of references studying the particle structures assembled from solution (*73, 74, 80, 123, 127*) or embedded in polymer matrix (*130, 138, 148, 153, 164, 186*). Unfortunately, magnetic anisotropy is frequently left without proper elucidation of its physical origin and magnetic properties became sort of cliché. Simple explanation of this phenomenon is on the other hand provided by Lisiecki and Pileni (*187*) and depicted in Figure 12A. During the assembling of MNPs in the magnetic field, their magnetic moments are aligned in the field direction. Therefore, magnetic moments are largely oriented in the direction of structure's long axis. Higher extent of parallelly orientated magnetic moments then results in higher magnetic response during magnetometric measurements.

Especially collective interactions of magnetic moments acting on the nanoscale lengths seems to be experimentally complicated to be measured. Usually, only macroscopic response is measured by the magnetometer (sort of vector summation of moments). To substitute this, emerging methods such as electron holography can be utilised to visualise the nanoscaled magnetic fields around MNPs and within their assemblies (*72, 188-194*). On the other hand, it needs to be mentioned that this technique is quite rare due to its requirements on equipment and experimental experience. Collective interactions and orientation of magnetic moments in anisotropic structures of Co nanoparticles can be seen in field free state (moments are stabilised

by each other) and under strong magnetic fields (±2 T) as reconstructed by the electron holography (Figure 12C) (*188*).

Response of polymer composites to external magnetic field was utilised in the various smart field responsive polymer parts. For example, Mishra, et al. (*149*) created two-dimensional thermoplastic polyurethane composite sheets with aligned microstructure. Cross shaped samples were cut from the sheets and origami-like folding of arms was observed according to an orientation of structures and intensity of external magnetic field. Also, Marchi, et al. (*150*) prepared magneto-responsive soft PDMS microstructured matter controllably deformed under relatively weak magnetic fields (*B*=42-100 mT). Such magneto-responsive materials can be used as shock absorbers, sensors, artificial muscles and actuators in various devices and soft robotics (*195*).

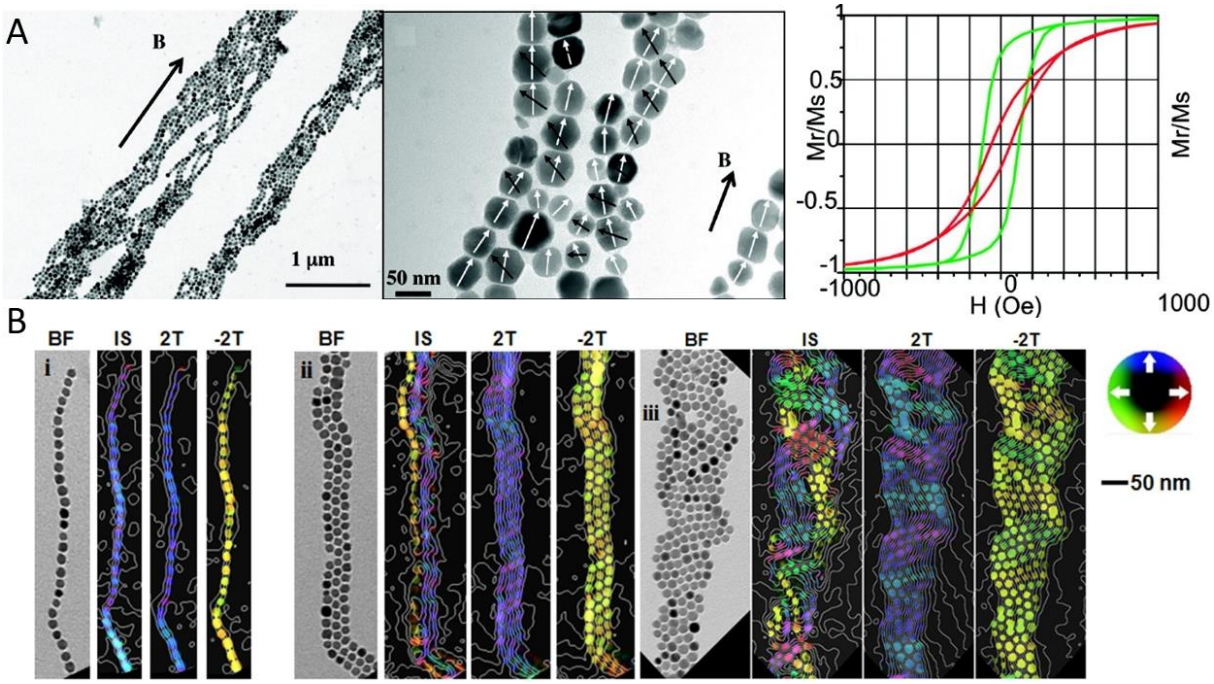

Figure 12 (A) TEM micrographs with corresponding magnetization curves measured parallel (green) and perpendicular (red) to the direction of magnetosomes extracted from AMB-1 magnetotactic bacteria. White arrows indicate [111] crystallographic direction – easy magnetization axis. Reprinted with permission from ref. (*187*). Copyright 2012 American Chemical Society. (B) Bright-field TEM images and electron holography reconstruction of generated magnetic field in (i) one, (ii) three and (iii) multiple Co particle thick structures in zero (IS) and ± 2 T magnetic field. Color wheel represents magnitude and direction of generated magnetic field (moment). Reprinted under open license from ref. (*188*). Copyright 2012 Nature.

1.5.2 Thermo-mechanical properties

Addition of NPs into polymer matrix results in non-trivial enhancement of macroscopic thermo-mechanical response. Classic composite micromechanics theories which are quite viable to explain the mechanical response of PMCs fail in the case of PNCs. For PMCs, simple volume replacement for isotropic and/or stress-transfer for anisotropic particles are valid mechanisms

explaining increase of PMC's mechanical robustness. However, none of these mechanisms cannot satisfactorily and fully explain mechanical and thermo-mechanical response of PNCs. For example, critical length for graphene or its derivates lies in the range of 5-20 μm for the stress to be fully transferred from the matrix into the graphene sheet (*196-201*). Hence, stress-transfer into submicron objects might be quite doubtful regardless of mismatch between matrix's and inclusion's stiffness. The explanation of the mechanical response via simple stress-transfer into the anisotropic NPs is doubtful even for common graphene filled PNCs exhibiting crumpled, wrinkled graphene sheets with a sub-micro length and different extend of exfoliation, structural defects and orientation. In such cases, graphene particle can be rather simplified by the isotropic particle with a compromised stiffness when subjected to deformation. Volume replacement on the other hand can be partially used for granular (filled) systems since this mechanism is based on the replacement of soft polymer volume by a much stiffer inorganic phase with a higher modulus. Assuming iso-strain conditions in all phases of composite during the deformation ($\varepsilon_M = \varepsilon_F$), additional portion of mechanical energy is required to deform stiff inclusion when compared to unfilled polymer. However, both mechanisms (stress transfer and volume replacement) seem to be valid only for the glassy matrix and reasonable mismatch of component's moduli. At elevated temperatures, situation is far more complicated

There is a large gap in the knowledge leading to the connection of nanoscopic mechanisms between NP-polymer and macroscopic mechanical response of the material (*202, 203*). Discrepancies between common continuum micro-mechanics theories and nanoscale mechanisms of PNCs are supported by different magnitude of moduli enhancement bellow and above glass transition of polymer (*204-208*). When loading of NPs in polymer matrix remains low, commonly very modest enhancement of PNC's modulus is observed bellow T_g which is consistent with micro-mechanics models. However, vast enhancement of PNC's modulus is observed around and above the glass transition. Question *why?* still remains more or less unanswered and possible mechanisms vary from system to system and from author to author. In the field of PNCs, two reinforcing mechanisms are respected among the researchers: *i*) altered relaxations of polymer by its immobilization in the presence of inclusion and *ii*) sort of stress-transfer via interconnected particle superstructures (*209, 210*). Interested reader can find more detailed information about these concepts and current issues and trends in PNCs reviewed by Jancar, et al. (*203, 211*) and/or Song and Zheng (*212*).

1.5.2.1 Polymer immobilization

Jancar, et al. (*206-208, 213-216*) comprehensively studied effect of the immobilised glassy layer induced on the surface of particles on various mechanical properties of PNCs. The fundamental difference between PMCs and PNCs is depicted via relative size of polymer coils with R_g=5 nm in presence of spherical MPs with a diameter 1 μm and NPs with a diameter 10 nm (Figure 13A). Loading of particles is kept at 7 vol. % in both cases at which average interparticle distance of idealized FCC packed spheres equals to the particle diameter (Figure 13B). In both systems, interfacial interactions between polymer segments and particle surface

are expected according to their chemical nature (repulsion versus attraction). In the case of attractive interaction, immobilized ‘‘glassy’’ layer is expected to be created with retarded chain dynamics compared to unaffected polymer in the bulk (Figure 13C). The thickness of interface layer is usually several nanometers and it was studied by various authors and methods (*11-13, 217-220*). However, in the case of PMCs as depicted in Figure 13A, only very small portion of polymer is affected and majority of the polymer chains remain in the bulky unaffected state without a knowledge about the particle presence when compared to their PNCs counterparts. In PNCs at same filler loading (7 vol. %), interparticle distance is on the order of polymer coil radius and all polymer chains interact at least with one particle surface. For randomly packed spheres in the PNCs, average interparticle distance of one particle diameter is achieved at volume fraction 2.6 % (Figure 13B-black line).

It needs to be point out that immobilization affects only polymer chains or their segments with a released mobility – undergoing conformation reconfigurations with a measurable relaxation time (detected within time scale of experiment). Bellow glass transition, all chains are in ‘‘frozen’’ glassy state with incredible long relaxation times and thus there is no observable influence of the NPs on the mechanical response.

Recman and Jancar (*206*) studied the effect of particle size (micro versus nano) on the mechanical response of PMMA in both relaxation regions – bellow and above the glass transition of prepared composites. They observed discrepancies between experimentally measured moduli and theoretical models: Kernern-Nielsen-Lewis model for volume replacement bellow T_g (Figure 14B) and Guth-Gold model above T_g associated with an entropic contribution from the strain-amplification of the matrix (Figure 14A). These differences between models and experimental values are based on fact that most of the theoretical predictions use values of unmodified (pristine) matrix modulus. However, it cannot be valid anymore with a respect to above outlined immobilization concept and matrix modulus in vicinity of solid inclusion is altered. They proposed that modulus of modified–immobilised matrix (E_M^*) scales with a filler’s surface area (S_F) available for physicochemical interactions – which is a function of the filler volume fraction (ϕ) and level of NPs dispersion; and the extent of interfacial interaction strength (K) which depends on chemistry of system.

Kalfus and Jancar (*213, 215, 216*) already previously showed that surface area of nano filler is rather being used as a scaling parameter for the thermo-mechanical properties rather than filler volume fraction regardless of particle shape, size and/or aspect ratio while keeping constant chemistry (K). Dorigato, et al. systematically studied the influence of various processing parameters (filler size and surface treatment) on the structure of various PNCs and effect of the structure on different mechanical properties of amorphous PLA (*221*), PU (*222*), epoxy (*223*) or semicrystaline PE (*224-229*) and PP (*230*) nanocomposites. Mostly, fumed silica or nano clay was used as fillers and despite crystallization effects of NPs on PE or PP, conclusions similar to Jancar were made – mechanical properties depends on the ability to form the immobilised layer which is a function of available particle’s surface (*221, 224, 226, 230*).

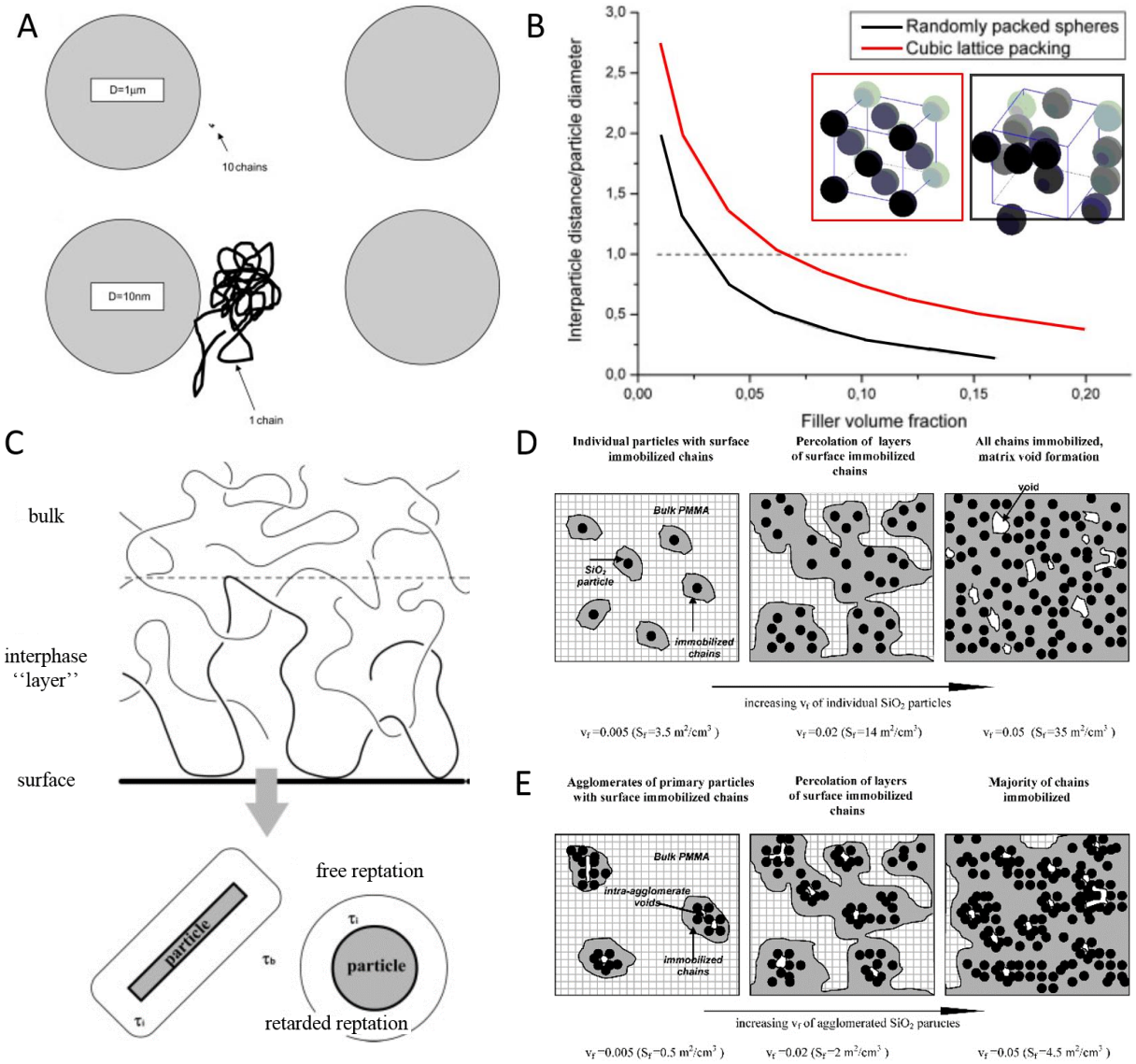

Figure 13 (A) Simplified depiction of relative size of single polymer chain with R_g=5 nm in vicinity of microparticle with a diameter 1 μm and 10 nm for nanoparticle. (B) Average interparticle distance as a function of filler volume fraction normalized to particle dimeter for randomly and FCC packed hard spheres. Reprinted from ref. (*203*), Copyright 2010, with permission from Elsevier. (C) Schematic representation of bound immobilized polymer layer around particle. Reprinted with permission from ref. (*213*). Copyright 2007 John Wiley and Sons. (D,E) Schematic representation of percolation of immobilized layers as filler content increases. Reprinted with permission from ref. (*207*). Copyright 2013 American Chemical Society.

Effect of NPs on the mechanical properties bellow T_g is commonly negligible and high particle contents are required to induce any significant enhancement of mechanical response which usually obey micro-mechanical mechanisms ($E=f(\phi)$), see Figure 14C,D. Surprising effect was showed by Hashemi, et al. (*231*) who studied the mechanical response of PMMA/SiO_2 nanocomposites in glassy state. Special surface treated silica nanoparticles with organic molecules providing strong hydrogen bonding with PMMA chains were used. Young's

modulus and yield stress was enhanced by 114 % and 94 %, respectively in the glassy state which is surprising result. Here the strong hydrogen bonding between moieties on the silica surface and PMMA chains led to massive physicochemical cross-linking of the matrix. NPs with a strong binding/attraction thus rather act as cross-liking agents increasing polymer network density and/or chain length.

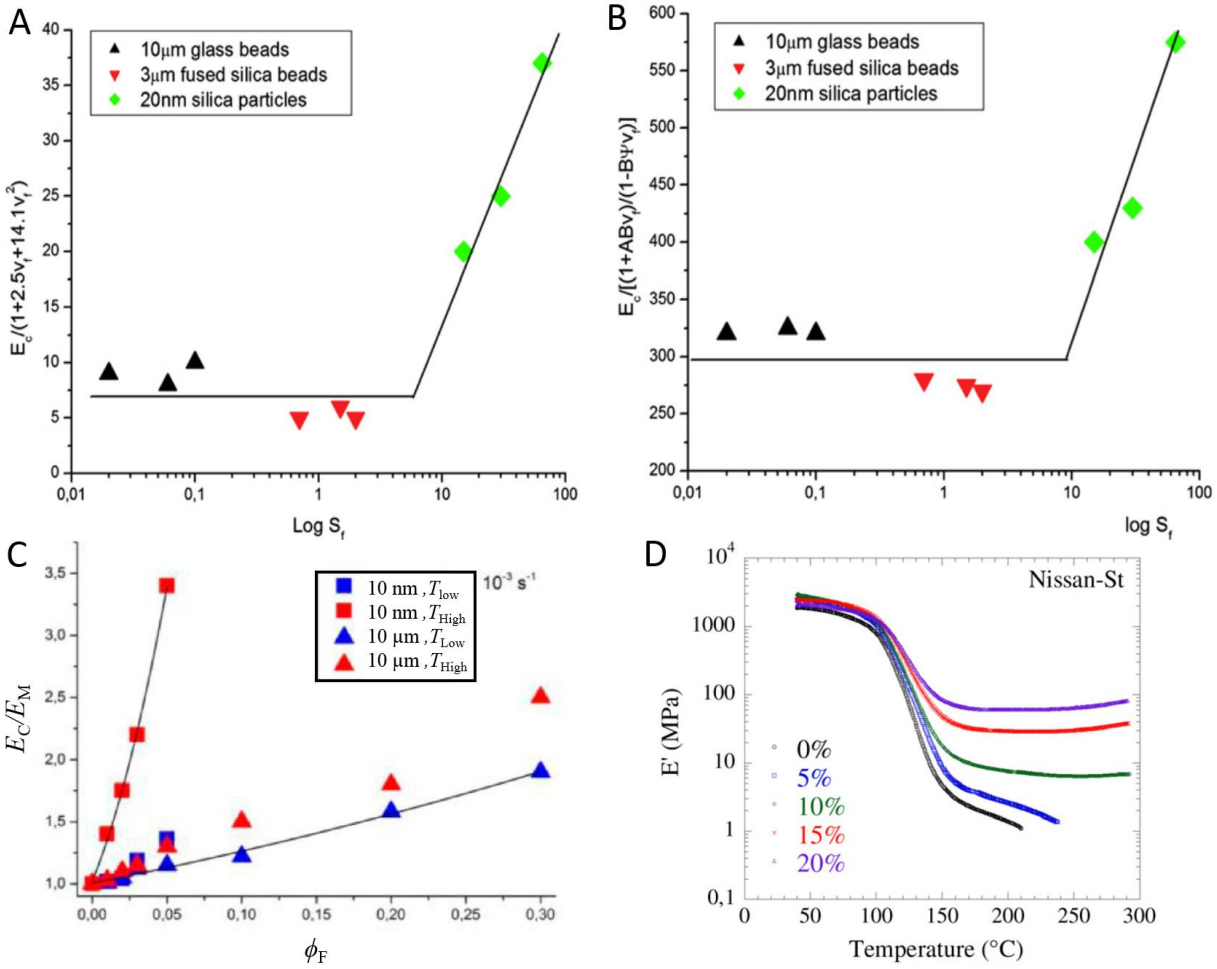

Figure 14 Modification of matrix modulus as function of specific surface area of micro and nanoparticles (A) above T_g and (b) bellow T_g. Reprinted from ref. (*206*), Copyright (2010), with permission from Elsevier. (C) Relative composite modulus as a function of filler volume fraction at T_{Low}=T_g-80 °C and T_{High}=T_g+15 °C. Reprinted with permission from ref. (*207*). (D) DMA temperature ramp of PS/SiO_2 PNCs with an increasing volume fraction of SiO_2 indicated by the legend in the graph. Reprinted from ref. (*205*), Copyright (2012), with permission from Elsevier.

Jouault, et al. studied effect of the nanosilica particles on the mechanical response of PS and PMMA (*204, 205*) in the order to elucidate the origins of the mechanical response. Two main reinforcing mechanisms were taken in an account by authors: *i*) filer-polymer matrix effect and *ii*) filler network contribution. Vast enhancement of storage modulus above the glass transition is again observed while enhancement bellow this temperature is consistent with a volume replacement and negligible compared to situation at high temperatures (Figure 14D).

Percolation threshold in their systems was observed around ~7 vol. % above which dramatic upturn of storage modulus in rubbery plateau occurs. Bellow this threshold, reinforcing mechanisms were solely ascribed to the immobilization of polymer matrix by the presence of NPs organized in the small aggregates (Figure 15C) as filler volume fraction is increasing and consequently primary particle aggregates percolate into three-dimensional particle network (Figure 15D) which is claimed to be responsible for the dramatic stiffening of rubbery-like matrix.

The contribution of filler percolation to enhancement of the visco-elastic properties is rather based on the percolation of the immobilized polymer layers which bridge the interaction between adjacent particles or their aggregates perturbing from sub-nano to macro length scales. Nevertheless, it needs to be mentioned that these two mechanisms occur simultaneously as well they influence each other. As for example polymer bound layers can stabilize the existence of densely packed particle aggregates or clusters and contribute to stress transferring into structure and aggregation/clustering of particles will bring the immobilized polymer layers close to percolate. The percolation of glassy polymer shells is depicted in Figure 13D,E. The bridging of particles via confined polymer segments is believed to be responsible for the vast enhancement above *Tg* (*207, 212, 232-236*).

1.5.2.2 Effect of particle structures

Nanoparticles are usually arranged in various nano-, sub-micro-, micro and macro structures inside the polymer matrix (Figure 15C,D). The bottom-up assembling of NPs and increased NPs concentration lead to creation of percolated and hyper branched structures which are termed as *fractal aggregates* (*237-241*). The example of such self-assembled structure and its bottom-up formation from the primary NPs can be seen in Figure 15A and B, respectively. The contribution of NP-NP interactions to the internal stiffness of the assemblies is far less clear than polymer immobilization concepts.

First ideas about possible reinforcing mechanism of particle structures came up with a ‘‘occluded’’ matrix inside the aggregates which is not able to contribute to deformation process and thus the stress is concentrated outside the aggregates resulting in increase of the stiffness. However, this picture does not explain the deformation of composites at higher strains because composites are often able to sustain much higher stress than a simple tensile strength of matrix and this concept would rather support reduction of breaking strength (*242*). Witten, et al. (*242*) also proposed that reinforcing of rubber by the networking fractal aggregates is rather due to interparticle axial attraction and lateral deformation of aggregates, especially at higher strains.

It is presumably believed that different particle assemblies have non-zero stiffness and strength due to existing cohesive interparticle forces which stabilize the particle assemblies during the deformation (*204, 210*). Shaefer and Justice (*243*) outlined that stiffness of particle assembly gradually decreases from values corresponding to the bulk modulus of single particle to negligible values as particle structure is growing in diameter. The role of perturbing polymer is not discussed but taking the strength contribution from the interparticle forces to the overall

stiffness of the structure under consideration is also realistic assumption. There would not be any reason for particle to aggregate if these stabilising forces holding each particle assembly together would not be sufficiently high enough. Atomistic deformation of individual particles within the polymer matrix and stress-transfer via skeleton of nanoparticle structure were also studied as possible contributions to overall stiffness of PNCs (*244*, *245*). Deformability and compactness of particle aggregates seems to play an important role (*137*, *244*, *246*, *247*) and interlocking/friction between individual particles can be beneficial for increased stiffness of the particle structure (*244*, *245*, *248*).

Elastic properties of nanoparticle aggregates were studied in detail for example by the researchers around prof. Sheldon Friedlander in early 2000s (*249-255*). They provide large number of *in-situ* observation of aggregate deformation in tension by SEM/TEM and micromechanical measurements of their mechanical response by AFM. In their experiments, particle aggregates show various elastic features such as retraction after breaking due to release of the stored elastic energy or rotation of individual particles within chain during straining. The strength between two primary particles was measured in the order of 8 nN and maximum stiffness of aggregate was calculated as 3-8.8 MPa and/or even hundreds of MPa for laser ablated and condensed carbon aggregates. The stiffness of structures was ascribed solely to van der Waals attractions between the primary nanoparticles. But for high values, sort of sintering of carbon nanoparticles creating a neck between them might contribute to overall stiffness.

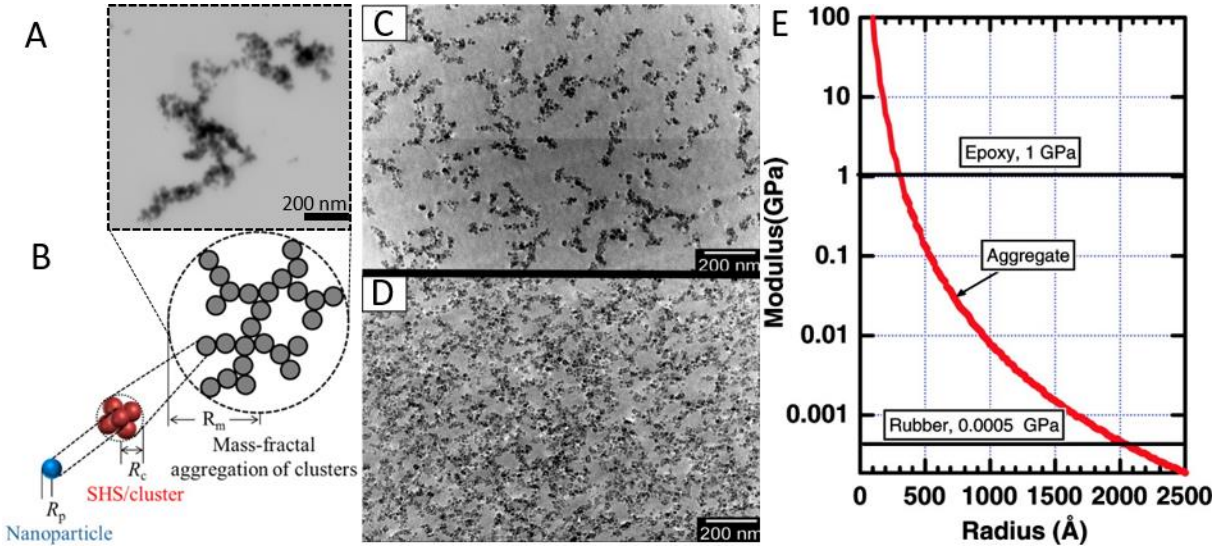

Figure 15 (A) Fractal aggregate studied in this thesis. (B) Schematic depiction of bottom-up aggregation process. Reprinted with permission from ref. (*240*). Copyright 2016 Americal Chemical Society. (C) Fractal aggregates of SiO_2 nanoparticles in PS matrix at filler loading ϕ=6.6 % and (D) percolated particle network at loading ϕ=15.7 %. Reprinted with permission from ref. (*204*). Copyright 2009 American Chemical Society. (D) Proposed decrease of modulus of particle structure from single particle to complex multi particle large structure. Reprinted with permission from ref. (*243*). Copyright 2007 American Chemical Society.

It is surprising that nature can create geometrically and structurally complex materials from the very simple nano building blocks such as stiff reinforcing phase bound together by soft organic macromolecules. The content of inorganic phase is usually very high but these structures exhibit mechanical robustness and toughness lacked by man-made top-down materials (*256-259*). This is due to specific arrangement of stiff and tough nano blocks in bottom-up manner into larger reinforcing units creating complex multi-level hierarchy of biological structures (*257, 259, 260*). Controlled bottom-up assembling of nano building blocks into micro-sized reinforcing units is driving inspiration of this work.

1.5.2.3 Mechanical properties of magnetically assembled anisotropic structures

The literature dealing with magnetically assembled structures is not very comprehensive as well it does not offer much of explanations. But according to few experimental observations, anisotropic particle structures formed in the magnetic field exhibit a non-zero intrinsic stiffness and ability to reinforce polymer matrix during the deformation.

Rigbi, Sohoni and Mark (*142, 143*) studied the effect of the magnetically assembled structures built from sub-micro elliptical Fe_2O_3 particles on the static mechanical properties of PDMS elastomer. Nevertheless, no structural information is provided, micro-sized one-dimensional chains are expected to be created. Authors observed a massive increase of stiffness and strength of the composite, both increasing with an applied field intensity (300, 525 and 1100 G) during matrix curing. In addition to this, they observed significant anisotropy of mechanical response when mechanical properties were measure longitudinally or transversely with a respect to the magnetic chain's axis (Figure 16A). This finding greatly supports a concept of solid-like behaviour of particle assemblies resulting in their non-zero stiffness during the deformation.

Bellan and Bossis (*144*) studied very similar system with a similar effect of anisotropic micro structures on the mechanical properties. In addition, measured mechanical properties in external magnetic field exhibited significant increase of the system stiffness suggesting much stronger interparticle interactions due to magnetic attraction and thus intrinsically stiffer structure. Similarly, Borin, et al. (*261*) showed that magnetization of elastomer filled with randomly dispersed microparticles of FeNdB (material used for permanent magnets) during the mechanical testing lead to impressive increase of composite tensile modulus. This enhancement was even pronounced for the composites with anisotropic structures (*262-265*) exposed to external magnetic fields which was contributed to magnetic energy within the structure. However, measuring of nanoscopic magnetic interaction between nanoparticles and nano objects might appear as more difficult task and electron holography (*72, 188-194*) or magnetic force microscopy (*266*) might come in hand.

The mechanical anisotropy of magnetically assembled nanoparticle system was also studied by Robbes, et al. (*139*) in uniaxial static tension above T_g of the PS nanocomposite. Authors produced elongated fractal aggregates of γ-Fe_2O_3 in PS matrix which were consequently percolated by lateral branches into particle network at loadings 1-3 vol. % in magnetic fields B=10-60 mT (see Figure 10G-H). Increased tensile modulus and strength ware observed for the

nanocomposites in the uniaxial tension (Figure 16B). Authors claimed that they provide first experimental evidence for the control over the structural anisotropy triggered by the external field stimulus that have beneficial effect on the mechanical response of polymer nanocomposite. However, similar systems were studied even previously including various matrix systems filled with micro (*144*), sub-micro (*143*) or even nano sized magnetic particles (*137, 264, 267*). Mechanical properties were usually investigated in close proximity or far above of T_g of the matrix but mechanisms of reinforcing effectivity of anisotropic structures rather left unanswered and usually very vague discussion of mechanical properties (if so) is offered by the authors. But few reinforcing mechanisms can be found as analogy with a reinforcement by the particle network. Lateral compression during uniaxial tension (and lateral stretching during uniaxial compression, respectively) was described as a mechanism that can contribute to stiffness of particle superstructures by promoting of direct particle-particle contacts or interparticle friction by Witten, et a. (*242*). Percolated particle network with branches in lateral direction thus could sustain significant lateral compression during uniaxial stretching of the network. However, this mechanism seems to be more pronounced especially at higher deformations. Jestin, et al. (*137*) studied the mechanical response of magnetically assembled γ-Fe_2O_3 nanoparticles in PBuA/PMMA matrix with an in-situ small angle neutron scattering (SANS) during the sample stretching and ascribed reinforcing at high strains to this mechanism.

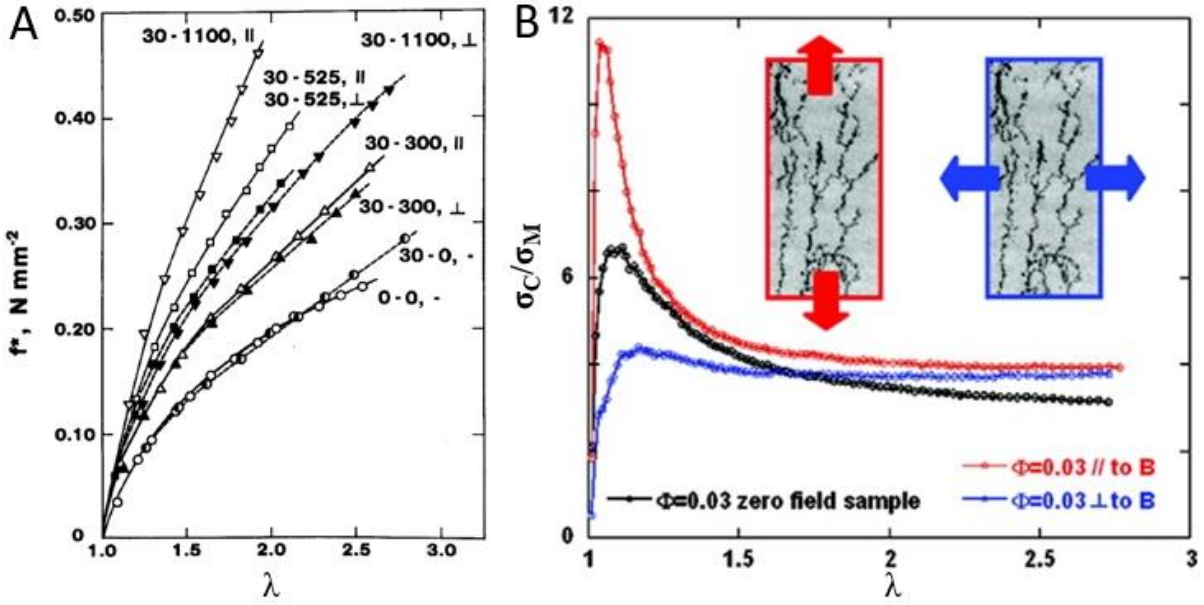

Figure 16 (A) Stress-strain curves for PDMS matrix (○) and its composites containing 30 wt. % of sub-micro magnetic particles assembled in the absence of magnetic field (◐) and increasing magnetic field (▲) 300, (■) 525 and (▼) 1100 Gauss. Empty and filled symbols are for longitudinal and transverse direction, respectively. Reprinted with permission from ref. (*143*). Copyright 1987 John John Willey and Sons and Sons. (B) Normalised reinforcing effectivity of magnetically assembled PS/γ-Fe_2O_3 nanocomposites to the neat PS matrix as function of draw ratio (λ) with depicted structures and measured directions. Reprinted with permission from ref. (*139*). Copyright 2011 American Chemical Society.

Aim of thesis

Impulse of external magnetic field initiates controlled assembling process of magnetic nanoparticles into ordered nano and microstrucutres. Magnetic dipole interactions are driving force of this process and dependent on the strength of external magnetic field, while environmental resistance of polymer matrix counteracts against these forces. Also, initial particle packing has a large impact on the balance of magnetic forces between particles and determines the size and structure of primary assembling blocks. The aim is to evaluate the influence of these processing parameters on the resulted structure with a respect to the kinetics of this process. Structural parameters will be used for interpretation of mechanical properties of these nanocomposites.

2 Materials and methods

2.1 Magnetic nanoparticles

The first set of experiments was conducted with a usage of a commercial grade of magnetite nanoparticles – Fe_3O_4 (d=103 nm) purchased from Sigma-Aldrich (Figure 17). However, proper and stable dispersion of these particles from the powder state was almost impossible despite using of various methods such as ultrasonication or even using of OA as a stabilizing agent and/or different solvents. After, couple of seconds gradual aggregation of MNPs occurred followed by their sedimentation. These failures led to synthesis of Fe_3O_4 magnetic nanoparticles.

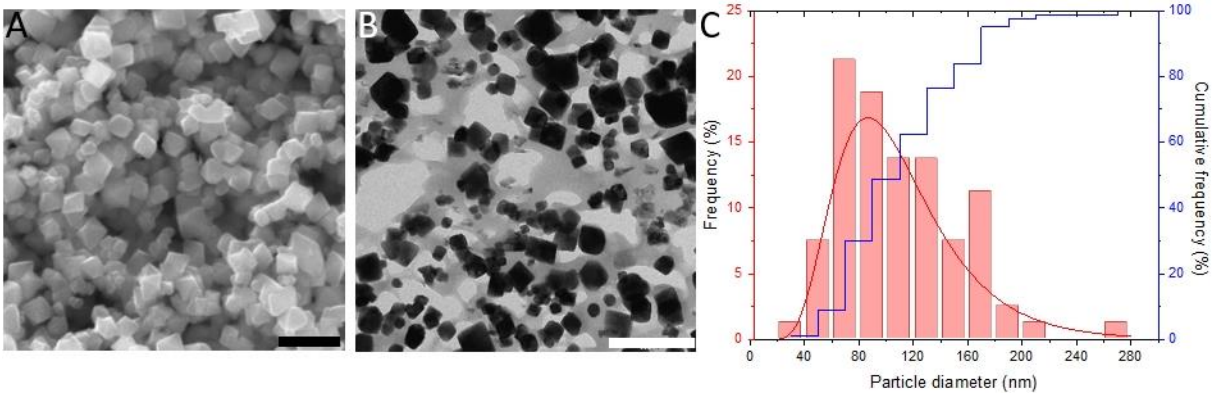

Figure 17 (A) SEM and (B) TEM electron micrographs of commercial Fe_3O_4 nanoparticles (Sigma-Aldrich) (scale bar is 500 nm in both) and (C) lognormal particle diameter distribution.

Synthesized Fe_3O_4 nanoparticles were prepared by the following procedure. Briefly, inorganic salts containing iron ions ($FeCl_3 \cdot 6\ H_2O$ and $FeSO_4 \cdot 7\ H_2O$) were dissolved in distilled water at the laboratory temperature and N_2 was bubbled trough the solution. Then, water solution of NH_4OH was very slowly introduced trough the small diameter tube during vigorous mechanical stirring of the reaction solution. Reaction scheme for the magnetite precipitation is as follows:

$$Fe^{2+} + SO_4^{2-} + 2\ NH_4^- + 2OH^- \rightarrow Fe(OH)_2 + (NH_4)_2SO_4$$

$$Fe^{3+} + 3\ Cl^- + 3\ NH_4^- + 3\ OH^- \rightarrow FeOOH + 3\ NH_4Cl$$

$$FeOOH + 2\ Fe(OH)_2 \rightarrow Fe_3O_4 + 2\ H_2O$$

$$n_{Fe^{3+}} : n_{Fe^{2+}} : n_{OH} = 1:2:8$$

The diameter of the synthesized magnetite nanoparticles remains constant regardless of the concentration during the synthesis, however number of non-magnetic FeOOH nanorods increases with a concentration. The extent of undesired oxidation of Fe^{2+} ions to Fe^{3+} and the creation of the additional FeOOH anisotropic nanorods was observed with an increasing concentration of final Fe_3O_4 particles in the reaction batch (Figure 18). Despite interesting anisotropy of FeOOH nanorods, no sufficient response to magnetic field was observed. And thus, concentration of Fe_3O_4 was kept as low as 0.05 mol/l to keep their concentration low.

Precipitated brownish-black nanoparticles were let to sediment and water suspension was decanted several times to remove soluble salts. Then particles were vacuum filtered and washed three times gradually with a water, ethanol and acetone. Particles were kept at semi-wet form in the final third washing with an acetone to prevent their solid aggregation in dry powder.

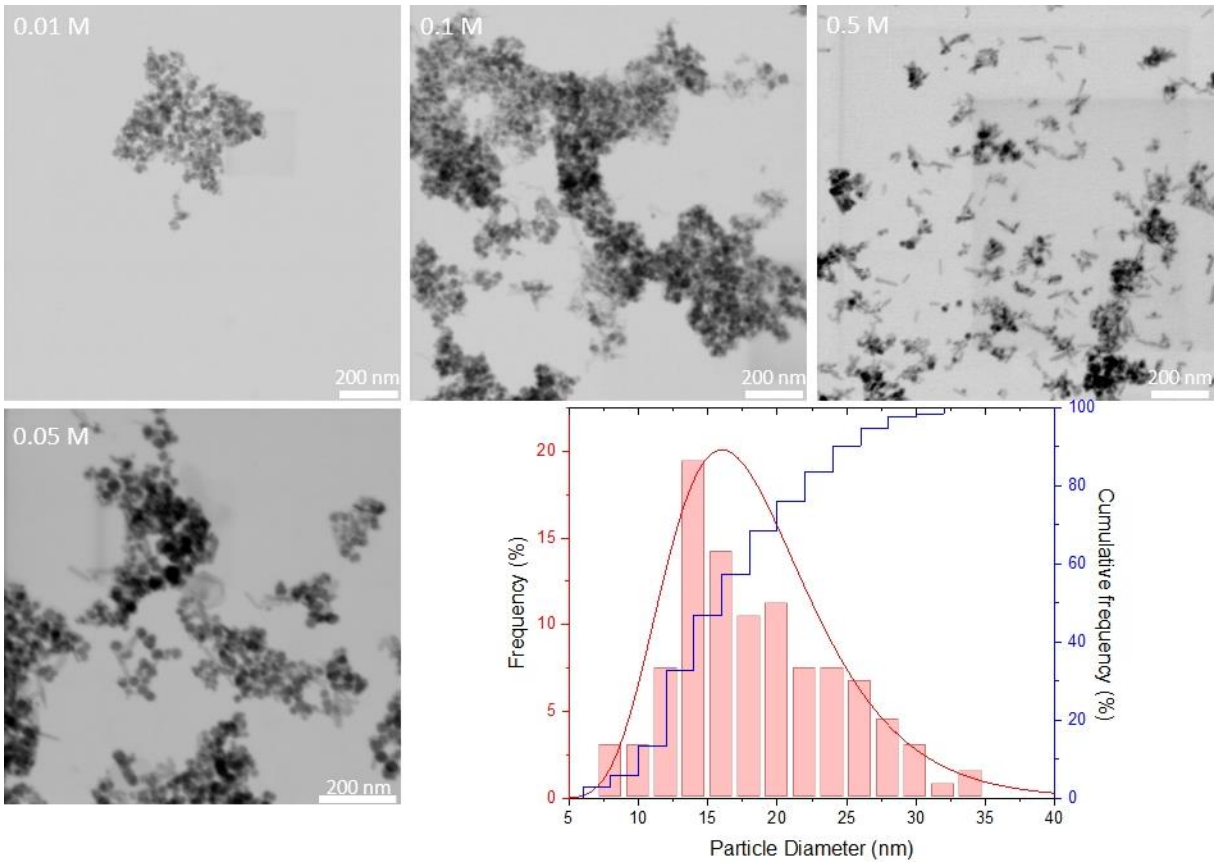

Figure 18 The morphology of the synthesized magnetic nanoparticles (in aggregates) with an increasing concentration of the final Fe_3O_4 in the reaction volume (indicated in images). Synthesized magnetite nanoparticles at concentration 0.05 M and lognormal particle diameter distribution.

2.2 Magnetic apparatus

Solenoid electromagnet with 939 turns of a copper winding was built for the generation of the magnetic field (Figure 19A,B). DC power supply E3633A (Keysight, USA) was used for the controlled generation of the electric current. Magnetic field strength (*H, B*) along centre axis of the solenoid was calculated via Equation (3). Three-axial Hall probe was used for measurement of the magnetic field strength in centre of the solenoid (0,0) as a function of current (Figure 19D, Table 1) and its gradient along the middle axis of the solenoid (Figure 19E). The experimentally measured magnetic field generated by the electric current I=5 A is presented in Figure 19E with a perfect fit of Equation (3). Inset in Figure 19E shows a cross-section simulation of the magnetic flux density (B) in the middle plane of the solenoid. Finite Element Model Magnetics (FEMM 4.2) software was used for the simulation of the magnetic field in the solenoid. Samples were prepared in area of the homogeneous magnetic field.

$$B = \mu H = \mu \frac{NI}{2l(d_2 - d_1)} \left[(l+2x) ln \frac{d_2 + \sqrt{d_2^2 + (l+2x)^2}}{d_1 + \sqrt{d_1^2 + (l+2x)^2}} + (l+2x) ln \frac{d_2 + \sqrt{d_2^2 + (l-2x)^2}}{d_1 + \sqrt{d_1^2 + (l-2x)^2}} \right] \quad \text{Equation (3)}$$

Where, B is the magnetic induction in (T), H is the magnetic field strength in ($A \cdot m^{-1}$), μ is the permeability of air, N is the number of wire turns, I is the electric current, l is the solenoid length, d_2 and d_1 are the outside and inner diameter, respectively and x is the position along the solenoid axis with a respect to its center (x=0, y=0).

Table 1 Magnetic field strength (H) and magnetic induction (B) of generated magnetic field by the electromagnet as a function of current (I).

I (A)	0	0.96	1.92	3.85	4.81	5.77	7.69	9.61
H ($A \cdot m^{-1}$)	0	3979	7958	15915	19894	23873	31831	39789
B (mT)	0	5	10	20	25	30	40	50

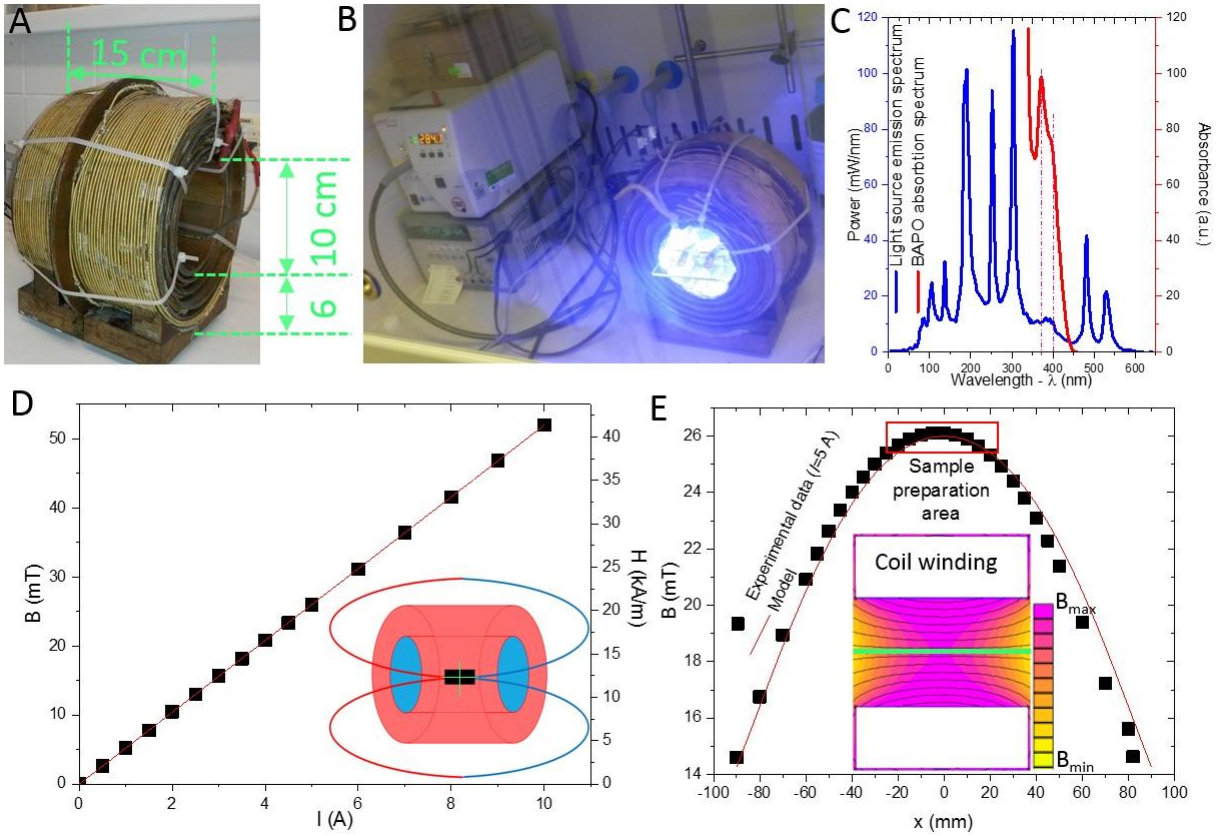

Figure 19 (A) Electromagnet used for the sample preparation and (B) apparatus used for the photopolymerization in the magnetic field. (C) Emission spectrum of the light source OmniCure S2000 (blue line) and the absorption spectrum of BAPO initiation (red line). (D) Generated magnetic field in the centre of solenoid (x,y=0,0) as a function of the current. (E) Experimentally measured magnetic field along the centre axis of the solenoid (y=0) and model fit from Equation (3), I=5 A. Inset shows a cross-sectional simulation of the magnetic flux density in FEMM 4.2 software.

2.3 Sample preparation

2.3.1 Polyurethane samples

Polyurethane samples with a commercial grade polyurethane matrix Gaform R30 (Dawex Chemical, Czech Republic) and commercial grade magnetite nanoparticles – 100 nm Fe_3O_4 (Sigma-Alrdich) were prepared by mixing of MNPs with a polyol part of the polyurethane resin for 1 hour. Then this mixture was ultrasonicated for additional 1 hour with ultrasonic homogenizer Sonoplus HD 3200 (Bandelin, Germany). Equivalent weight amount of diisocyanatane monomer was added to the polyol part (1:1 by weight). Resin was then mixed for 1 min by mechanical stirring and then dosed into the silicone mould. Moulds were immediately inserted into the homogenous area of solenoid and let to be cured for 30 min at laboratory temperature. The magnetic field was applied for the entire time of the assembling. Time up to the solidification was controlled by the curing reaction after part A and B is mixed together and it is strictly given as 5 minutes – gel point. Samples were post-cured at elevated temperature 80 °C for 2 hours to be fully cured and then demoulded.

2.3.2 Photopolymer samples

Photocurable resin was composed from two methacrylate monomers. The first one is poly(ethylene glycol) dimethacrylate (PEGDMA) (99 %, Sigma-Aldrich, USA), with a molecular weight of PEG part, $M_{n(PEG)}$=750 g·mol^{-1}. This corresponds approximately to n=16 PEG units in the backbone of the molecule and total molecular weight of monomer molecule is M_r=904.0 g·mol^{-1}. Ethoxylated bisphenol A dimethacrylate monomer (bis-EMA) (>87%, Esschem Europe, United Kingdom) with a molecular weight M_r=496.6 g·mol^{-1} was used as a second monomer. Monomers were mixed in the molar ratio 22/78 and 1 molar % (0.75 wt. %) of phenylbis(2,4,6-trimethylbenzoyl)phosphine oxide (BAPO) (97%, Sigma-Aldrich, USA) was added into the mixture of the monomers as a photo initiator absorbing the light on the edge of blue and UV range with a strong absorption at 371 and 400 nm (*268*). The absorption spectrum of the UV initiator is in Figure 19C – red line. Monomers and UV initiator were used as received and exact composition of photopolymer resin is listed in Table 2. The photocurable resin mixture was used as the master batch for the preparation of PNCs. The chemical structure of the monomers, photo initiator and experimental measurement of thermal transitions temperatures (T_g, peak of tan δ and plateau of tan δ) for PEGDMA/bis-EMA blends as a function of the molar composition is in Figure 20.

Table 2 Composition of the photopolymer resin.

Component	ρ (g·cm^{-3})	M_r (g·mol^{-3})	w (%)	ϕ (%)	x (%)	x_1* (%)
bis-EMA	1.12	496.58	65.99	62.72	77.50	78.32
PEGDMA	1.13	904.00	33.26	31.39	21.50	21.68
BAPO	1.19	418.50	0.75	5.89	1.00	-

*- molar ratio between bis-EMA and PEGDMA monomers

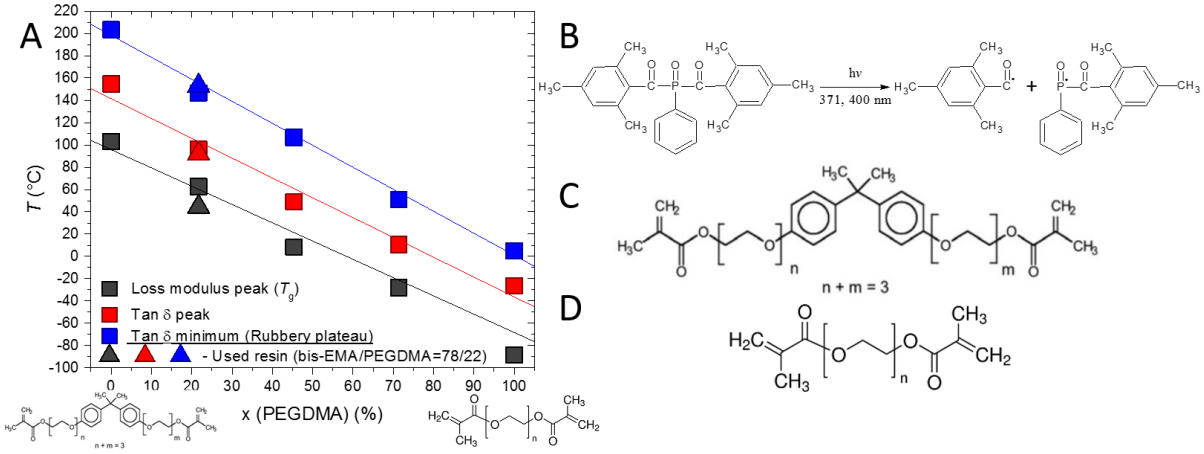

Figure 20 (A) Characteristic temperatures – glass transition, peak of tan δ and rubbery plateau for bis-EMA/PEGDMA copolymer blends as a function of PEGDMA monomer molar content. (B) Reaction scheme of photoinitiator (BAPO) α-cleavage by the UV absorption. (C) bis-EMA and (D) PEGDMA monomers.

The synthesized magnetite nanoparticles were used as a magnetic filler in photocurable polymers and colloids. The weight of particles corresponding to 1 or 2 vol. % was added into 40 ml of the photopolymer resin and subjected to continuous ultrasound dispersion for 1 hour with ultrasound homogenizer Sonoplus HD 3200 (Bandelin, Germany) while rapid cooling of suspension. Residual acetone was removed by the vacuum rotary evaporation at laboratory temperature while reaction mixture was shielded against the light to avoid the photopolymerization in thin layers on the walls of the flask. After the removal of acetone, the particle suspension in photopolymer was subjected to second step of continuous ultrasound dispergation for 5 hours with ultrasound homogenizer Sonoplus HD 3200 (Bandelin, Germany) while rapid cooling of suspension.

Small volume of the particle suspension was drop casted between two quartz glass microscopy slides covered with a thin cellophane foil. The mould was placed on quartz glass platform in the center of the solenoid. Magnetic assembling was conducted in this area. Magnetic field (B=0, 5, 25, 50 mT) was applied for entire time of the sample preparation. After certain time of magnetic irradiation (t_a=0, 5, 10, 20, 30, 60, 300 sec) for the particle assembly, UV light generated by the light source OmniCure S2000 (Excelitas Technologies, USA) was applied for 5 minutes for each side of the sample. The emission spectrum of the UV source is in Figure 19C – blue line. Walls of solenoid were covered with an aluminium foil for the light reflectance (Figure 19B). Intensity of emitted light was measured as 40 $mW \cdot cm^{-2}$ in the sample preparation area. After photopolymerization, thin film samples were demoulded and post cured in a vacuum oven at 100 °C for 1 hour under vacuum.

2.3.3 Colloid samples

Colloid samples were prepared by suspending of Fe_3O_4 nanoparticles in acetone (99.99 %, Verkon, Czech Republic) and corresponding amount of PMMA was dissolved in acetone suspension. Weight ratio between PMMA and Fe_3O_4 was set to 5 wt. %. Then concentrated

suspension was diluted and final Fe_3O_4 concentrations were obtained as listed in Table 3. Suspensions without PMMA showed problematic aggregation and sedimentation hence no experiments were done with this system. Concentration was measured by weight measurement of the suspension before and after the solvent evaporation in a vacuum oven at laboratory temperature. Volume of 15 µl of suspension was drop casted by automatic pipet onto silicon substrate placed in the center of the solenoid and magnetic field was immediately switched on. Acetone evaporation took approximately ~40 seconds. Assembled structures were analyzed by the scanning electron microscopy as prepared on the silicon substrates.

Table 3 Concentration (c) and volume fraction (ϕ) of Fe_3O_4 nanoparticles and PMMA in the acetone colloid suspensions. Particle volume fraction as a function of the concentration (in plot).

Sample	$c_{Fe_3O_4}$ (µg/ml)	$\phi_{Fe_3O_4}$ (vol. %)	c_{PMMA} (µg/ml)	ϕ_{PMMA} (vol. %)
c_1	356.0	$7.1 \cdot 10^{-3}$	19.0	$2.2 \cdot 10^{-5}$
c_2	189.0	$3.8 \cdot 10^{-3}$	10.0	$1.2 \cdot 10^{-5}$
c_3	130.0	$2.6 \cdot 10^{-3}$	7.0	$8.1 \cdot 10^{-6}$
c_4	97.0	$2.0 \cdot 10^{-3}$	5.0	$6.0 \cdot 10^{-6}$
c_5	39.0	$7.8 \cdot 10^{-4}$	2.0	$2.4 \cdot 10^{-6}$
c_6	19.0	$3.9 \cdot 10^{-4}$	1.0	$1.2 \cdot 10^{-6}$

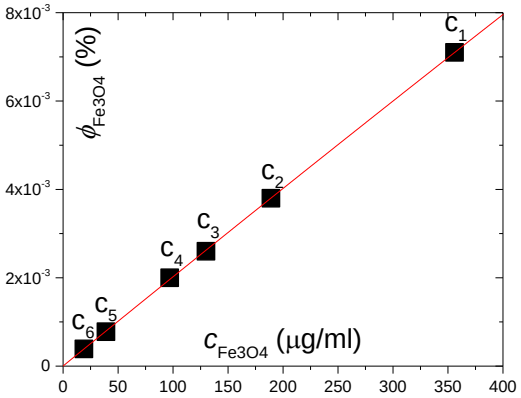

2.4 Structural analysis

The morphology and size of particles, structure of the nanocomposites and particle assemblies was investigated by the scanning electron microscope (SEM) Mira3 XM (TESCAN, Czech Republic) in secondary electrons (SE), back-scattered electrons (BSE) and/or in transmission mode (STEM). Also, high-resolution transmission electron microscope (HR-TEM) TITAN Themis (FEI, USA) was used. Samples for SEM were polished using TEM Mill 1050 (Fischione Instruments, USA) and very thin layer of the sample surface was milled off for the structures to be observable by the electron microscopy. Thin slices for STEM and HR-TEM were prepared by Ultramictome EM UC7 (Leica Microsystems, Germany). Nanoparticles were drop casted from the diluted acetone suspension onto the carbon film coated TEM grid or deposited on the SEM sample holder. Particle assemblies from the colloid suspensions were deposited onto Si wafers and analyzed as prepared. The structure of polyurethane composites was investigated by the optical microscope LEXT OLS 10 000 (OLYMPUS, Japan).

2.5 Dynamic mechanical analysis

Dynamic mechanical analyzer for the solid samples RSA G2 (TA Instruments, USA) was used for the measurements of thermo-mechanical properties of the samples in tension with an axial deformation of ε=0.05 %, frequency f=1 Hz and top-down temperature ramp from 170 °C to -100 °C with a cooling rate 5 °C/min. Cooling from 170 °C was used to erase thermal history of

the sample. Geometry of thin film photocured samples was as follows: loading gap l=10 mm, width w=6 mm and film thickness t=80 μm. At least two samples were used for the measurements and their mean value with a standard deviation is presented. Measurements exhibits good repeatability when a single sample is measured multiple times.

2.6 Thermal properties

The volume fraction of MNPs in PNCs was checked with a thermo-gravimetric analyser Discovery TGA (TA Instruments, USA). Samples were heated in N_2 atmosphere up to 1000 °C with 10°C/min heating rate and polymer was thermally decomposed.

Thermal processes in the photopolymer samples (glass transition, melting) were analysed by differential scanning calorimeter Discovery DSC (TA Instruments, USA). Heating and cooling rate were set at 5 °C/min – to simulate the conditions from the DMA measurements. 10 mg of sample was enclosed in aluminium pan. The sample was firstly cooled down to -80 °C. Then it was heated to 170 °C and cooled down back to -80 °C – the first heating and cooling cycle. Secondly, sample was heated back to 170 °C and cooled down to -80 °C – the second heating and cooling cycle. Analyses show very uncertain and insignificant glass transition. Also, no crystallization was observed during cooling cycles.

2.7 Magnetic properties

Magnetic properties of the magnetic nanoparticles were measured with a use of Mini Cryogen-Free Magnet System (Cryogenic Limited, United Kingdom) at the laboratory temperature T=298 K (temperature of assembling). The magnetization hysteresis curves for the commercial and synthesized MNPs are in Figure 21A,B. Both, synthesized and commercial Fe_3O_4 particles, exhibit a ferrimagnetic behavior with a hysteresis of magnetization and remanence. Synthesized magnetite shows initial non-zero magnetization in zero field state with a value M_w=1.53 emu·g^{-1}. Minority magnetization curves were measured up to 2 T showing gradual non-linear increase of minority saturation magnetization, with M_m^S=88.2 emu·g^{-1} (or A·m^2·kg^{-1}) at B=2 T (Figure 21D). Minority saturation and remanent magnetization can be satisfactorily fit with a linear function in the range of B=0-50 mT (B range of experiments). The slope of the linear fits represents the magnetic susceptibility of the material and/or extent of orientation of the magnetic moments, $M_v=\chi_v H$, see Figure 21E,F. The temperature dependence of the magnetization for the synthesized magnetite was measured from the laboratory temperature to T=3 K with an applied field B=2 T (Figure 21C).

The magnetic interactions between in-line aligned particles with a parallel orientation of their magnetic moments were modeled using finite difference micromagnetic code OOMMF (*269*). Magnetic moment of a single nanoparticle M=9.74·10^{-19} A·m^2 was calculated from the saturation magnetization (M^S=88.2 emu·g^{-1}) and used for the simulations. Spherical magnetite particles with a diameter 16 nm were approximated by two-dimensional cylinders of identical diameter, mass and volume. Energy of collective magnetic interactions was solved for two,

three, five and seven particles which are aligned in one line. Surface-to-surface distance between particles was set to: 32, 20, 12 and 4 nm.

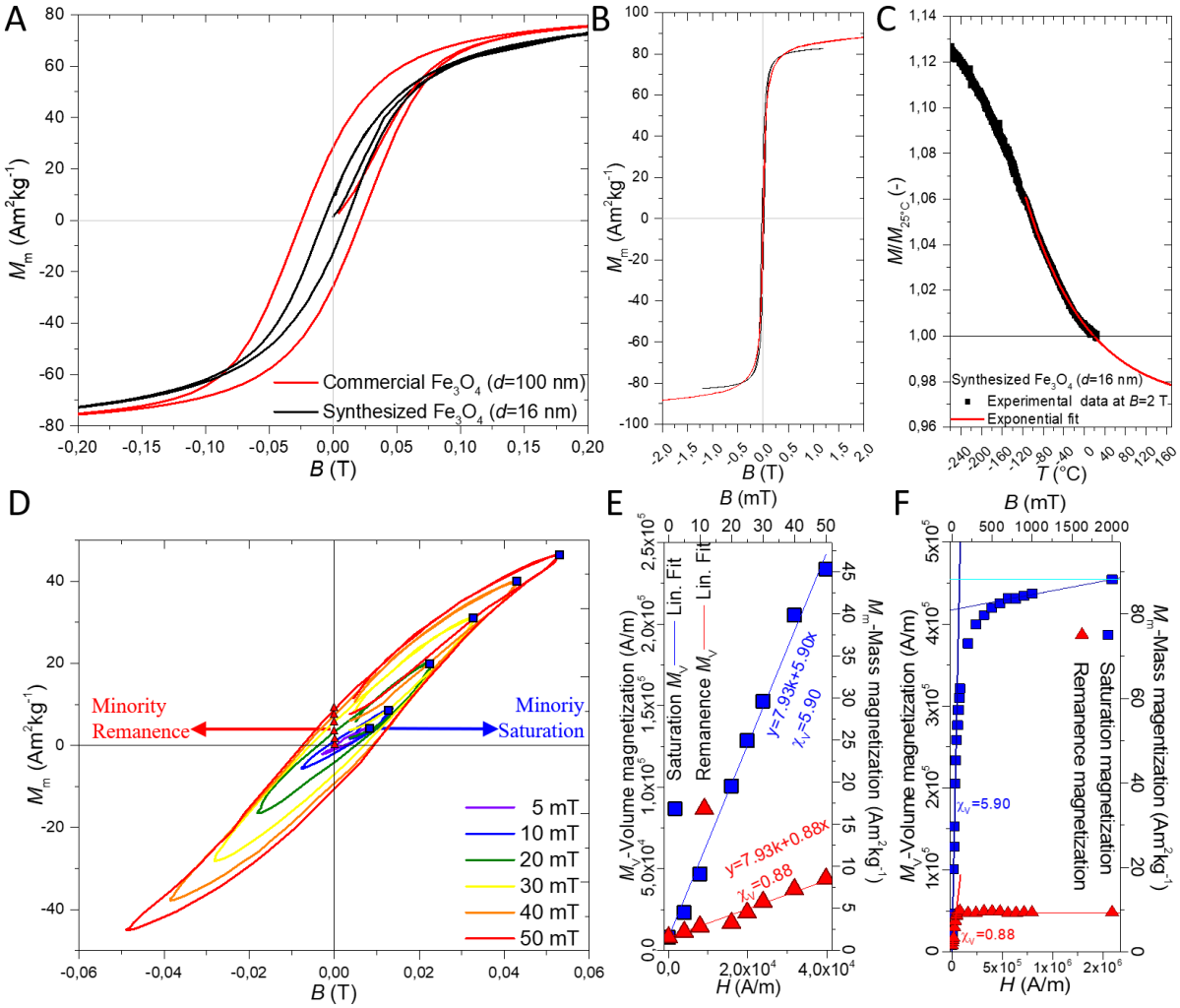

Figure 21 (A,B) Magnetization hysteresis curves for used magnetic nanoparticles. (C) Temperature dependence of the magnetization response for the synthesized magnetite nanoparticles at *B*=2 T normalized to signal at *T*=25 °C. (D) Minority hysteresis curves for the synthesized nanoparticles in the field range *B*=5-50 mT. Minority saturation and remanent magnetization of the synthesized nanoparticles up to (E) *B*=50 mT and (F) *B*=2 T

3 Results and discussion

3.1 Structure

In the following chapters, structure formation governed by the magnetic interactions is discussed in detail.

3.1.1 Self-assembly aggregation, *B*=0 mT

The mixing of magnetic nanoparticles with a photo curable methacrylate resin allowed the solidification of the PNCs in thin sections by a relatively fast photopolymerization within the seconds. The structures resulted from the self- and directed self-assembly in magnetic field are thus very quickly fixed by the solid polymer network. However, longer exposure times were used to promote the yield of the photopolymerization reaction followed by the thermal post-curing (see 2.3.2 in Materials and methods section). Assembling time (t_a) was conveniently controlled by the time up to the light exposure. The structural parameters such as a width, length and/or volume of the magnetically assembled structures dramatically depends on multiple processing parameters such as a particle loading, intensity of magnetic field, MNP's susceptibility, viscosity (*104, 146*) and assembling time (*138*). Nevertheless, homogeneity, size and shape of primary building blocks derived from the quality and stability of the initial particle dispersion seem to be the most important parameters among others (*106*). Description of the aggregation process of MNPs in the system without an application of the magnetic field is attempted in the order to elucidate the size and shape of the primary building blocks and aggregation dynamics. For this purpose, electron microscopy images are analyzed and attractive interparticle potentials are calculated. Aggregation of magnetic nanoparticles accompanied the sample preparation of all systems investigated in this dissertation thesis (colloid, polyurethane, photopolymer) due to no additional chemical stabilization of MNPs in the polymer liquids.

Initial self-assembled structures exhibit relatively extensive aggregation of MNPs into sub-micron irregularly shaped assemblies with small aggregates (quasi isotropic, composed from few particles) homogenously distributed in the sample volume (Figure 22). Lower particle loading, 1 vol. %, exhibits rather isolated particle aggregates (Figure 22A) in contrary to 2 vol. % sample with considerably bigger and microscopically percolated particle structures (Figure 22B). In the case of self-assembled systems, synthesis of PNCs was conducted in absence of the external magnetic field, except of the Earth's magnetic field which is $B \approx 50$ μT and it is not expected to cause any significant effects on the assembling process. The adsorption of low molecular weight photopolymer monomers (M_r=496.6 g·mol^{-1} and 904.0 g·mol^{-1}) such as used in the experiments apparently cannot sufficiently stabilize the particle dispersion by the steric repulsion despite the presence of numerous polar bonds in PEG chains and ester bonds (~**CO–O**–CH_2–CH_2–**O**~). It will be later shown that close MNPs are spaced with a thin layer of polymer and structures are something between aggregate and cluster.

Non-zero magnetization (remanence) measured by the magnetometer (Figure 21) significantly contributes to the interparticle interactions and consequently to irreversible particle aggregation

in colloid suspension with complex aggregation dynamics. Remanence suggests sort of magnetic stabilization and non-superparamagnetic response. Initial non-zero magnetization of the particles in the moment of the sample's insert to the magnetometer with a zero applied field exhibits value of M_m=1.51 emu·g^{-1}. The physical meaning of this value needs to be addressed. Absolute value of magnetic moment of single particle, *M* is constant and independent of the applied external magnetic field at given temperature. Hence, particle is always surrounded by its magnetic field. Its value does not change since atomistic structure of MNP remains unmodified. Moment oscillates within the lattice of MNP (Néel's oscillation) and/or it exhibits non-parallel orientation with an external field of magnetometer. This results in lower macroscopic magnetic response of the material. The increase of magnetization with a field is caused by the gradual orientation of the moments in the field direction. In the saturation state (in high magnetic fields), maximum extent of magnetic moments alignment is achieved (Figure 4A). From the values of the saturation magnetization (M_m^S=88.2 emu·g^{-1}), the magnetic moment bear by single particle with a mass m=1.104·10^{-17} g is calculated as M=9.74·10^{-19} A·m^2. The magnetic moments can be oriented in the field direction by: *i*) alignment within the crystalline structure of MNP and/or *ii*) Brownian rotation of whole MNP when the moment is energetically locked in favorable crystalographic axis. In the case of contact aggregation of multiple particles, Brownian rotation is more difficult/slower due to larger viscous force of the surrounding medium insert on the particle aggregate (*59*).

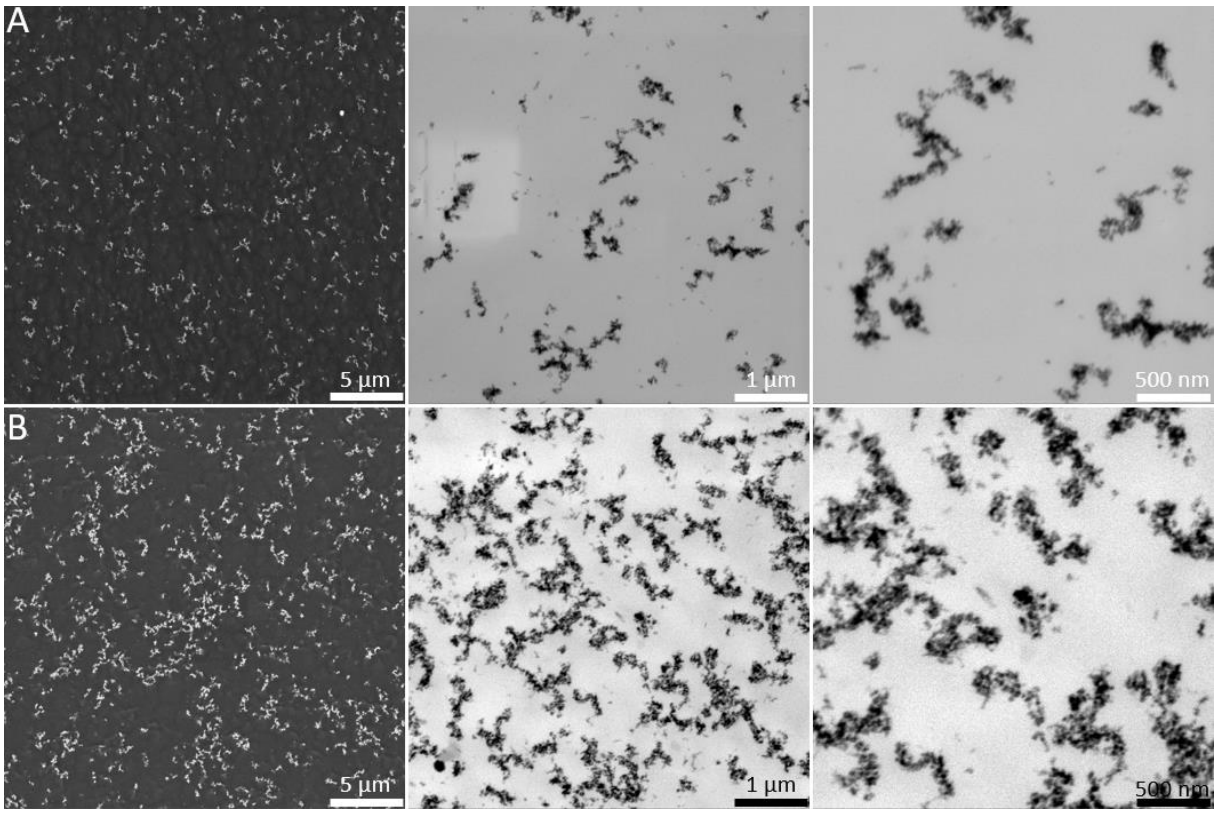

Figure 22 Electron microscopy images of the particle structure in the photopolymer matrix at filler loading (A) ϕ=1 vol. % and (B) ϕ=2 vol. % in absence of the external magnetic field, B=0 mT. BSE and STEM modes, magnification: 10k, 50k and 100k x.

Problematic dispersion and spontaneous aggregation of MNPs in photopolymer matrix (*154, 270, 271*), other polymer solutions and melts (*59, 81, 138, 272-275*) has been reported also previously by numerous researchers. Despite particle surface stabilization utilizing various strategies such as a grafting, surface treatment with long hydrocarbon acids/salts or simple usage of bare untreated particles, aggregation is observed even at very low particle loadings. It needs to be mentioned that using of the surface stabilization with molecules incompatible/immiscible with a polymer matrix or solvent catastrophically influences the stability of the system resulting in opposite effect than desired dispersion – phase separation/flocculation (*59, 138*). The addition of third phase – polymer into the colloid MNPs dispersion seems to be more complicated situation. Remanent magnetization measured at the zero field accompanied by the particle aggregation was experimentally observed by Robbes, et al. (*273*) for γ-Fe_2O_3 larger than d>50 Å and Bharti, et al. for 20-30 nm γ-Fe_2O_3 (*67*) (see their Supporting Information and dispersion states). However, effect of magnetic interactions on the aggregation process was not studied.

It was shown that aggregation of MNPs in liquid polymer matrix undergoes two steps aggregation process (*137, 273*). In the first step, primary aggregates composed from few of particles (for example 10) are created via interparticle interactions such as van der Waals, or electrostatic (including the magnetic attraction is highly reasonable). In the second step, primary aggregates form the secondary fractal aggregates as a volume fraction of MNPs increases above ϕ>0.01 vol. %. In the case of our experiments, existence of primary aggregates is not entirely clear and it can be caused by two factors:

i) Insufficient dispersion of the MNPs from the semi-wet powder in which van der Waals interactions acting on very short interparticle distances in a combination with a magnetic attraction may be sufficient stabilization factors preventing the breakdown of primary aggregates into individual particles during sonication.
ii) Magnetic interactions arising from their non-zero magnetic moments can attract adjacent dispersed particles and contribute to aggregation significantly. This applies also for the growing aggregates.

Few isolated, most probably kinetically entrapped, self-assembled structures consisted from several particles with a diameter ~50-100 nm and little bit larger ~150 nm for ϕ=1 and 2 vol. %, respectively were found within the polymer matrix (Figure 23A,B). Small number of even smaller (few particle) aggregates and single particles were found during the analysis of multiple STEM images at high magnifications, but the presence of these objects is rather exceptional and rare (marked with arrows in Figure 23C). Despite the origin of the primary aggregates (dispersion of powder vs. self-assembly aggregation) is uncertain, these small objects are building blocks for any other structures which further grow in the system with or without the external magnetic field. They either exist in the colloid suspension from the beginning or they are formed very quickly. Fractal-like aggregates in this work such as those in Figure 22 were created by a complex multi-step aggregation of smaller particle structures into large fractal

aggregates with an irregular shape and size as depicted in Figure 23C. Two populations of primary aggregates of different shape and size were observed. The isotropic spherical (in Figure 23C marked with red dotted line) and anisotropic aggregates with elliptical shape a slightly larger number of particles and volume (in Figure 23C marked with orange dotted line). Recently, similar multi step and bottom-up aggregation processes were also studied in different self-assembled non-magnetic systems (*238-240*).

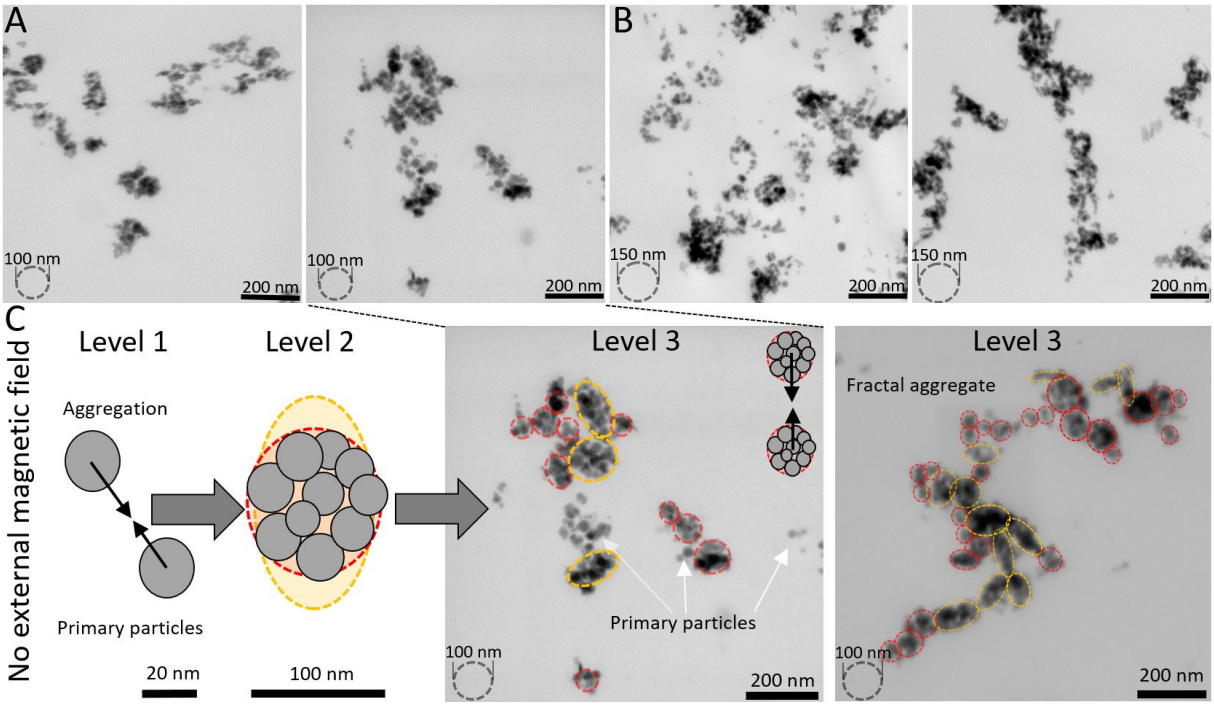

Figure 23 Few isolated self-assembled aggregates in the photopolymer matrix containing (A) ϕ=1 vol. % and (B) ϕ=2 vol. % of MNPs. (C) Schematic representation of the proposed multi step self-assembly aggregation in the sample with ϕ=1 vol. % of particles. Assembling process starts from the primary particles (Level 1) forming two population of aggregates (Level 2): *i*) isotropic primary aggregates with almost circular shape and diameter in the range d=50-100 nm (red dotted line) and *ii*) larger anisotropic assemblies (orange dotted line). Finally, assembly of the individual aggregates and particles into sub-micron aggregates and complex shaped fractal aggregates (Level 3).

Jiao and Akcora (*274*) studied the aggregation process in the system with PS grafted Fe_3O_4 nanoparticles in solution of PS. Particle loading was kept approximately at ϕ~1 vol. %. Energy of van der Waals and dipolar magnetic attraction between Fe_3O_4 nanoparticles with a diameter 8 nm and short interparticle distance Δl=2 nm (center-to-center distance, l=10 nm), were calculated as U_{vdW}~1k_BT and $U_{mag.}$~0.8k_BT, respectively. Under these conditions, it is obvious that magnetic dipole attraction plays less significant role in the aggregation process compared to van der Waals attraction. Anyway, it needs to be mentioned that such short interparticle distances for 8 nm particles are reasonable to be assumed only at very high particle loadings (above ~7-12 vol. %), assuming that initial dispersion of particles is homogeneous and MNPs are randomly packed in the volume (*203, 207*). It is surprising that both energies are less or the

same order than the thermal energy nevertheless, aggregated structure is obtained even at very low particle loadings under certain grafting parameters. Robbes, et al. (*139*) also observed spherical aggregates of γ-Fe_2O_3 at very low particle concentration (ϕ<0.05 vol. %) in absence of the external magnetic field despite grafting with PS chains. This arises additional questions regarding the dispersion and aggregation process of MNPs: *i*) *What is the role of the magnetic interactions*? *ii*) *What is successful way for the dispersion of MNPs (grafting versus surface stabilization)?* leading to more general question in the field of PNCs *iii*) *What is the role of grafted and/or adsorbed polymer chains on the surface of the NPs on the aggregation process and dispersion stability*? Obviously, grafted and/or adsorbed polymer chain can contribute to balance of energetic equilibrium by various effects, mainly entropic ones (*272*) and offer possibility how to construct defined structures which was studied by Akcora, et al. (*16*). In addition to this, balance of interactions between particle-polymer-solvent has crucial effect on structure governing mechanisms which seem to be non-trivial (*23*). Interplay between grafting density, molecular weight and dipolar forces was found to have strong impact on the morphology of self-assembled particle aggregates while string-like particle structures are formed in PS matrix at low grafting density (*274*). Anisotropic self-assembled aggregates were also observed in our systems under zero magnetic field and generally, large particle aggregates create anisotropic arms and/or whole aggregate shows dominant elongated backbone (see Figure 22, Figure 23). Anisotropic self-assembled structures are in good correlation with a theoretical prediction from the work of Hynninen and Dijkstra (*104*) on the assembling of the spherical dipolar particles in electric or magnetic fields. The thermo-dynamical phase diagram shows a region with string like particle structures at low particle concentrations even for dipolar interactions strengths<<1 (Figure 7B). In this simulation work, strictly homogeneous system easily reaching its thermo-dynamical equilibrium was taken into a consideration while structuring in the polymer solutions might be more complex.

Other experimental works studying the assembling of magnetic particles (*81, 105, 107, 138, 154, 270-274*) uses significantly prolonged assembling times and thus more time to reach the thermo-dynamic equilibrium. Hindering the thermo-dynamic equilibrium by kinetical entrapment of particles and their aggregates in a solid photopolymer within couple of seconds of assembling needs to be taken into a consideration. As well viscous effect of photopolymer liquid (η_0=0.7 Pa·s) and interlocking by the particle-particle solid contacts can introduce additional kinetical barriers for MNPs to reach the thermo-dynamically stable structure within the time scale of the experiment. As a result, kinetically entrapped, irregular shaped sub-micro aggregates are created. Just to give a picture, instability of initial particle dispersion is mentioned. Particle dispersion transforms from perfectly optical transparent systems to flocculated agglomerates visible by bare eye (in thin section) after couple of minutes after sonication is switched off. This suggests complex aggregation process of nanoparticles driven by common aggregation mechanisms which are present in colloid NPs systems and enhanced significantly by non-zero magnetic interactions in the case of MNPs. Unfortunately, kinetics of structure formation for self-assembled systems were not further studied and no structural

information regarding the aggregation kinetics is available. Also, relatively fast aggregation and dynamic transition of the system complicate an analysis of the initial system (t_a=0 sec) by scattering methods because these techniques require certain time to scan the spectrum.

3.1.1.1 Van der Waals and magnetic energy

To address the relative strength of van der Waals and magnetic interactions on the aggregation process, corresponding energetic potentials were calculated and normalized to thermal energy (Equation (4)). Electrostatic interaction is neglected. Mean interparticle surface-to-surface distance (*203*) and mean shortest interparticle surface-to-surface distance (*207*) for randomly packed spheres is used assuming homogeneous initial dispersion of MNPs at filler loading ϕ=1 and 2 vol. %. Calculated interparticle distances are summarized in Table 4 or see Figure 24A.

Energy of van der Waals attraction between magnetite nanoparticles is calculated according to Equation (5) (*272*).

$$U_{\mathrm{Thermal}} = k_{\mathrm{B}}T \qquad \text{Equation (4)}$$

$$U_{\mathrm{vdW}} = -\frac{A}{12}\left[\frac{d^2}{l^2-d^2} + \frac{d^2}{l^2} + 2ln\left(1-\frac{d^2}{l^2}\right)\right] \qquad \text{Equation (5)}$$

$$\gamma = \frac{U_{\mathrm{vdW}}}{U_{\mathrm{Thermal}}} = \underbrace{\left|-\frac{A}{12}\left[\frac{d^2}{l^2-d^2} + \frac{d^2}{l^2} + 2ln\left(1-\frac{d^2}{l^2}\right)\right]\right|}_{\text{van der Waals Energy}} \Big/ \underbrace{k_{\mathrm{B}}T}_{\text{Thermal Energy}} \qquad \text{Equation (6)}$$

Where A is Hamaker constant ($A_{Fe_3O_4}$ =2.1·10^{-19} J (*272*)), d is the particle diameter and l is the center-to-center interparticle distance. Boltzmann constant k_B=1.38·10^{-23} J·K^{-1}, temperature of assembling process T=298.15 K.

Magnetic energy between two particles with a parallel moment orientation (θ=0 °) was calculated according to Equation (7) (*58, 66, 67, 107*).

$$U_{\mathrm{Mag.}} = \frac{\mu_0 M^2(1-3cos^2\theta)}{4\pi l^3} \qquad \text{Equation (7)}$$

$$\lambda = \frac{U_{\mathrm{Magnetic}}}{U_{\mathrm{Thermal}}} = \underbrace{\left|\frac{\mu_0 M^2(1-3cos^2\theta)}{4\pi l^3}\right|}_{\text{Magnetic Energy}} \Big/ \underbrace{k_{\mathrm{B}}T}_{\text{Thermal Energy}} \qquad \text{Equation (8)}$$

Where μ_0 is the magnetic permeability of free space μ_0=4π·10^{-7} H·m^{-1}, magnetic moment bear by a single particle M=9.74·10^{-19} A·m^2 and θ is the angle between magnetic moment and center-to-center interparticle distance (θ=0°).

Both energies were normalized to thermal energy (Equations (6) and (8)) and their normalized values in the units of thermal energy are plotted as a function of interparticle surface-to-surface distance in Figure 24B.

Table 4 Mean interpaticle surface-to-surface (Δl) and center-to-center (l) distances at investigated filled fraction ϕ=1 and 2 vol. % for the magnetite nanoparticles with a diameter d=16 nm assuming the random particle packing and energy of corresponding van der Waals (γ) and magnetic dipolar energy (λ) normalized to thermal energy.

	Mean interparticle distance					Mean shortest interparticle distance				
ϕ (%)	$\Delta l/d$ (-)	Δl (nm)	L (nm)	γ (-)	λ (-)	$\Delta l/d$ (-)	Δl (nm)	l (nm)	γ (-)	λ (-)
1.0	~1.95	31.2	47.2	$2.6 \cdot 10^{-3}$	0.44	~1.14	18.24	34.24	0.02	1.15
2.0	~1.40	22.4	38.4	$9.6 \cdot 10^{-3}$	0.81	~0.70	11.20	27.20	0.11	2.30

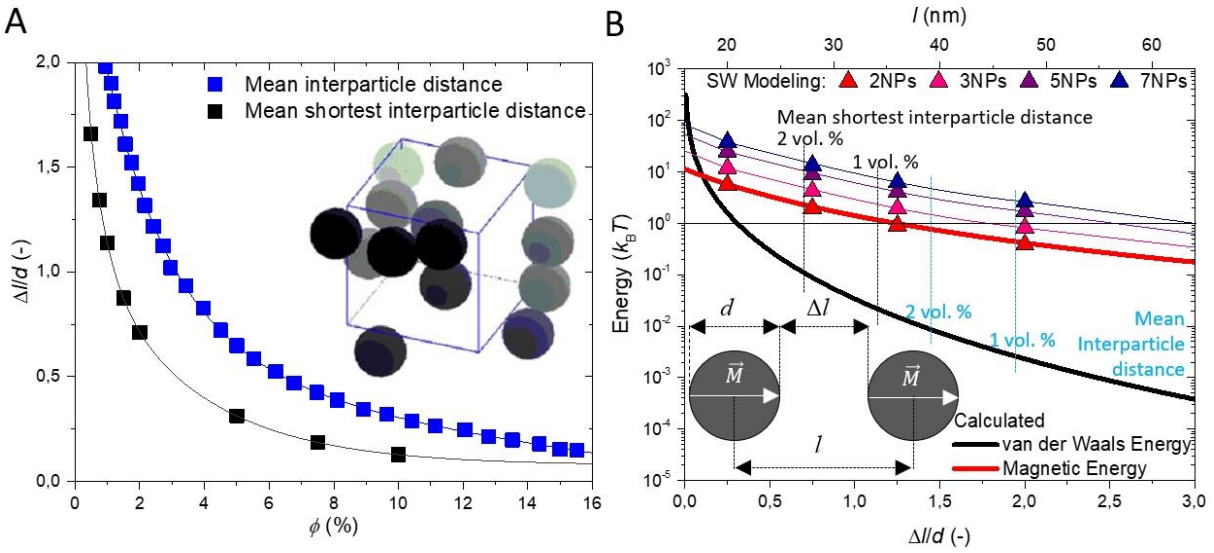

Figure 24 (A) Mean interparticle distance normalized to the particle diameter as a function of filler volume fraction, data acquired from ref. (*203, 207*). Inset shows structure of PNC with a random particle packing. Reprinted from ref. (*203*), Copyright 2010, with permission from Elsevier. (B) Calculated van der Waals (solid black line) and magnetic interaction energy (solid red line) between two MNPs, d=16 nm as a function of their interparticle distance in the units of thermal energy ($k_B T$). Inset depicts the particle arrangement. Triangles represent micromagnetic simulations of mutual magnetic interaction energy for increasing number of in-line aligned MNPs: 2–red, 3–pink, 5–purple and 7 MNPs – blue.

Energy of van der Waals attraction scales with an interparticle distance and it significantly contributes to aggregation only at very short interparticle distances. vdW energy dramatically overcomes the effect of long-range magnetic attraction bellow Δl<1.75 nm. Even shorter interparticle distances can be found in the particle aggregates and vdW interactions can be strong stabilizing forces holding the aggregates together. On the other hand, van der Waals interactions become too weak above Δl>5 nm to overcome the thermal motion of the particles and these forces are not strong enough to bring the remote MNPs to close contact.

Magnetic interactions contribute to aggregation significantly on much longer ranges when compared to van der Waals attraction and contributes to aggregation process of two 16 nm magnetite particles up to interparticle distance Δl=20 nm at which λ=1. Magnetic energy for mean shortest interparticle distances satisfactorily falls to the aggregation region (λ>1) while energetic values for mean interparticle distance remain still in diffusion region (λ<1). Reported mean values of the interparticle distances (*203, 207*) are used for the prediction of distance in system containing MNPs (Table 4). But interparticle distances exhibit much broader distribution of interparticle distances and consequently also much shorter distances than reported mean values exist in the system (*276, 277*). After all, this can be seen also in depiction of the model PNC system containing randomly packed spheres in inset of Figure 24A. Various stochastic processes leading to decrease of the spacing are expected to be present in the liquid system as well. During sonication of colloid suspension, particles can approach close proximity due to vigorous viscous flow of the system. In addition, particles can randomly diffuse and decrease/increase interparticle separation by simple thermal diffusion. And most importantly, on contrary to magnetic attraction, magnetic repulsion should be also taken into an account as highly possible situation when two adjacent particles with a repulsing moment arrangement (see Figure 5) are repealed from each other. This consequently can bring one of them closer to another magnetic particle or aggregate and in final, it can decrease the spacing between them down to the point of no return.

Analytically calculated magnetic interaction assumes interaction only between two MNPs with identic orientation of magnetic moments. As the number of neighboring particle increases, the magnetic interaction becomes stronger due to collective interaction. Micromagnetic simulation of magnetic dipolar interaction energy for two particles agrees perfectly with the analytically calculated magnetic interaction energy. Simulated collective interactions further exhibit an increase in magnetic energy with increasing number of neighboring particles. Consequently, the capturing radius beyond which magnetic energy overcomes thermal energy and particles aggregate by magnetic interactions increases. Orientation of magnetic moments is set to be aligned in the same direction and particles are arranged in one line with identic separation. The simulation of magnetic interaction energy for two (red triangle), three (pink triangle), five (purple triangle) and seven particles (blue triangle) is plotted in Figure 24B.

Systems with a particle loading of 0.1 and 1.0 vol. % were prepared also in polyurethane matrix. It is obvious that poor dispersion quality is obtained by the used preparation method and initial self-assembled system shows aggregated structure even at very low particle loadings with a size of aggregates of several micrometers while aggregation is more pronounced at higher particle concentration as interparticle distance decreases (Figure 34). Fe_3O_4 nanoparticles vigorously aggregated also from colloid acetone suspension during evaporation into micro sized aggregates within couple of seconds as no magnetic field was applied. This aggregation process was pronounced for larger particle concentrations and observable by bare eye. Irregular shaped aggregates are shown in the Figure 33 as well very small particle aggregates with sub-micro size that can be considered as primary aggregates.

3.1.2 Magnetically assembled structures

The application of magnetic field triggered rapid assembling of magnetic building blocks into anisotropic chain-like assemblies with a homogeneous orientation controlled by the external magnetic field. In the magnetic field, particles rapidly form various types of structures and their mutual interactions are enhanced as magnetic moments are more aligned in direction of the field when compared to zero field sample. Magnetic building blocks create stronger local magnetic field resulting from the contribution of external field and magnetization of particles aggregates according to Equation (9). In zero external field this local field is generated only by the remanent magnetization of building blocks. Values of local magnetic field generated by MNPs are listed in Table 5. Higher extent of alignment, longer and larger structures are assembled under higher external magnetic fields as can be seen in Figure 25. The anisotropic structures are perfectly oriented in the field direction. One-dimensional structures are gradually merged in longitudinal and lateral direction and create superstructures under intense external fields, higher particle loading or extended assembling times (kinetic will be discussed further in text).

$$B_{\mathrm{local}} = \mu(H + M_{\mathrm{V}}) = B + \mu M_{\mathrm{V}} \qquad \text{Equation (9)}$$

Table 5 Intensity of external magnetic field (*B*, *H*) with a measured volume magnetization of synthesized magnetite (M_v), and relative magnetization normalized to saturation magnetization (M/M_S). Generated local magnetic field (B_{local}) around the assemblies and magnetic/thermal energy ratio (λ_0).

B (mT)	*H* ($A \cdot m^{-1}$)	M_v ($kA \cdot m^{-1}$)	M/M_S (-)	B_{local} (mT)	λ_0 (-)
0	0	7.93	0.02	9.96	$3{,}43 \cdot 10^{-3}$
5	3979	23.18	0.05	34.12	$2{,}93 \cdot 10^{-2}$
25	19894	128.54	0.28	186.53	$9{,}01 \cdot 10^{-1}$
50	39789	233.78	0.52	343.77	$2{,}98 \cdot 10^{0}$
2000	1.59M	454.24	1.00	2570.82	$1{,}13 \cdot 10^{1}$

The images of electron micrographs were analysed in ImageJ software to obtain the volume of the structures, their length and diameter (width) resulting in the aspect ratio. These structural parameters for analysed structures are reported in Figure 27.

3.1.2.1 Assembling in low magnetic field, *B*=5 mT

At a low particle concentration, ϕ=1 vol. %, magnetic structures are elongated along the field direction and assembled into superstructures guided by the low magnetic field, *B*=5 mT. These superstructures are formed from the individual aggregates interconnected by head to tail magnetic interactions acting between them (Figure 25). These superstructures are homogenously oriented along the field direction and individual building aggregates can be

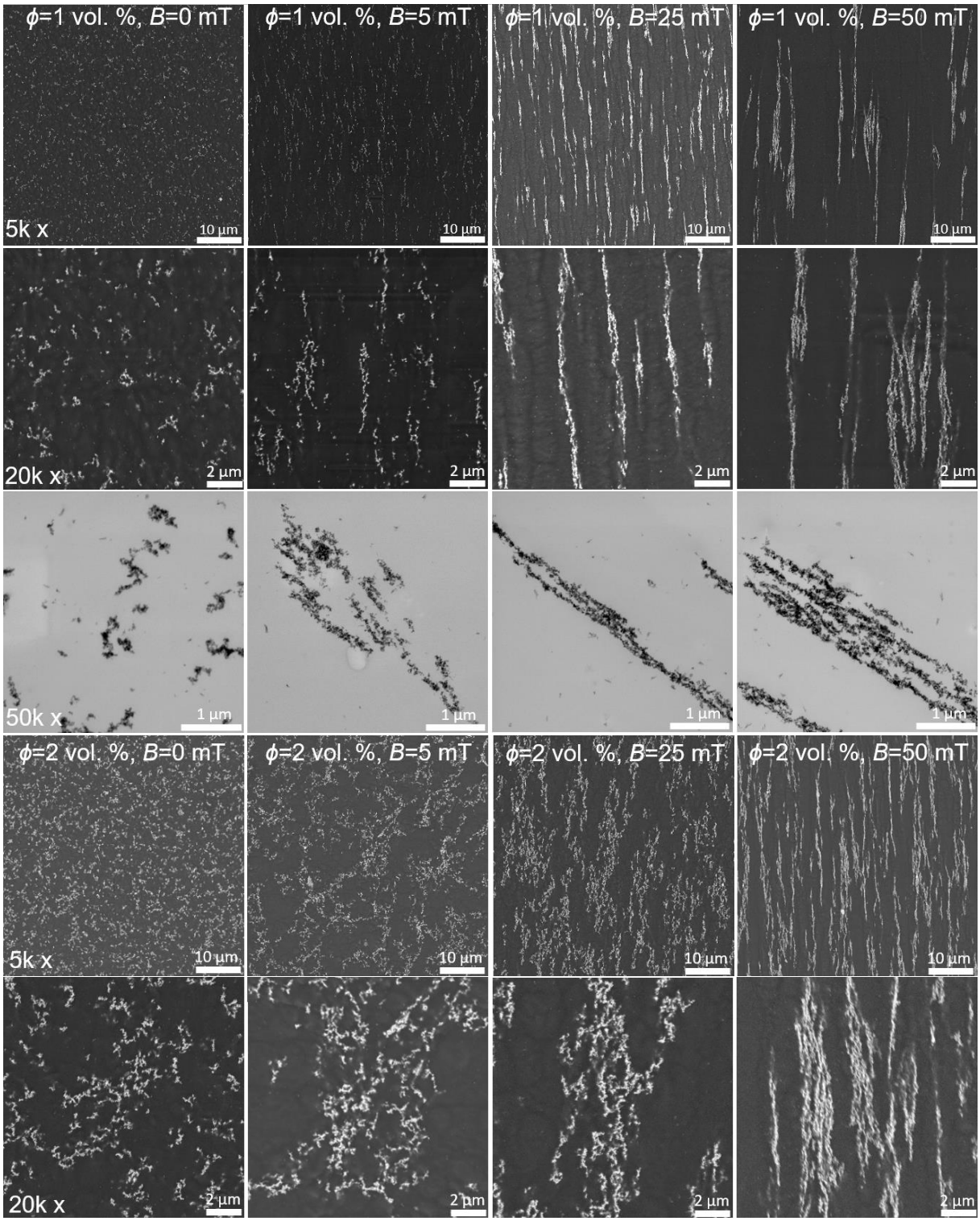

Figure 25 SEM and STEM images of self-assembled structure in absence of external magnetic field and magnetically directed self-assembled structures in presence of external magnetic fields B=5, 25 and 50 mT at particle loading ϕ=1 and 2 vol. %, after t_a=10 sec. Images at increasing magnification: 5k, 20k× in BSE and 50k× in STEM mode.

distinguished clearly from the SEM images (Figure 26B). Spacing polymer is also visible in the images – marked with arrows. Analysis of the structure's dimensions shows surprisingly similar volume distribution of the aggregates assembled in the absence of magnetic field (B=0 mT) and

low magnetic field (*B*=5 mT). See Figure 27 and Figure 26A,B for the comparison and basic difference between these two systems. Particle assemblies in the low magnetic field are slightly smaller, but their backbone is well aligned in the field direction. To the contrary, backbone of the self-assembled aggregates shows curved and/or complex shape (Figure 26A). In addition to large magnetic structures observed in both cases, relatively large number of small and individual aggregates are visible in the electron micrographs (few particle large). Two processes proceed simultaneously in this system with a low magnetic field: *i*) self-assembly aggregation of MNPs and *ii*) their magnetic alignment. Low external magnetic field, *B*=5 mT, rather results in the concentration, straightening and chaining of adjacent (self-assembled) neighbouring aggregates into large superstructures along the imaginary force lines of the magnetic field while self-assembly process has a major effect on the growth of individual aggregates.

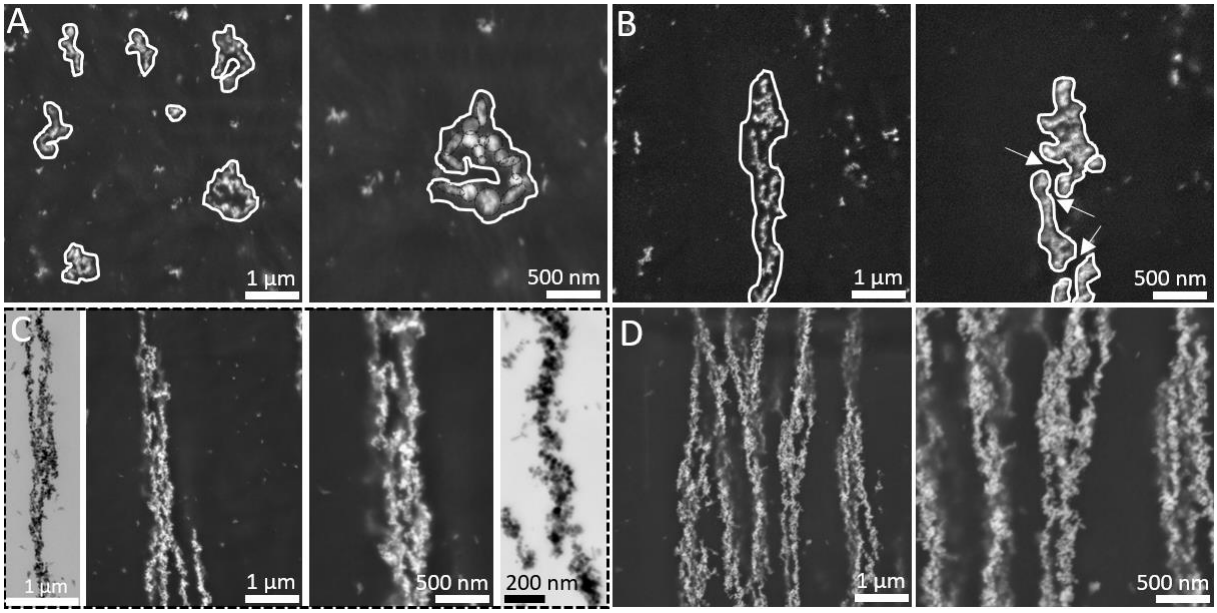

Figure 26 (A) The structure of self-assembled PNC with 1 vol. % of MNPs in absence of the magnetic field and (B) in low magnetic field, *B*=5 mT. White lines restrict (A) the self-assembled aggregates and (B) superstructure which is composed from many smaller anisotropic self-assembled aggregates spaced by a thin layer of polymer indicated by white arrows in right-B image. The superstructure of magnetically assembled PNC with 1 vol. % of MNPs in magnetic field (C) *B*=25 mT and (D) *B*=50 mT created by entangling of multiple magnetic chains.

Robbes, et al (*139*) studied directed self-assembly of PS grafted γ-Fe_2O_3 nanoparticles in colloid suspension of PS in applied magnetic field (*B*=10 and 60 mT). Sample was vitrified bellow boiling point of dimethylacetamide solvent for relatively long time – 8 days. Despite grafting of MNPs with PS chains, very small self-assembled particle aggregates are formed. In the magnetic field, their anisotropy is developed. Isolated chain-like particle assemblies consisted from several particles at low loadings (ϕ=0.05 vol. %) and percolated fractal-like particle aggregates interconnected with short lateral branches at increased particle loadings (ϕ=1-3 vol. %) were fabricated in the PS matrix (see Figure 10G,H).

In our case, structures do not percolate on the macroscopic scale due to depletion of the particles during more extensive primary aggregation – building blocks of magnetically aligned structures are much larger. However, increased loading of MNPs, ϕ=2 vol. %, shows transition from the anisotropic sub-micro aggregates to microscopically percolated assemblies (Figure 25) with no preferential alignment or anisotropy which is further developed after the extended assembling times (Figure 29). These microscopic flocculates are created by the drag and concentration of the magnetic material in one spot and thus large particle-free domains are formed (Figure 25 and Figure 29). Results from this work prove this procedure with a very fast processing technology as a promising method for the generation of the anisotropic fractal-aggregates in polymer liquids induced by very low magnetic fields or even by a remanent magnetization carried by MNPs.

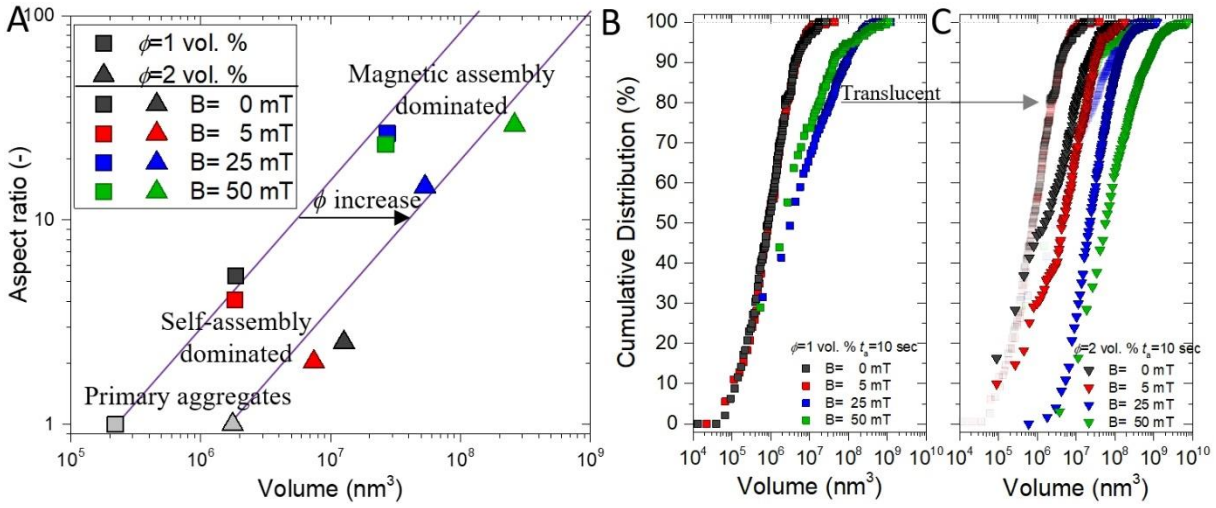

Figure 27 (A) Mean volume versus mean aspect ratio for the structures assembled after t_a=10 sec. Cumulative distribution of structure volume (B) for ϕ=1 vol. % and (C) for ϕ=2 vol. % assembled after t_a=10 sec. In (C) translucent data represent ϕ=1 vol. % for the comparison.

3.1.2.2 Assembling in higher magnetic fields, *B*=25 mT and *B*=50 mT

Increase of magnetic field to *B*=25 mT and 50 mT led to more rapid organization of MNPs into well-developed anisotropic structures with a high aspect ratio (in the system containing ϕ=1 vol. %). Magnetic material is concentrated along the imaginary force lines of the field. Again, structures are homogenously oriented with a long axis of the magnetic chain backbone aligned along the direction of the applied magnetic field. From both SEM and STEM images (Figure 25), it is clearly seen that these superstructures are built from individual particle chains that are several particles wide and micrometres long. These one-dimensional structures interact with each other by head-to-tail magnetic interactions creating longitudinally interconnected superstructures. This process increases the volume, length of the structure and inter structure spacing significantly (see Figure 27). The widening of the structures is caused by an instability of repulsive interchain magnetic interactions which results in their lateral merging and formation of chain junctions (see Figure 26C,D). This is especially visible for the strongest magnetic field, *B*=50 mT. Large magnetic structures are surrounded by stronger magnetic field

while smaller assemblies have a higher mobility in viscous matrix. Growing structures gradually attract and absorb smaller magnetic building blocks from 3D area around them during the magnetic directed self-assembly and increase their volume (*67, 146*).

The diameter of the magnetic chains is very close to diameter of primary aggregates found in nanocomposites (Figure 23A,B). The mean width of individual structures is D=109±41 and 113±53 nm, for B=25 mT and 50 mT, respectively. As can be seen, the length (L) of the structures can reach as high as tens-hundreds of micrometres. With a diameter ~100 nm, aspect ratio (L/D) of the structures easily exceeds the values ~100. However, mean values of chain's aspect ratio lie around ~25-29 due to presence of shorter structures (see Figure 25 for B=25 and 50 mT in low magnification). This is more evident and frequent for the structure assembled under B=50 mT. The length of some particles assemblies considerably exceeds the length of those assembled under B=25 mT but lot of relatively short and thick particle chains are found in the system as well, which consequently decrease mean length/aspect ratio when compared to system assembled under B=25 mT. As well, these structures show larger extent of lateral merging but they still remain mainly individual with a spacing polymer between them (Figure 26D). Additional lateral merging of the structures is more obvious after extended assembling time or increased concentrations of MNPs (discussed further in text). The assembling of the individual particle chains into one dimensional particle superstructures is a perfect example of complex bottom-up built-up approach.

The application of 25 mT in the system containing higher particle volume fraction (ϕ=2 vol. %) lead to development of in-field elongated micro-percolated particle flocculates. The structure is very similar to the sample assembled under magnetic field 5 mT. The well-developed anisotropic chains are formed after prolonged assembling times and/or in increased magnetic field 50 mT (Figure 25).

Well-developed one-dimensional magnetic structures in polymer matrices by various vitrification protocols have been previously reported (*130, 138, 148, 164, 184*). Fragouli, et al. (*138*) assembled ~80 nm thick one-dimensional particle chains from γ-Fe_2O_3 in PEMMA matrix in magnetic field 160 mT. On the other hand, quite low particle loading was used, ϕ~0.25 vol. % and higher volume fractions, ϕ~1 vol. % show relative coarse structures. This is due decreased interparticle spacing and extensive aggregation enabling lateral merging of already big primary aggregates. This effect is even promoted by the longer assembling times which was required to evaporate the solvent (t_a>700 sec) and similar structures were observed further in our experiments under extended assembling times as well. In this dissertation work, one of the best dispersion qualities of MNPs in PNCs under studied conditions – particle loadings (ϕ=1 and 2 vol. %) and no particle stabilization is presented.

3.1.2.3 Kinetics of assembling and growth of superstructures

It is obvious that thermodynamically stable assemblies formed in the homogenous magnetic field are defined as anisotropic one-dimensional structures with a high aspect ratio. These structures may grow into two and three-dimensional structures with an increasing concentration

of MNPs or field strength. But the size and shape of the assembled structure can dramatically change with increasing time of assembling. The effect of the assembling time on the development and growth of the structure was mentioned several times in the previous text. In this chapter, the kinetic effect of magnetic assembling will be discussed.

Structural studies based on direct *in-situ* microscopy observation of growing structures in liquid matrix/environment (*65, 105, 146, 278-280*) provide relatively versatile and real-time information about the dynamics of the assembling process. Basically, three types of structures were observed in the view field of the optical microscope: i) isolated one-dimensional, ii) percolated one-dimensional and iii) two-dimensional ellipsoidal structures which were developed after longer assembling times (t_a>10 min.) and resulted in the coarsening of the system on the micro and macro scale (see Figure 7C) by Swan, et al. (*105*). But these results are limited by the resolution of used microscope, usually in micro meters for optical microscopy which hinders the *in-situ* observation of assembling process bellow sub-micro scale and/or short assembling times from nano colloids.

The kinetics of assembling process was studied *ex post* by electron microscopy of the cured samples (see Figure 29-31). Assembling time was controlled by the application of magnetic field after which samples were rapidly solidified by photopolymerization. Under short assembling times (i.e. t_a=10 sec.), large number of anisotropic structures are created due to chaining via north-south pole interactions. These structures produce three-dimensional magnetic field around them attracting and absorbing other structures around them which result in their lateral merging and growth (*67, 86, 146*). By kinetic entrapment (solidification), metastable structure can be preserved inside the matrix without reaching its stable configuration – obviously high aspect ratio micro chain perfectly aligned in the field direction.

For the low magnetic field B=5 mT and low particle loading ϕ= 1 vol. %, very slow process of structure growth is visible, especially at images of lower magnifications (Figure 29). Structures rather grow in direction of magnetic field and lateral merging starts to occur after longer assembling times (such as t_a>30 sec.) and with obvious lateral merging after very long assembling times, t_a=300 sec. The structure rapidly changes in the system with ϕ= 2 vol. %. Here, the switching of the low magnetic field attracted building blocks and increased their concentration in specific points promoting phase separation. This creates particle-free and particle-rich domains. On the other hand, the volume of magnetic objects does not dramatically differ from the self-assembled structure (Figure 27). With an increase of assembling time, situation changes and concentrated aggregates grow, elongate in the field direction and they are densified. Sort of particle micro web very similar to macroscopically percolated fractal-like aggregates is generated in the matrix. After prolonged assembling time, t_a=300 sec., drastic reconfiguration of the particle structure is observed. Particles are organized in microscopic chain-like structures with a homogeneous orientation while lateral branching diminish. This transition from the branched and percolated structure occurs somewhere in the range t_a=60-300 sec. This structure would slowly grow further to one-dimensional macro structure.

Considerably faster growth of the superstructures is observed for assembling in higher magnetic fields with substantial development of micro superstructures and coarsening of system within short time scales. The growth of the structures is clearly visible in Figure 30 and Figure 31 for B=25 and 50 mT, respectively. The transition from nano-/submicro- to micro- and macrostructure occurs within very short assembling times (t_a>30 sec.). These micro chain structures developed in the system are visible by bare eyes in the PNCs. Magnetic field B=25 mT forms micro chains in both particle concentrations (1 and 2 vol. %) after t_a=300 seconds, and these particle chains are stable. They also display a relatively large densification. In magnetic field B=50 mT, extremely large magnetite-rich micro islands are created via significant lateral merging after 300 seconds of assembling. Interaction of magnetic chains in lateral direction is significant for magnetic field 50 mT.

Two types of phase diagrams were constructed for the assembled structures which reflect metastable structures resulted from short assembling time (t_a=10 sec.) and prolonged assembling times which aim towards the thermodynamic equilibrium. Also, structures assembled from the acetone suspensions are presented in second diagram. These phase diagrams summarize resulted morphology of the structures in studied systems. Magnetic/thermal energy ratio is used as a scaling parameter versus particle volume fraction. Initial magnetic energy (λ_0) is calculated according Equation (7) using measured volume magnetization (M_v) as a function of magnetic field (see Table 5).

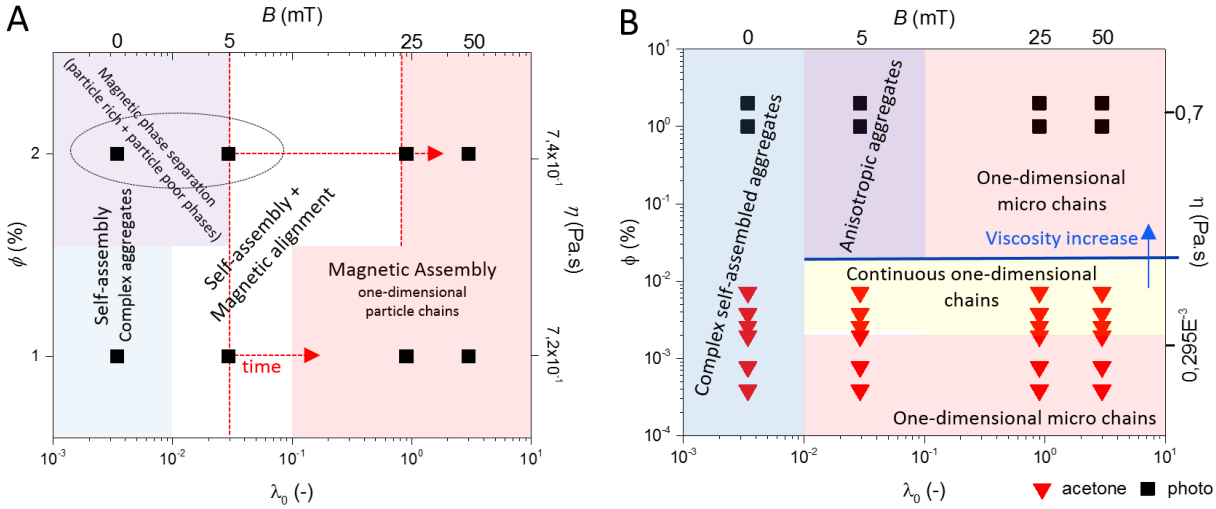

Figure 28 (A) Phase diagram for metastable structures in the photopolymer matrix (assembled after tens of seconds) and (B) phase diagram for stable structures assembled from acetone suspension (acetone), photopolymer (photo) assembled after prolonged assembling times when compared to (A). Both diagrams are in initial dipolar strength (λ_0) versus volume fraction (ϕ) representation.

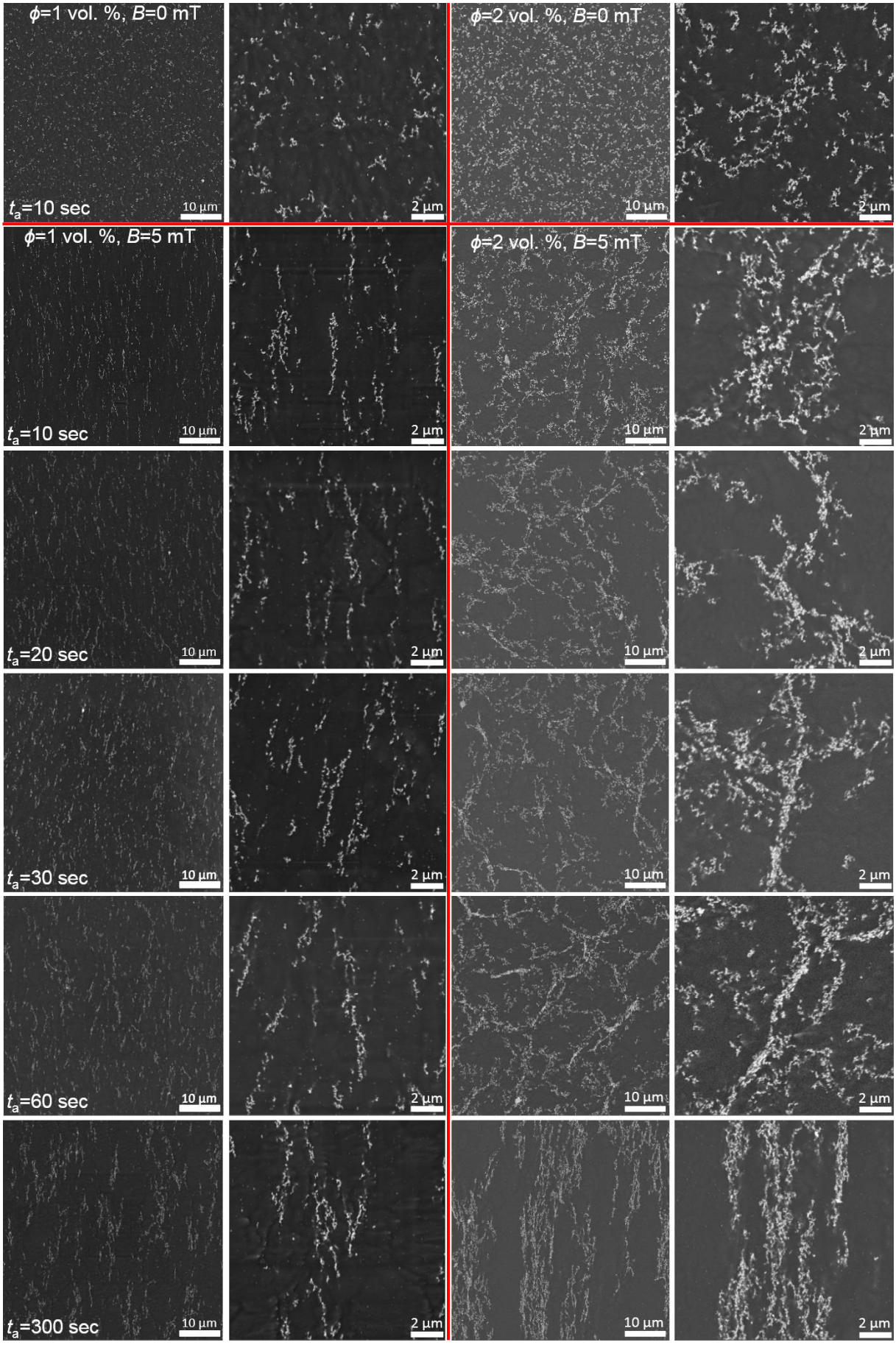

Figure 29 Electron micrographs of magnetically directed self-assembled structures in the photopolymer matrix containing 1 and 2 vol. % of Fe_3O_4 nanoparticles at the magnetic induction B=0 mT and B=5 mT after t_a=10, 20, 30, 60 and 300 seconds. Magnification 5k and 20k x in BSE mode is provided for each sample.

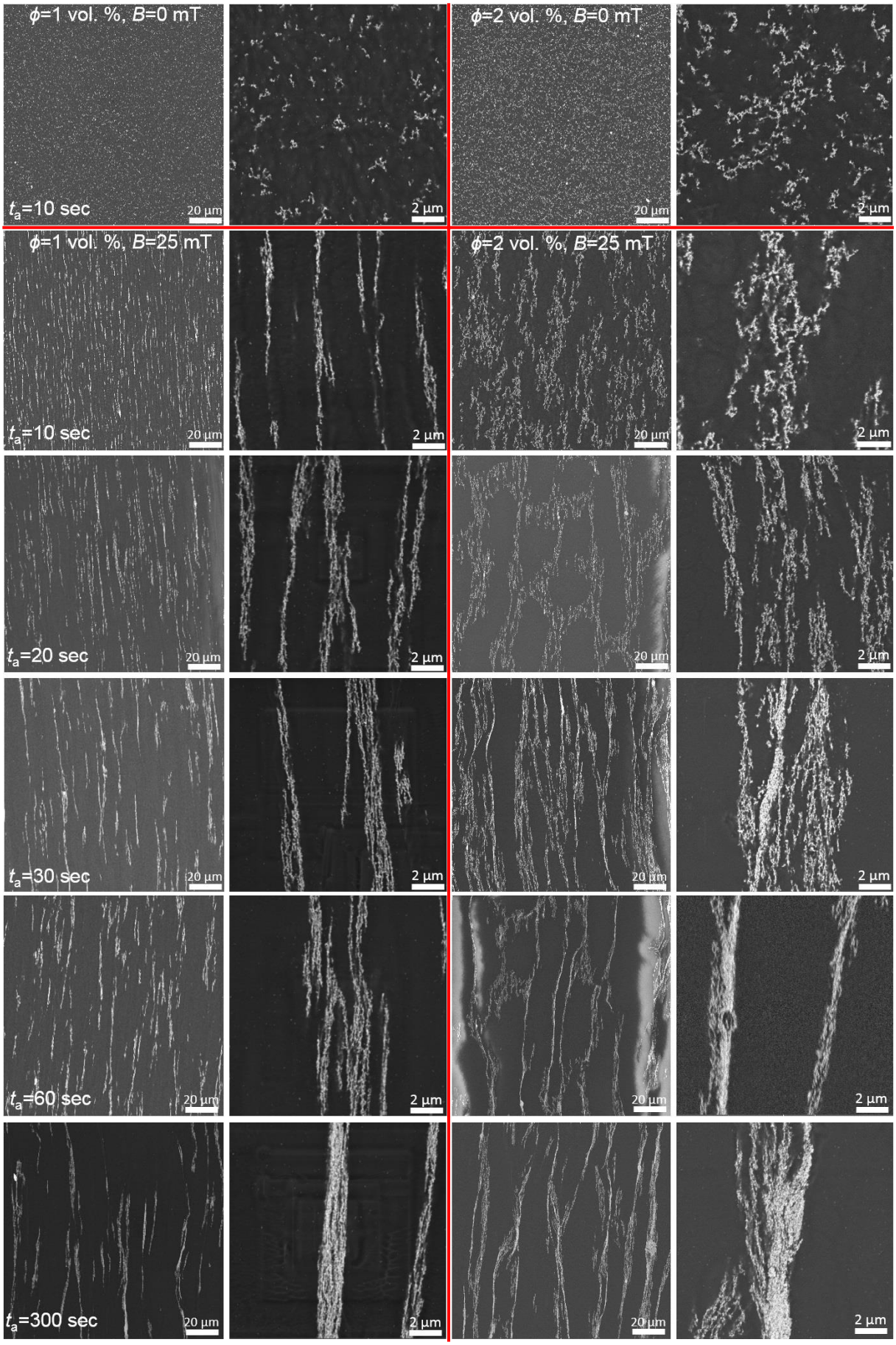

Figure 30 Electron micrographs of magnetically directed self-assembled structures in the photopolymer matrix containing 1 and 2 vol. % of Fe_3O_4 nanoparticles at the magnetic induction B=0 mT and B=25 mT after t_a=10, 20, 30, 60 and 300 seconds. Magnification 2k and 20k x in BSE mode is provided for each sample.

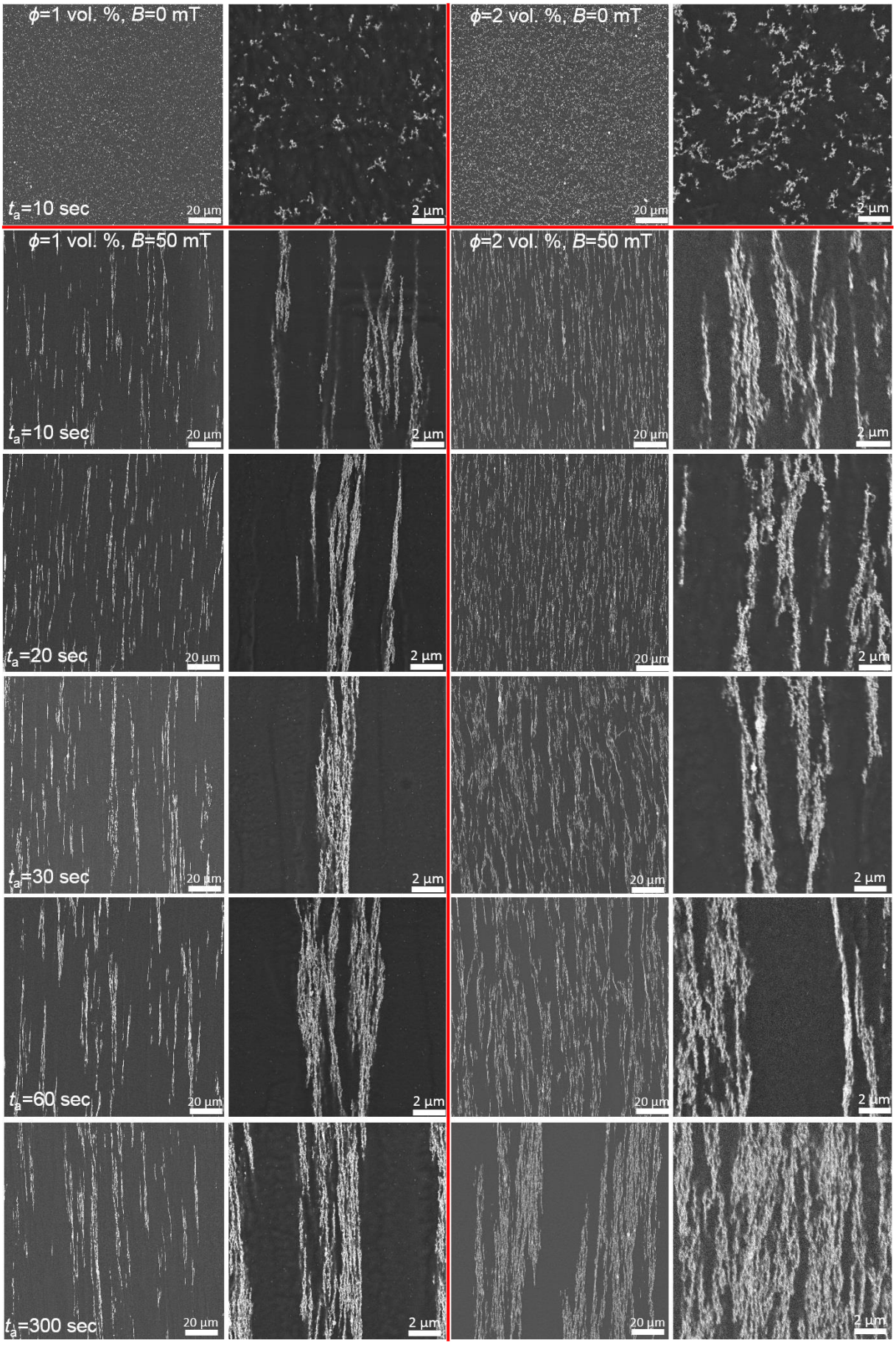

Figure 31 Electron micrographs of magnetically directed self-assembled structures in the photopolymer matrix containing 1 and 2 vol. % of Fe_3O_4 nanoparticles at the magnetic induction B=0 mT and B=50 mT after t_a=10, 20, 30, 60 and 300 seconds. Magnification 5k and 20k x in BSE mode is provided for each sample.

3.1.3 Colloid samples

Suspension of magnetic nanoparticles in presence of small amount of PMMA (5 wt. %≈20 vol. %) in acetone suspension were subjected to assembling in the magnetic fields with a strength *B*=0, 5, 25, 50 mT. Despite very low particle concentration (Table 3), large particle structures were obtained with different structural parameters depending on the particles concentration (see Figure 33). Low 1k and 10k x magnifications are provided for each sample.

In field free state, vigorous phase separation was observed within couple seconds as acetone stars to evaporate in zero field state. Large aggregates can be seen. After 40 seconds of assembling and acetone evaporation, the time is sufficiently long for the particle aggregation promoted by the magnetic attractions in low viscous acetone suspension (η_0~0.3 Pa·s). Also, acetone evaporation from the particle surface might play role in phase separation.

In the magnetic field, large one-dimensional structures bound by PMMA are formed. At highest concentration c_1, porous particle structures – latterly interconnected (entangled together) and clearly composed from individual particle chains are formed. Lateral percolation can be seen also for lower particle concentration $c_{2\text{-}4}$. The diameter of particle chains negligibly decreases with a particle concentration but remains still in order of several micrometres. Lateral interconnection of the chains vanishes at lower particle concentrations ($c<c_3$). Particle concentrations (c_1-c_3) results in the formation of continuous particle structures with a length spanning across the whole deposition area. Particle concentrations c_4-c_6 shows limited chain length with higher densification and less porosity – individual building magnetic chains are visible. Individual chains are wrapped together into large micro structures which is evidence of their bottom-up formation. In the proximity of large particle assemblies, these smaller sub-micro chains can be observed.

While PMMA bounds the structures and stays inside them for low PMMA concentration, the addition of higher amount of PMMA (such as 10 and 15 wt.%) led to interconnection of the magnetic chains by fine PMMA network (Figure 32). Figure 32D shows magnetic structure surrounded and embedded completely by the PMMA micro web with a small amount of MNPs.

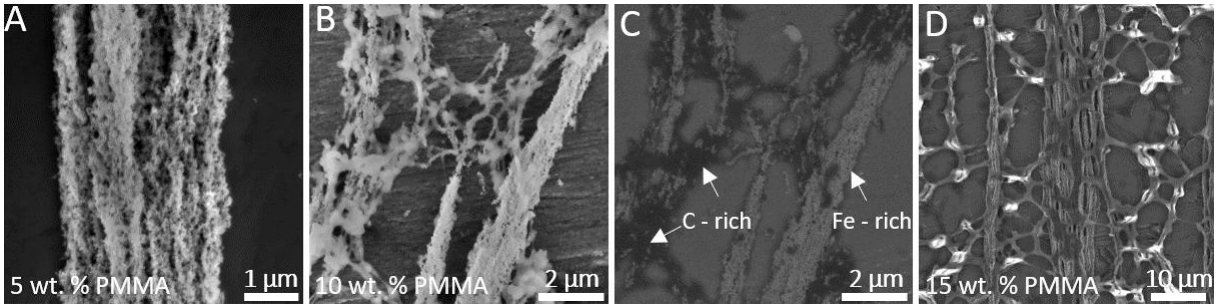

Figure 32 (A) Microstructure of the c_6 sample assembled in 50 mT magnetic field with 5 wt. % of PMMA. Microstructure of the sample with an addition of (B,C) 10 wt. % and (D) 15 wt. % of PMMA – images from SE mode. (C) Image of the structure in BSE mode. Dark areas indicate a matter containing atoms with a low atomic number such as carbon (PMMA) and brighter areas indicate areas containing atoms with a high atomic number such as Fe (MNPs).

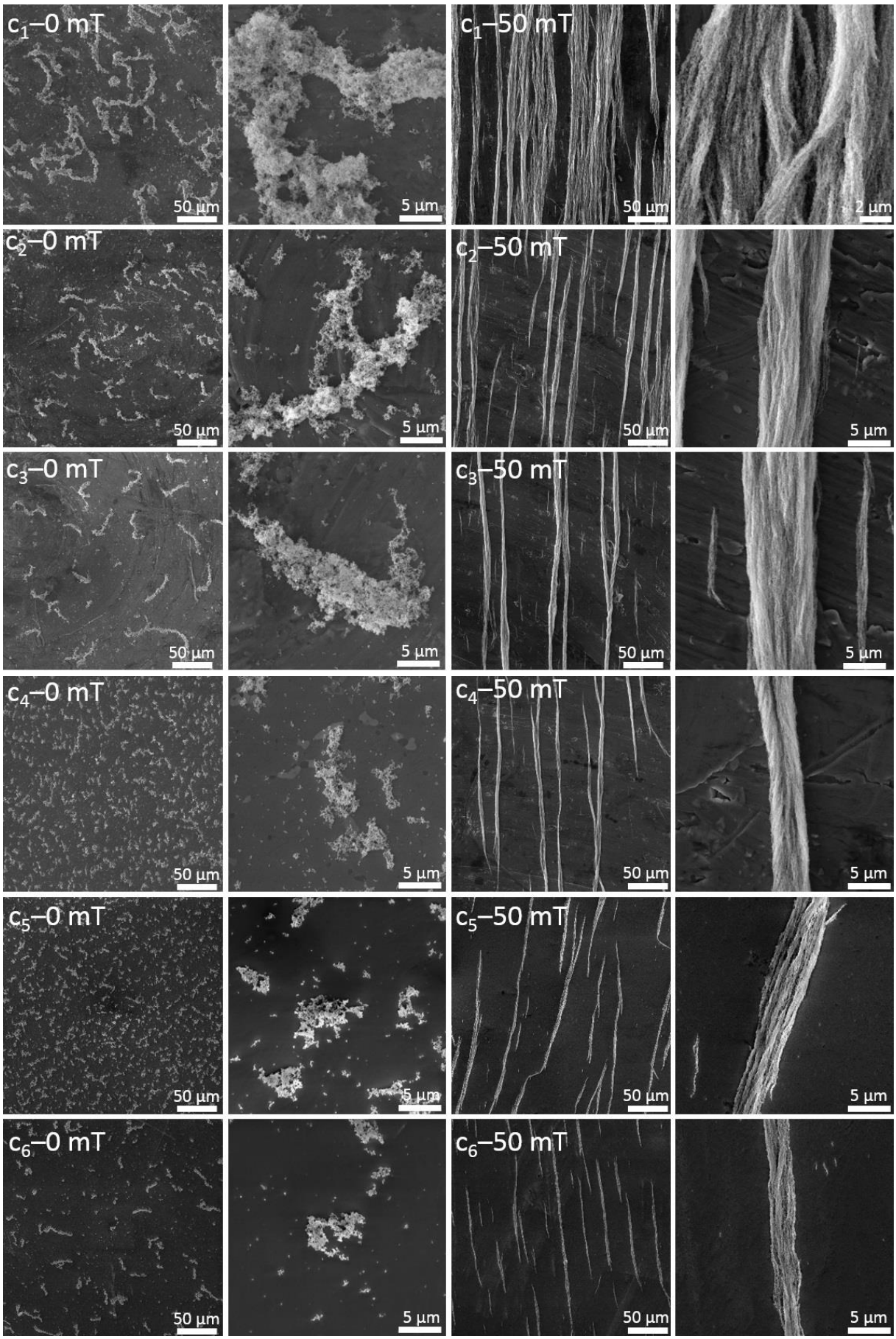

Figure 33 Electron micrographs of magnetically directed self-assembled structures assembled from acetone in the magnetic field with induction *B*=0 mT and *B*=50 mT. Particle concentration is given in Table 3. Magnification 1k and 10k x in SE mode is provided for each sample.

3.1.4 Polyurethane samples

Polyurethane samples filled with a low particle content ϕ=0.1 vol. % show formation of small micrometre aggregates which grow into thin particle chains with a similar diameter when magnetic field B=50 mT is applied. These thin and high aspect ratio magnetic chains are homogenously oriented in the direction of applied magnetic field. Increase of particle content led to more extensive aggregation of particles into microsized particle flocculates homogenously distributed in the volume of sample. High-magnification particle structure of self-assembled aggregate is shown in Figure 34C. Assembling time for polyurethane samples is given by gel-point which is reached in 300 seconds. In combination with an applied external magnetic field, particle structures grow from isotropic aggregates into oriented magnetic superstructures (Figure 34D). The crucial role of building block size on the size of resulted magnetic assemblies is perfectly visible when low and high particle concentration is compared. However, only equilibrium-close structure after ta=300 sec can be seen, but in the case of lower concentration, much smaller particle aggregates are expected due to lower interparticle distance than in sample with10x larger concentration.

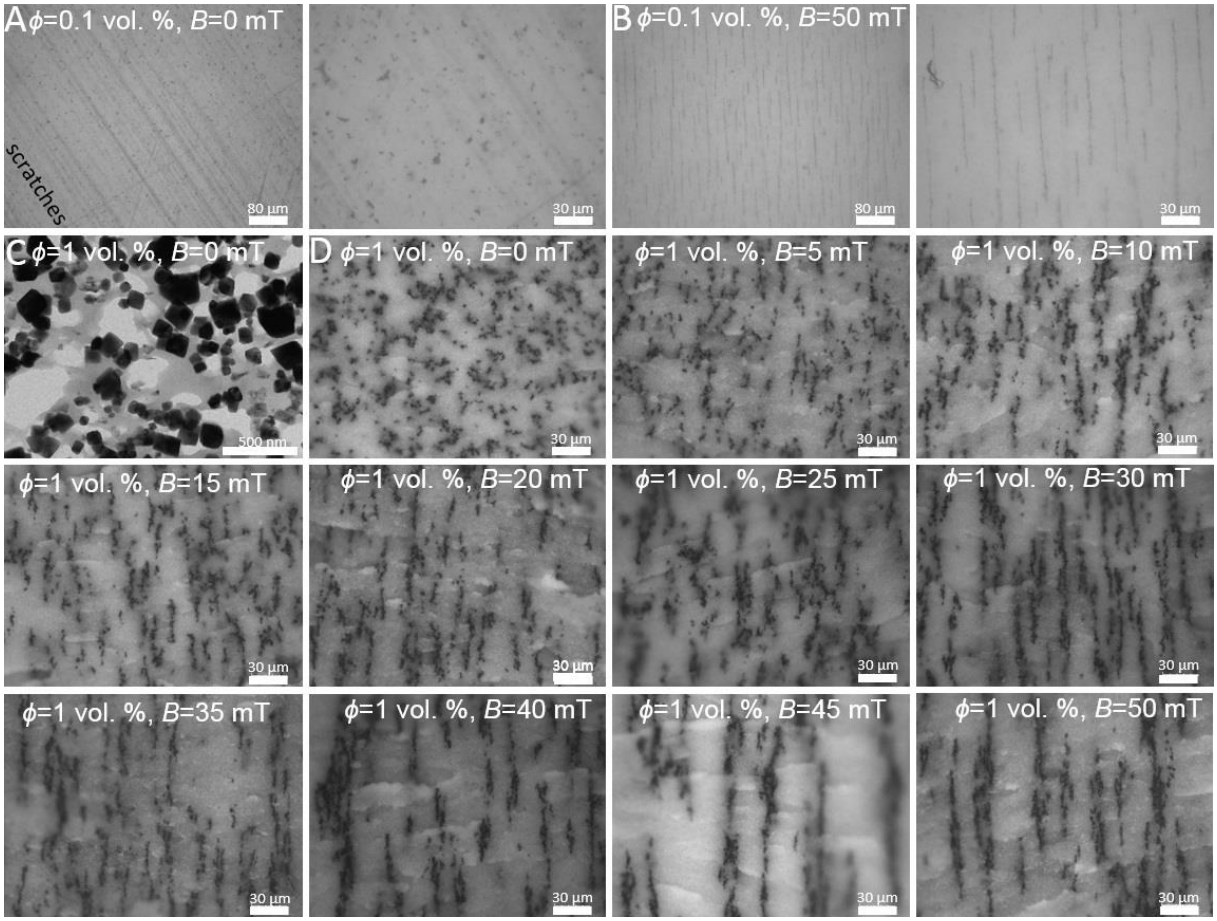

Figure 34 Structure of polyurethane NPC with ϕ=0.1 vol. % of magnetite (d=100 nm) under application of (A) no magnetic field and (B) B=50 mT. (C) Nanostructure of self-assembled polyurethane PNC from TEM. (D) Structure of polyurethane NPC with ϕ=1 vol. % of magnetite (d=100 nm) under application gradually increasing magnetic field B=0-50 mT. Assembling time is t_a=300 sec.

3.2 Thermo-mechanical properties

The mechanical anisotropy of magnetically assembled nanoparticle systems was studied by various authors (*137, 139, 143, 144, 262-265, 281*). Enhancement of mechanical properties in direction of particle assemblies is the most often result reported in the humble literature. All the investigated systems have one thing in common – the influence of the particle assemblies on the mechanical properties has been studied in proximity or far above T_g of system. It is generally known that large enhancement of polymer nanocomposite stiffness is obtained mainly above T_g where polymer chains undergo relaxation processes hindered by the presence of NPs (*204, 205, 207, 282*). In this temperature range, deformation of the particle structure and/or polymer immobilization are two common theories explaining the increase of the modulus. Despite research done in this field, reinforcing mechanisms of anisotropic chain-like particle structures are not fully understood yet. In this chapter, thermo-mechanical measurement of complete temperature spectrum (from glassy through transition to rubbery region) of material stiffness is discussed.

Dynamic mechanical analysis with a temperature ramp from T=170 °C to -100 °C was used for the mechanical characterisation of prepared PNCs. Thin polymeric films were used as specimens. History of material was erased at high temperature and then thermo-mechanical response was measured during cooling of the material. Orientation of structures within the films with a respect to the loading direction is schematically illustrated in Figure 35A. Samples exhibit thermal stability at high temperatures during repeated measurement showing identic course of moduli (courses of moduli fit the previous measurements). It can be assumed that no additional thermal post curing, network degradation or other processes are present in studied temperature range, or at least no significant changes in molecular weight of polymer and network density influencing the visco-elastic properties.

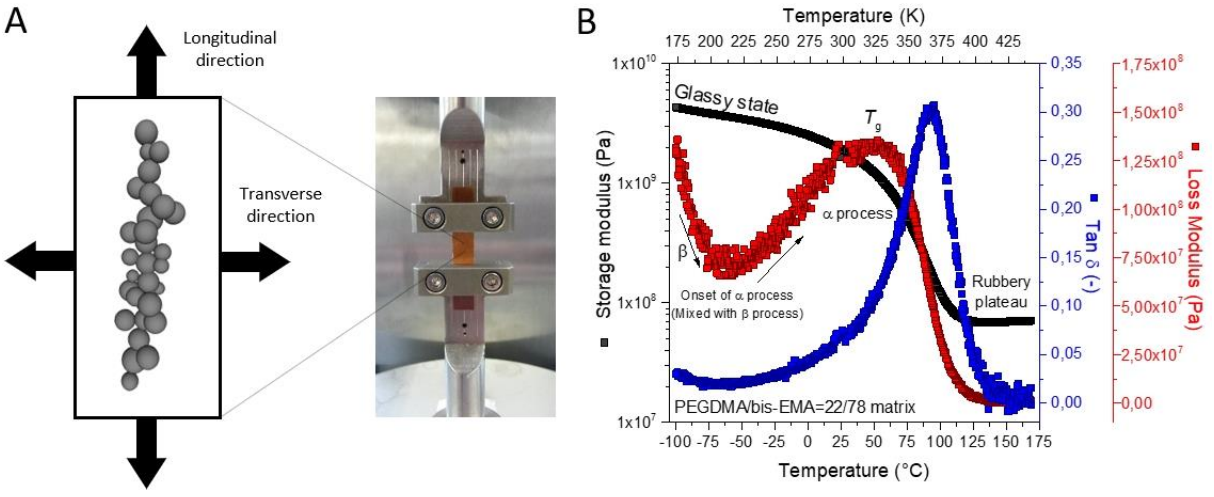

Figure 35 (A) Schematic illustration of the structure orientation in the plastic films with a respect to the loading direction (Longitudinal vs. Transverse direction) and digital snapshot of specimen clamped in tension geometry. (B) Representative DMA temperature spectrum for polymer matrix.

3.2.1 Glass transition

In the glassy state, the motion of the polymer chains is 'frozen' and slow in such extend that mechanical testing at common frequency ranges (f=10^{-3}–10^{2}) is not able to detect molecular relaxations of the polymer backbone – α process (T_g). As a temperature increases, thermal motion and relaxations of polymer chains start to be more significant and fast enough to be detected in the frequency range of experiment (here, f=1 Hz). This will result in the decrease of the macroscopic mechanical properties of the material (such as Young's modulus or complex modulus measured by DMA) because polymer chains become 'softer' and more prone to the deformation due to released mobility of chains. This results in the increase of viscous behaviour of material and increase of loss modulus (E'') which directly reflects viscous behavior of the material – consumption of the input energy for the dissipation processes – such as relaxation processes of the polymer chains. This will result in the phase shift (δ) between applied (oscillation) deformation and measured stress response – viscoelastic behavior. Glass transition (T_g) of the matrix and composites was determined from the peak of the loss modulus which was fitted using GCAS peak function in Origin.

Also, differential scanning calorimetry (DSC) was used to determine the thermal transitions in the composites (glass transition and melting/crystallization). Heating/cooling rate 5 °C/min from T=170 to -80 °C was used to simulate the conditions during the DMA experiment. Anyway, release of chain mobility occurs in very broad temperature range spanning across 100 °C (see Loss modulus in Figure 35B) due to broad distribution of molecular weights between network crosslinks and free (unpolymerized) chain ends which are common for the photocured polymers. Glass transition of shorter and freely hanging chains occurs at lower temperatures while domains with a higher cross-link density require more energy and undergo the relaxation at higher temperatures. It was complicated to quantitatively asses the glass transition only by the tiny changes of heat capacity which changes negligibly and gradually in the broad temperature range and no 'sharp' transition is observed regardless of heating/cooling rate. Much stronger effects of the released chain mobility were observed on the mechanical response such as decrease of storage modulus or peak on loss modulus. Hence, DMA was used for determination of T_g. In contrary to complications with a negligible glass transition, one important information was obtained from the DSC scans – no melting/crystallization enthalpy was measured and polymer matrix is considered as amorphous even in nanocomposites, despite PEG polymers often may show semicrystalline morphology (*283*).

Glass transition of neat polymer matrix (PEGMA/bis-EMA=22/78) was evaluated as T_g=45.1±3.9 °C. Its position shifts to lower temperatures and decreases by more than ΔT_g>-5 °C with an addition of 1 vol. % of magnetic nanoparticles which are aggregated into complex sub-micro structures (Figure 36B). This decrease is caused by the absorption of the light during the photocuring by magnetite nanoparticles and especially by their larger aggregates/structures (*154, 270*). Particle structures work as efficient light absorbers/scattering objects for the light despite their diameter is bellow critical dimension which equals to wave length absorbed by the

photoinitiator (λ=370-400 nm)(*268*). For larger structures than this length, penetration of light is almost impossible – for example the penetration in longitudinal direction of the structures (sub-micro to micro length). Light required for initiation and cleavage of photoinitiator thus may not penetrate properly the depth of the sample which is even pronounced for growing structures in magnetic field. With an increase of interchain distance occurring at B=25 and 50 mT, light penetrates trough the magnetite free domains – optical paths of neat matrix and T_g starts to upturn (*154*). In addition, light has limited possibility to penetrate inner structure of particle assemblies and cross-link the monomers entrapped here. Later, it will be shown that this polymer fraction is essential for thermo-mechanical properties of PNCs. Measured vitrification course from loss modulus is affected by both polymer fractions – polymer matrix around the structures and matrix entrapped inside the structures. Thermal post curing generates additional initiating radicals and repeatably trigger the cross-linking radical polymerization, however mobility of free radicals is slower and limited by the diffusivity of free radicals trough the polymer network although temperature is far above T_g.

The presence of the immobilised layer of polymer on the NPs is assessed by various analytical methods (*212*) but the most commonly, the increase of T_g of composite is the most straight forward evidence of altered relaxations. Due to decrease of cross-linking density with an addition of MNPs and their structuring by magnetic interactions, T_g of PNCs is gradually decreasing (*284*), hence the presence of polymer chains with retarded dynamics cannot be qualitatively and directly evidenced by analysis of T_g. On the other hand, this does not mean that polymer chains are not immobilised/confined by particle surface. The polymer network in the presence of MNPs just has a smaller cross-linking density than the unfilled matrix. Repulsive NP-polymer interaction is not expected.

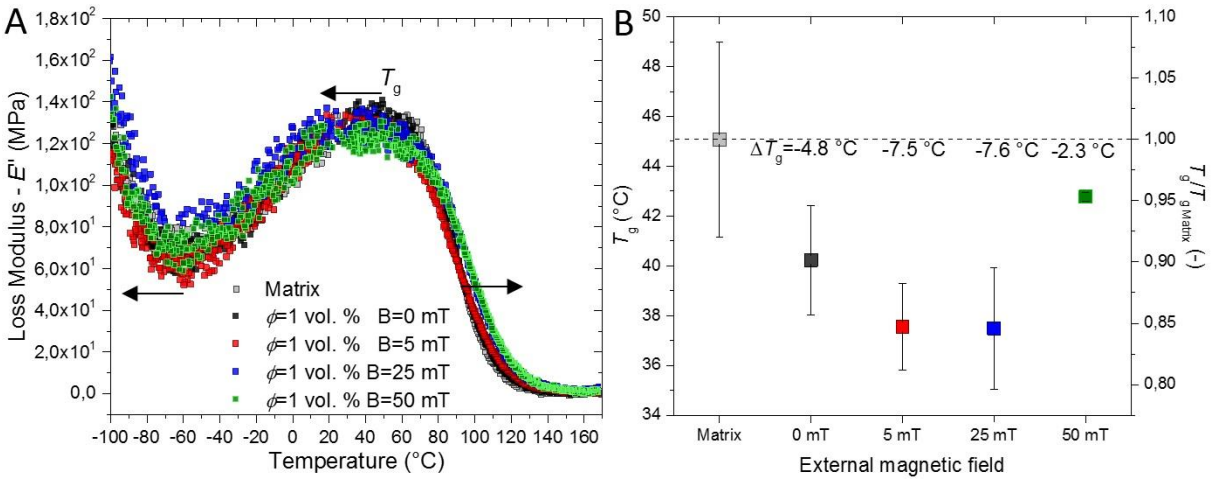

Figure 36 (A) Loss modulus for the matrix and nanocomposites containing ϕ=1 vol. % of self- and magnetically-assembled Fe_3O_4 magnetic nanoparticles. (B) Evaluated T_g of the polymer matrix and its nanocomposites as a function of the external magnetic field.

3.2.2 Mechanical properties in glassy region

The complete temperatures spectrum (from -100 °C to 170 °C) of the storage moduli of the magnetic PNCs is shown in Figure 37A,B for both longitudinal and transverse direction, respectively. Insignificant effect of the particles and their assemblies on the mechanical response is observed bellow glass transition of the system while substantial difference in modulus is observed above glass transition. Storage modulus is normalized to modulus of neat polymer matrix for both regions – glassy and rubbery and shown in graph in Figure 37C.

Mechanical properties of composites in glassy region scatter around boundary E/E_M=1 regardless of structure size or its orientation (Figure 37C). Negligible effect of NPs on the stiffness of PNCs in the glassy region is commonly known for decades and mentioned in more detail in the Chapter 1.5.2 Thermo-mechanical properties. In this region, mechanical response of PNCs obeys a micro-mechanical reinforcement given by the volume replacement mechanism – replacement of polymer with a stiffer phase (particles). This model accounts with a contribution of particle deformation to overall macroscopic deformation of PNC. And thus, it might be said that addition of fraction of 1 vol. % will have only marginal effect on the mechanical robustness of PNCs. Usually, higher volume fractions (or substantial modification of polymer matrix via particle-polymer interactions) are required to induce reinforcement of the glassy matrix. Experimental data of the storage modulus were fitted with a micro-mechanical Kerner-Nielsen-Lewis model which is commonly utilized for the particle filled polymers filled either with MPs or NPs and it is derived in Equation (10) (*285*).

$$\frac{E_{\mathrm{KNL}}}{E_{\mathrm{M}}} = \frac{1+A\cdot B\cdot \phi}{1-\psi\cdot B\cdot \phi} \qquad \text{Equation (10)}$$

Where E_{KNL} and E_{M} are the tensile moduli of the composite and neat matrix, respectively. Parameter A is a function of matrix's Poisson ratio given by Equation (11), and parameter B is a function of reinforcing effect and parameter A given by Equation (12). Where E_{F} is the tensile modulus of magnetite (value E_{magneite}=175 GPa was used (*286*)). Parameter ψ is a function of particle volume fraction ϕ and maximum volume fraction ϕ_{max}=0.64 given by Equation (13).

$$A = \frac{7-5\nu_M}{8-10\nu_M} \qquad \text{Equation (11)}$$

$$B = \frac{\frac{E_F}{E_M}-1}{\frac{E_F}{E_M}+A} \qquad \text{Equation (12)}$$

$$\psi = 1 + \phi^2\left(\frac{1-\phi_{\mathrm{max}}}{\phi_{\mathrm{max}}}\right) \qquad \text{Equation (13)}$$

Despite Kerner-Nielsen-Lewis model does not account with a NP-polymer molecular interaction and resultant modification of polymer matrix (*206*), this model predicts a stiffness of PNCs filled with ϕ=1 vol. % of MNPs as E_{KNL}=3.5 GPa which corresponds to normalized value $E_{\mathrm{KNL}}/E_{\mathrm{M}}$=1.021 (Figure 37C – blue dotted line). Data of glassy state modulus scatter around this trend line what means that reinforcing mechanisms can be explained by the volume replacement of softer polymer glass with much stiffer magnetic nanoparticles.

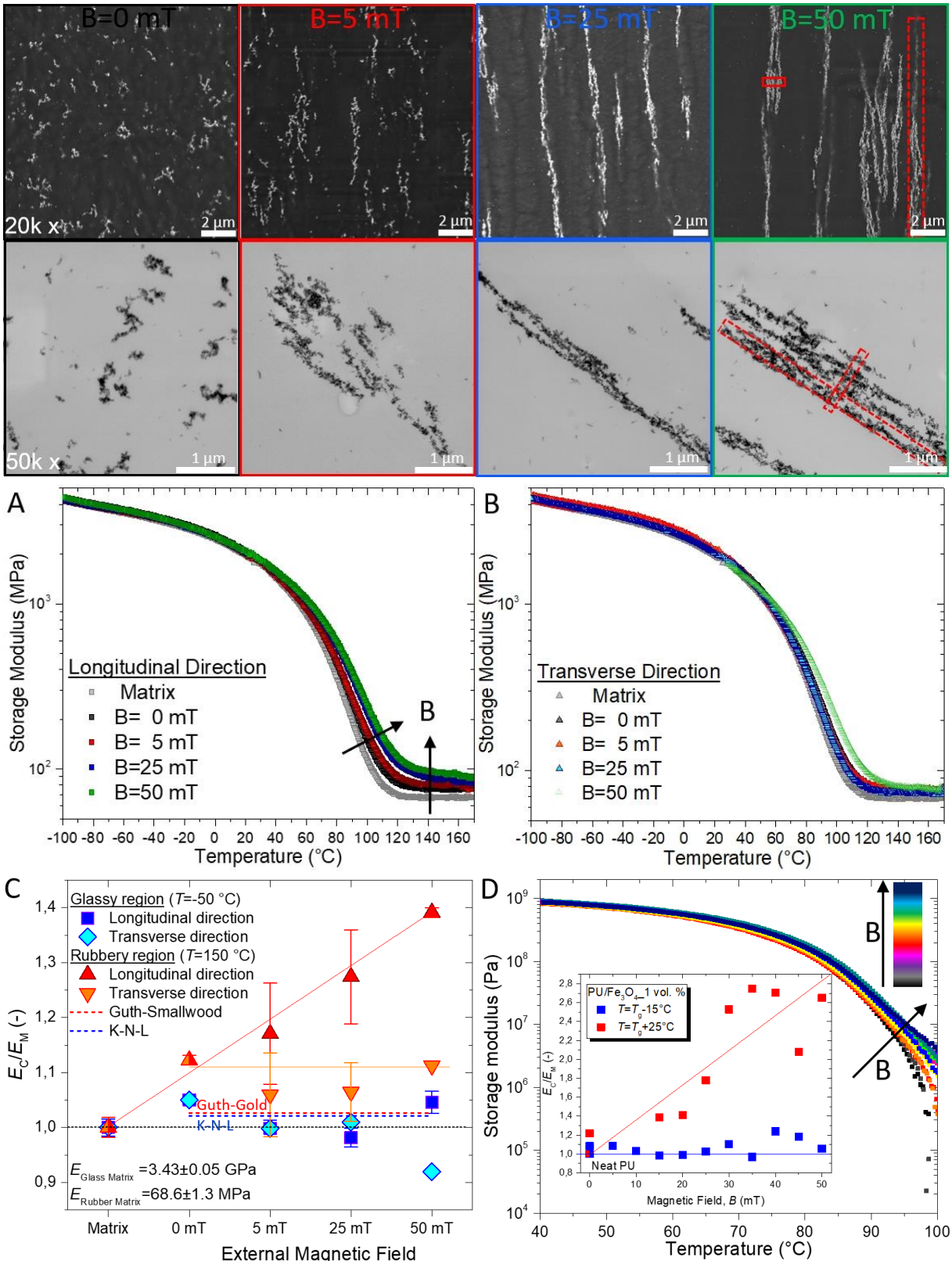

Figure 37 DMA temperature ramp spectrum for photopolymer matrix and its nanocomposites filled with ϕ=1 vol. % of Fe_3O_4 and assembled under magnetic fields B=0, 5, 25, 50 mT after t_a=10 sec. Storage modulus of PNCs films in (A) longitudinal and (B) transverse direction with a respect to the structure orientation as a function of temperature. Color frames around images of structure above corresponds to color labeling in A and B. (C) Storage modulus of composites normalized to modulus of neat matrix (E_C/E_M) as a function of the external magnetic field. (D) Storage modulus of PU/Fe_3O_4 composites as a function of temperature with inset showing normalized values as function of magnetic field bellow and above T_g.

3.2.3 Mechanical properties in rubbery region

Rubbery modulus of neat matrix drops down by two orders of magnitude from glassy state with a stiffness E_M^G=3.43GPa to E_M^0=68.6 in rubbery plateau. In contrary to glassy region, large enhancement of composite stiffness and strong anisotropy was measured for the mechanical properties of PNCs far above their T_g. Relative values of the composite stiffness normalized to neat polymer modulus are plotted in Figure 37C. Difference between mechanical properties of polymer matrix and its PNCs starts to appear in proximity of the T_g of the polymer matrix. Course of storage modulus as well of tan δ starts to separate around T=20 °C and their different course becomes significant with an increasing temperature as soon as T_g is exceeded. Figure 38 shows representative difference between longitudinally and transversely oriented structures assembled in magnetic field B=25 mT after 10 seconds, both storage modulus and tan δ are shown. Similar trends were observed also for B=5 and 50 mT samples. For transversely oriented structures, almost constant enhancement of the rubbery modulus was measured comparable with a modulus of the self-assembled composites (Figure 37B,C). As well, tan δ shows same position and height of tan δ peak. Much stronger effect of the particles structures on the increase of the rubbery modulus is observed for their longitudinal orientation (Figure 37A,C) and modulus increases steadily with an increasing assembling field (with a growth of the particle structures in the sample). Also, similar effect of the particle structures on the mechanical properties of PNCs bellow and above its T_g is observed for polyurethane set of samples. Figure 37D shows courses of storage moduli for the polyurethane PNCs while inset in the figure shows a plot of relative composite modulus as a function of magnetic field applied for assembling. Corresponding structures of polyurethane PNCs can be seen in Figure 34.

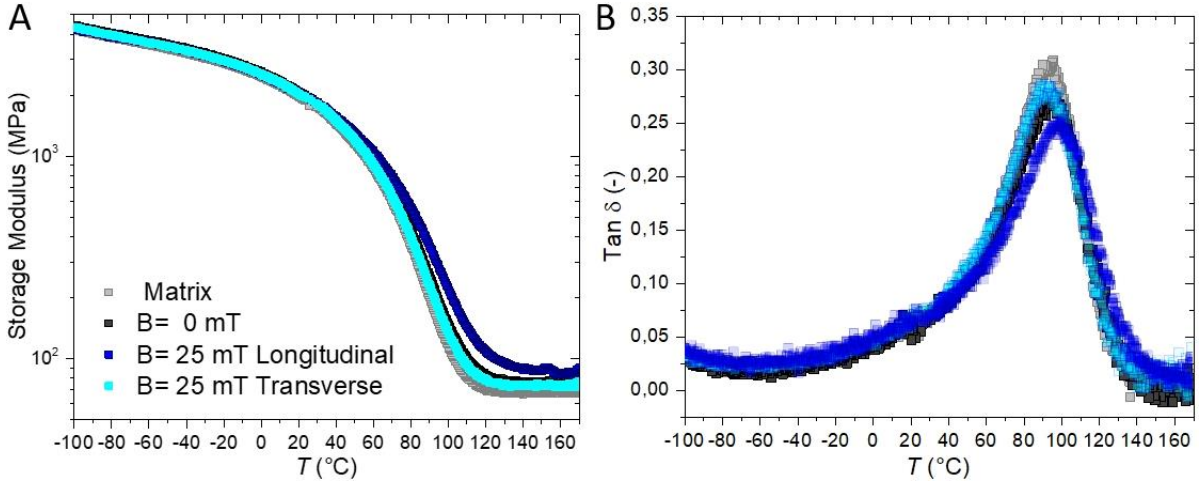

Figure 38 Course of (A) storage modulus and (B) tan δ for polymer nanocomposites containing ϕ=1 vol. % of magnetite nanoparticles self-assembled (0 mT) and magnetically assembled in external magnetic field 25 mT after 10 seconds. Comparison between longitudinal and transverse direction is shown. Inset in (A) shows whole temperature range.

It seems that volume replacement and stress transfer mechanisms put a condition on the reasonable moduli mismatches between polymer matrix and filler phase. If we would use Kerner-Nielsen-Lewis model for a prediction of composite modulus in rubbery region and thus

picture of volume replacement, we would end up with a stiffness of the rubbery composite, E_C=7.01 MPa which is E_C/E_M=1.02 in relative units. However, experimental data of relative stiffness of PNCs in rubbery state exhibit much higher values than 1.02 (Figure 37C). Stiff inclusions are not able to deform in soft polymer (or deform negligibly) due to large mismatch between particle and polymer moduli, therefore stress is concentrated in surrounding matrix which is strained more in presence of the particles – hydrodynamic entropic effect of strain amplification (*287, 288*).

For the entropic strain amplification contribution to the stiffness of PNCs, Guth-Gold model (*289, 290*) is used (Equation 14). This model is derived from Einstein's viscosity formula for filled liquids and it is based on the inability of particles undergo the deformation process of their atomistic structure due to large mismatch of matrix/particle moduli and only surrounding matrix is being strained (locally overstained). However, it was outlined that stress concentration may be in contrary with a strength increase which is often observed for filled elastomers/rubbers (*242*). Usage of this model and its modifications for various systems including those with an immobilized polymer layer was debated by various authors (*291, 292*). Despite numerous discussions and discrepancies in outlined theories and experiments, this model is used for predictions of PNC's stiffness above T_g and in rubbery state (*206, 288*). In the photopolymer syste, this model predicts a normalized rubbery modulus of nanocomposite as E^0_{GG}/E^0_M=1.026 (Figure 37C – red dotted line). Experimental data for both, longitudinal and transverse orientation in rubbery state show considerably higher values than a model prediction. Discrepancies between model and real experimental results are the most commonly debated on the background of the immobilized layer (*206*) or contribution form particle structure (*288*) concepts. The both theories seem to have their own logic and their mutual existence might be also explanation despite hardy to distinguish their individual contributions.

$$\frac{E^0_{GG}}{E^0_M} = 1 + 2.5\phi + 14.1\phi^2 \qquad \text{Equation (14)}$$

Importantly, sample with the highest crosslink density (υ_c) is expected to have the highest temperature of glass transition and the highest rubbery modulus – which is pure matrix. The network density is characterized as a number of cross-linking points (or junctions) per volume and it is function of mean molecular weight of polymer chains between two physical/chemical junctions – M_c. This parameter of course influences a mechanical response of polymer and its composites, especially modulus in rubbery plateau, E^0_M which is especially sensitive to network/cross-link density according to Equation (15) (*293, 294*).

$$E^0_M = \rho_R \frac{R \cdot T}{M_c} = \frac{\rho_R}{\rho_G} \cdot \frac{R \cdot T}{N_A} \upsilon_c \qquad \text{Equation (15)}$$

Where $\rho_R \approx 1000$ kg·m^{-3} and $\rho_G \approx 1200$ kg·m^{-3} are densities of matrix in rubber and glass, respectively, N_A=6.022·10^{23} mol^{-1} is Avogadro constant, R=8.314 J·mol^{-1}·K^{-1} is universal gas constant, T=423 K is absolute temperature at rubbery plateau (tan δ minimum) and M_c and υ_c are molecular weight between cross-links and cross-linking density, respectively.

Glass transition was found to be in linear dependence with υ_c (*293*). Thus, pure matrix which has the highest value of glass transition, logically, should have largest modulus of rubbery plateau. In other words, if υ_c of polymer matrix decreases, rubbery modulus of polymer matrix in nanocomposite needs to decrease as well and stiffness of the PNCs is expected to follow the trend of their glass transitions. But relative rubbery modulus of PNCs is steadily increasing with a magnetic field applied for the assembling beyond the limit set by Guth-Gold model despite T_g decrease (Figure 37C). Composite stiffness as a function of T_g is plotted in Figure 39A. This supports that increase of storage modulus above T_g cannot be caused by higher cross-linking density of the polymer matrix in PNCs. In fact, two processes with an adverse influence on the PNC's stiffness are present: *i*) decrease of the photopolymerization yield and *ii*) stiffening by the particle structures. It is worth to notice that despite relatively large standard deviation for T_g of neat matrix (T_g=45.1±3.9 °C), rubbery modulus for matrix differ only negligibly resulting in small standard deviation (E^0_M=68.6±1.3 MPa). The decreasing polymerization yield in the presence of NPs and enhancement of composite's stiffness was observed for example by Sotta, et al. (*288*). Cross-linking initiator is preferentially adsorbed on the silica surface rather to be dispersed in SBR matrix. They used normalization of relative value of composite stiffness (E_C/E_M) by the parameter linearly proportional to the cross-linking density measured by NMR. Similar approach of modulus normalization is adopted here, and $T_{g\,PNC}/T_{g\,Matrix}$ ratio is used for the normalization of the relative rubbery modulus (Equation (16)). This will consequently decrease the value of matrix's modulus, E_M in composite systems. Resulted reinforcing ratio for the nanocomposites, R is plotted as a function of the assembling magnetic field in Figure 39B.

$$R = \frac{E_C}{E_M} \Big/ \frac{T_{g\,PNC}}{T_{g\,Matrix}} = \frac{E_C}{E_M \cdot \frac{T_{g\,PNC}}{T_{g\,Matrix}}} \qquad \text{Equation (16)}$$

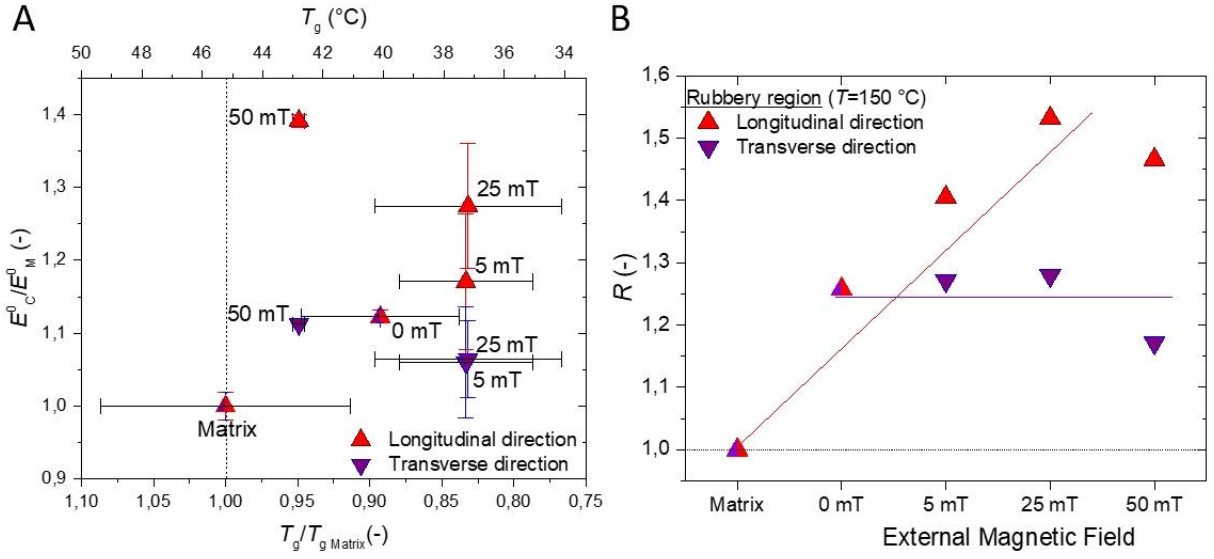

Figure 39 (A) Rubbery modulus of nanocomposites as a function of glass transition ratio – substitution for relative cross-linking density. (B) Normalized reinforcing ratio for the structures assembled in various magnetic fields. Lines in plot are only for eye guidance.

3.2.4 Mechanical properties in transition region

In addition to storage modulus, some interesting features were observed also for tan δ during vitrification in temperature range between the rubbery plateau and peak of loss modulus (Figure 40A,B). This broad temperature range will be marked as transition region. These features are vanishing slightly bellow T_g, around T=20 °C. Tan δ is ratio between loss modulus representing a viscous behaviour and storage modulus which represents elastic behaviour of material – tan δ=E''/E'. As a value of tan δ decreases, sample is more elastic, and consequently less energy is dissipated. This means that from the comparison of tan δ absolute values of individual nanocomposite systems, one can distinguish which structure is more elastic and thus which sample shows more reinforcing effects. Tan δ for longitudinally oriented structures shows shift of tan δ peak in both directions – shift in *x*-axis to higher temperatures and shift in *y*-axis by decrease of tan δ absolute values with an increasing magnetic field and length of structures (Figure 40A,C,D). For transversely oriented structures, both values remain more or less on the same values as self-assembled structure (Figure 40B-D). Thus, orientation of particle structure

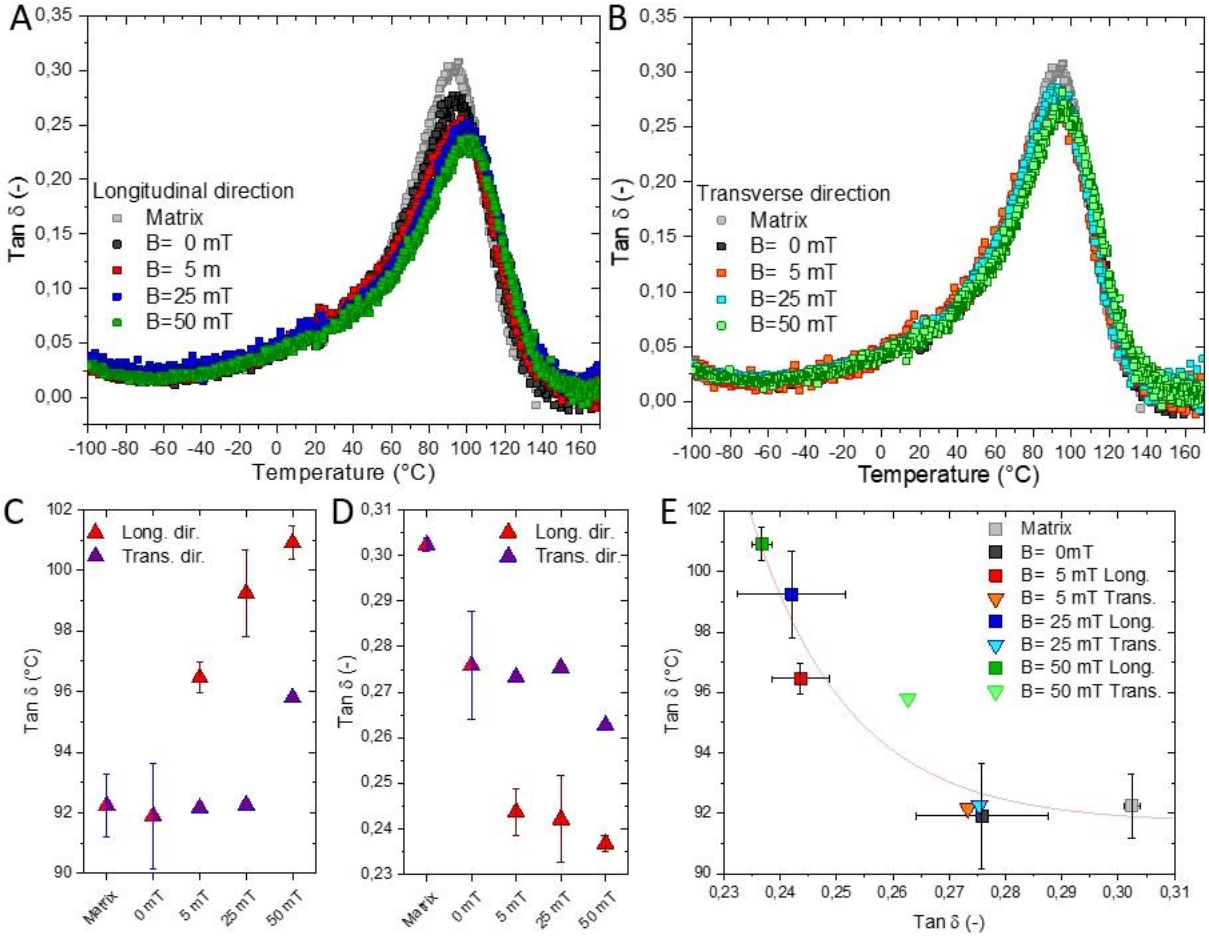

Figure 40 Tan δ from DMA temperature ramps for PNCs filled with ϕ=1 vol. % of Fe_3O_4 and assembled in magnetic fields B=0, 5, 25, 50 mT. Tan δ in (A) longitudinal and (B) transverse direction as a function of temperature. (C) Tan δ peak temperature position, (D) maximum value of tan δ as a function of external magnetic field. (E) Tan δ peak position vs. tan δ peak absolute value for PNCs.

needs to have an influence on the viscoelastic behaviour of the soft polymer matrix above T_g. There is no difference for tan δ of PNCs bellow glass transition (around T≈20 °C) or in rubbery plateau (above ~150 °C). In rubbery state, tan δ≈0.

Bulk polymer chains are considered as completely unvitrified – in rubbery/liquid state when exceeding temperatures of rubbery plateau (~150 °C). Tan δ falls to its minimum and polymer matrix is considered as ideally rubbery elastic material. Here, only reptation and very fast reconfigurations of polymer segments occur. Time-temperature superposition, temperature and frequency dependence of polymer stiffness should be kept in mind. During cooling – vitrification, segmental relaxations of polymer start to require longer times/higher energies and stiffness of polymer network gradually increases. Segments which are part of the dense polymer network and/or strongly adsorbed/confined by particles require largest portion of the energy and their relaxation time is longest (see the inset in Figure 42B). Consequently, they vitrify as first when temperature is decreased while other segments (in bulk) have a still enough time to undergo relaxation (*295*). The stiffness of vitrified segment is increased.

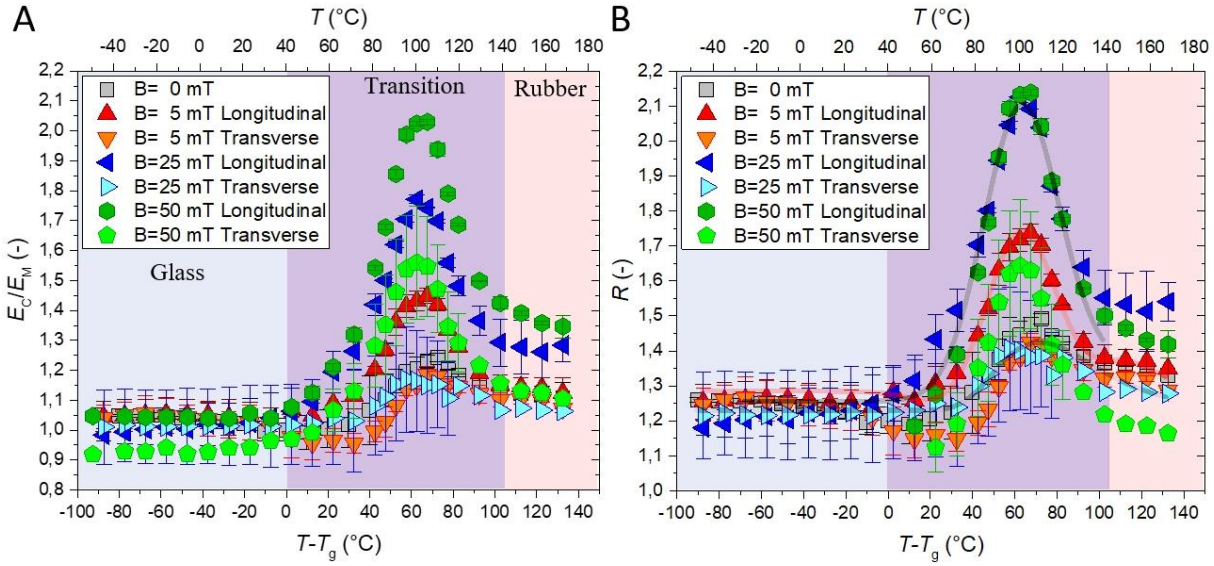

Figure 41 (A) Relative composite modulus (E_C/E_M) and (B) normalized reinforcing ratio for PNCs containing ϕ=1 vol. % of MNPS as a function of distance from T_g (T-T_g). Individual temperature/relaxation time regions are marked as follows: glass – blue, transition – purple and rubber – red.

Relative values of PNC's modulus were plotted as a function of distance from the PNC's T_g (Figure 41) to address the influence of the particle assemblies on the stiffness of PNCs in whole temperature range – glassy, transition and rubbery region. The effects in glassy and rubbery regions were already discussed in previous sections. Note that T_g of individual composites (Figure 36) were used for the calculation of temperature distance (T-T_g). Figure 41 shows plot of (A) E_C/E_M and (B) reinforcing ratio, R versus T-T_g. Large peak of relative composite stiffness can be observed in transition region exhibiting temperature dependent and viscoelastic reinforcement. Maximum is temperature independent for all samples regardless of structure size of its orientation. Note that self-assembled and magnetically assembled structures (B=0, 5, 25

mT) with a transverse orientation shows almost identical course of reinforcing effectivity. Transversely oriented sample assembled under B=50 mT deviates and possible reasons could be caused by deformation of the large laterally merged magnetic superstructures (see 50 mT sample in Figure 37). What is the most important, longitudinally oriented samples significantly differ from self-assembled and transversely oriented PNCs also and mainly in transition region with an evident maximum.

Surprisingly, despite reduction of composite's T_g, storage modulus of longitudinally oriented nanocomposites shows much steeper increase during vitrification from rubbery state (Figure 37A, Figure 38A). The temperature vitrification should be direction independent, however appearance of PNCs storage moduli exhibits significant elastic anisotropy. This invokes question: *What causes this discrepancy between fragilities of anisotropic structures and the neat matrix and/or their self-assembled quasi-isotropic counterparts?*

3.2.5 Reinforcing mechanism

Additional concepts and theories explaining the mechanical response of PNCs can be found in the literature dealing for example with Payne effect (*219, 233, 296-299*). This effect was ascribed to breakdown and/or reconfiguration of all possible structural features in PNCs (*287*) and up to now, mechanisms behind are "*far from being clear*" (*295*). Despite discrepancies in the field of PNCs, author's own theory of reinforcing mechanisms for anisotropic particle structures (assembled by the guidance of the external magnetic field) will be addressed on the background of own experimental results and knowledge from the literature. This theory can be in general applied for reinforcing mechanisms in PNCs.

The modification of PNCs mechanical response is often attributed to adsorption of polymer chains on the surface of solid inclusions leading to creation of bound layer with altered relaxations (*300, 301*). The thickness of bound layer is usually reported in the order of several nanometres (1-2 nm) depending on various chain properties and interactional strength (*10, 12, 13, 220, 300*). For example, Xu, et al. (*295*) studied the adsorption of low molecular weight polypropylene glycol (PPG) on the silica NPs structured in continuous network and its contribution to viscoelastic and thermal response of PNCs. Anderson, Kim and Zukoski (*302, 303*) reported an adsorption of polyethylene glycol (PEG) with various molecular weights on the surface of silica NPs. Both teams reported bound polymer layer with a thickness in order of several nanometres for studied glycol molecules. Also, methacrylate esters are frequently reported to be successfully anchoring moiety in the presence of NPs (*205-208, 304*).

Surface of crystalline MNPs is also covered by hydroxyl groups and thus certain level of similarity can be shared with commonly studied amorphous silica filled PNCs. Both, PEG and ester groups can be found in the backbone of PEGDMA and bis-EMA molecules and polymer chains are expected to interact with a surface of MNPs in analogic attractive manner. Both monomers contain multiple reaction sites. The first one is ester group (*304*) bridging methyl methacrylate with PEG unit and each monomer molecule contains two ester groups at the ends of the molecule backbone. The second interaction site is situated on the oxygen in the backbone of PEG (see Figure 20). These groups can act as Lewis acids coordinating their electron density with a hydrogen from surface HO– groups (Lewis base) and create hydrogen bonds. Bis-EMA monomer has a short PEG unit (n_{PEG}=1 and 2), on the other hand, PEGDMA monomer with n_{PEG}=16 can offer number of interaction sites. In addition, adsorption of initiator/initiating radicals on the surface of particles is not known.

If we will assume the existence of immobilised layer on the MNPs surface as well polymer chains bridging the contact between particles (however, could not be directly assessed by the analysis of the loss modulus and T_g), we will obtain hybrid polymer-Fe_3O_4 structures with a high inorganic content. It needs to be noted that usually higher particle volume fractions are required to increase the fraction of bound polymer relative to that bulk chains in such extent that it is possible to macroscopically distinguish the signal from immobilized chains. Here, we are dealing with a particle loading ϕ=1 vol. % and a complication in the form of decreased

photopolymerization yield. Despite this fact, changes induced by particle assemblies on mechanical properties are tremendous. Figure 42A shows an inner particle structure of the magnetic chain in sample B=25 mT from STEM observation. Nanoparticles are spaced with a thin layer of polymer. Interparticle surface-to-surface distance between closest neighbours was measured and trimodal distribution is plotted in Figure 42B. Mostly, particles are in direct contacts or distanced within the sub nanometer range. The radius of particles gives an opportunity for polymer occupation of this space. The second distribution peak is around 4 nm and third one around 14 nm. Both are large enough to accommodate the polymer coils or monomers. Other assembling fields exhibit quite similar particle packing and thus structures are something between aggregate and clusters while this nature depends on actual position within particle chain. Interparticle distances are considerable short in magnetically concentrated assemblies and behaviour of such system can find analogy with highly filled PNCs (*305-307*) or even analogy with a structure of platelets in nacre and/or mineralized collagen fibrils in bone (*257*). Polymerization degree of confined monomer units within the structures is not known. It will be assumed that monomers adsorbed on the particles and polymerized in confined space requires minimum space approximately 2Rg=2.4 nm to fit into the interparticle space without the change in chain conformation due to squeezing ($R_{g\ PEGDMA}$≈1.2 nm, approximated to $PEG_{Mw=1000}$ (*303*), gyration radius of bis-EMA is expected to be lower and more anisotropic). In the case of shorter distances (Δl<R_g), monomer coil cannot occupy this space without further reduction of gyration radius (*307*, *308*) or occupation of anisotropic shape (*309*) and consequently drastic modification of chain rigidity.

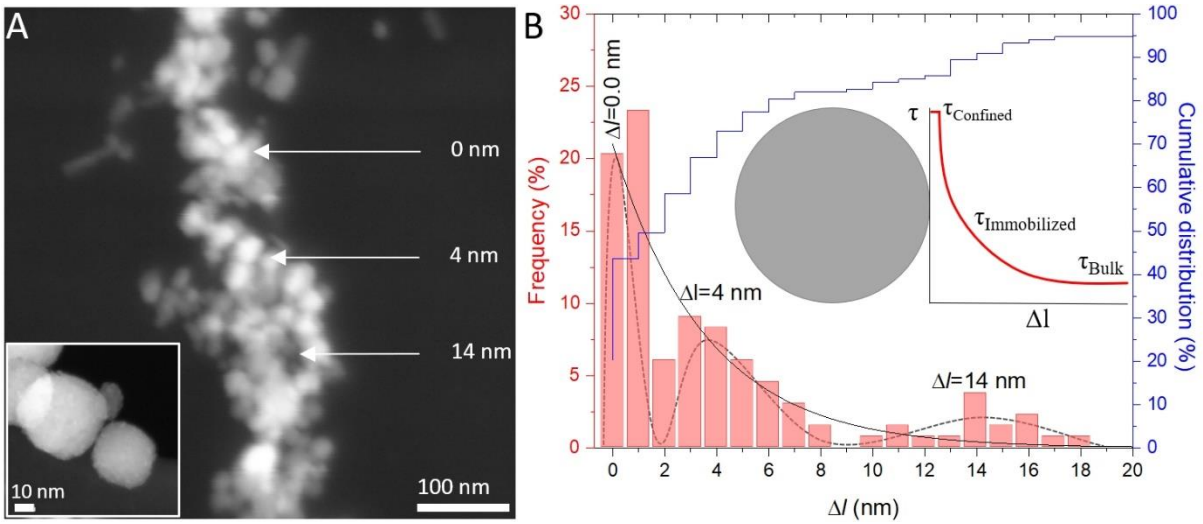

Figure 42 (A) STEM image of anisotropic structure assembled in B=25 mT after 10 seconds with ϕ=1 vol. % of particles in photopolymer matrix (dark areas is polymer). Arrows show typical places with a characteristic spacing. Dark field HR-TEM inset in (A) shows the most frequent situation when particles are in close contact resulting in Δl≈0 nm but their radius gives a rise to non-zero interparticle spacing suitable for polymer bridging. (B) Distribution of interparticle surface-to-surface distances Δl for the closest particle neighbors in the cluster from (A). Inset in (B) shows schematic depiction of relaxation time dependence on distance from particle surface.

Various researchers claimed that strongly bound and confined polymer chains may behave as glass even at the temperatures when the bulk polymer is already completely unvitrified. This effect results in the vast increase of reptation/relaxation times, rubbery plateau, or fully disappeared terminal zone commonly evidenced in rheological measurements of highly filled PNCs melts. For example, Mujtaba, et al. (*310*) measured the fraction of surface-immobilized polymer by NMR and detected significant fraction of segments with glassy relaxation times at temperatures of rubbery plateau of SBR/silica PNC. Fraction of glassy segments decreases with a temperature and it is dependent on particle volume fraction and level of confinement (caused by particle percolation). Similar NMR results were also published by Berriot, et a. (*232*) and Chen, et al. (*306*) also outlined that some segments might still appear as glassy in highly filled PNCs melts when interparticle distances are close or even lower than a length of Kuhn's segment. In these systems, unvitrified glass is preserved at particle loadings far above tens of volumetric percent.

Despite very low total fraction of MNPs in our systems, polymers shells are brought close enough to percolate due to magnetic interactions between particles or their assemblies during self- and magnetic assembly. Magnetic field increases local concentration of inorganic content considerably beyond the percolation threshold with a local particle volume fraction inside the particle chains calculated as ϕ_{local}~52 vol. %. This is close to maximum volume occupation for randomly packed spheres. Such short interparticle distances, vast enhancement of rubbery modulus and local particle volume fraction inside the magnetic chains indicate that there might be still a fraction of unvitrified polymer segments trapped inside the particle clusters. Term '*glassy*' will refer to polymer segments with retarded relaxations compared to bulk matrix, in our PNCs.

The percolation of glassy fraction of polymer and creating of continuous glassy backbone in soft matters (above T_g) is believed to be mainly responsible for the thermo-mechanical response of PNCs (*24, 207, 208, 219, 232-234, 296, 306, 310-312*). Also, Bharti, et al. (*67*) observed the stiffening effect of bridging chains in their magnetically assembled nanoparticles bound by fatty acids in water. Above transition temperature of fatty acid bridge, structures exhibit decreased rigidity. Mentioned experiments underline the undisputable contribution of relaxation times distribution within the volume of PNC on its thermo-mechanical response. Concept of percolated bridging glassy layer seems to be reasonable explanation for thermo-mechanical response of PNCs mainly due to its time-temperature dependence and viscoelastic appearance. Tauban, et al. (*234*) modelled the mechanical response of PNCs with confined polymer chains within the particle structures of various morphologies and packings based on previous experimental results and theories (*219, 232, 233, 296*). They present a plot of reinforcing ratio versus distance from T_g which exhibit very similar temperature dependence of reinforcing ratio for highly filled PNCs as plotted in Figure 41 for systems studied in this thesis. Such processing of thermo-mechanical data with a '*bell-like*' temperature dependence and maximum of reinforcing effectivity in transition region is universal for all PNCs. Therefore, distance of PNCs from its *T*g and rubbery plateau is important to be specified in scientific texts dealing

with a mechanical response of PNCs! Constant portion of storage modulus of PNCs at temperatures far above T_g is ascribed to deformation of bound glassy polymer with a significantly altered relaxation characteristic and stiffness high enough to avoid modulus drop.

Generally, particles assemblies in PNCs gradually form a nano, sub-micro, mirco and macroscopically percolated hybrid structures of various shapes and geometries with an increasing particle content. Consequently, nano, sub-micro, micro and macroscopic immobilized glassy polymer is formed in soft matrix (*207, 208*) and its shape and geometry are defined by particle arrangement. These hybrid structures can get under the deformation during the sample testing and exhibit non-zero stiffness. In our case, particles are organized in one-dimensional chains – fibers which may carry the load transferred from the matrix.

To address orientation dependent mechanism of reinforcement by hybrid anisotropic structures, continuum micromechanics concepts will be employed. Micromechanics in combination with a model of composite with various structural motives was used to describe the mechanical response of biological hard tissues (*313-315*). Complex reinforcing micro blocks commonly found in biological composites (*257*) were simplified by solid anisotropic microparticles arranged in polymer matrix in special geometrical patterns. Similar concept is used also here despite PNCs shows significant reinforcement only above T_g. Thus, such approximation and adopting of the micromechanical stress-transfer might not be relevant in whole temperature range, for studied PNCs. Hybrid micro chain structures of this work are approximated by solid fibres with a non-zero internal stiffness and homogeneous orientation. Depiction and description of model material with a multi-level hierarchy with images of individual levels of structure is in Figure 43.

During the deformation of the composite, particle fibres are stretched. The stress is transmitted via bridging polymer within the structures and amount of stress carried by anisotropic hybrid structures dependent mainly on their orientation, length and their internal stiffness (E_F). Higher stiffness of hybrid structure than a stiffness of surrounding medium is essential requirement for the composite reinforcement ($E_F > E_M$). In opposite situation, structures will decrease the stiffness of composite. In longitudinal direction, larger portion of stress is transferred from low stiffness matrix while transversely oriented structures are less reinforcing effective (*316*). Hence, transverse direction is comparable with self-assembled quasi-isotropic structures – similar volume of hybrid structures is locally under the deformation. This hypothesis is supported by the appearance of storage moduli for longitudinal and transverse direction showing significant anisotropy and change in their effect on reinforcement (Figure 37C, Figure 38, Figure 41). The reinforcing effectivity of structures seems to be linearly dependent on their aspect ratio (Figure 44A) and exhibits upturn above $L/D > 1$. Aspect ratio listed in Figure 27A is used for longitudinal direction and inreverse values for transverse direction. Note that thickness of magnetic structures is comparable with a thickness of self-assembled aggregates and radius of primary/secondary aggregates (~100 nm). Isotropic geometry $L/D = 1$ is added into the graph to address the deformation of the isotropic structures (marked as Transverse

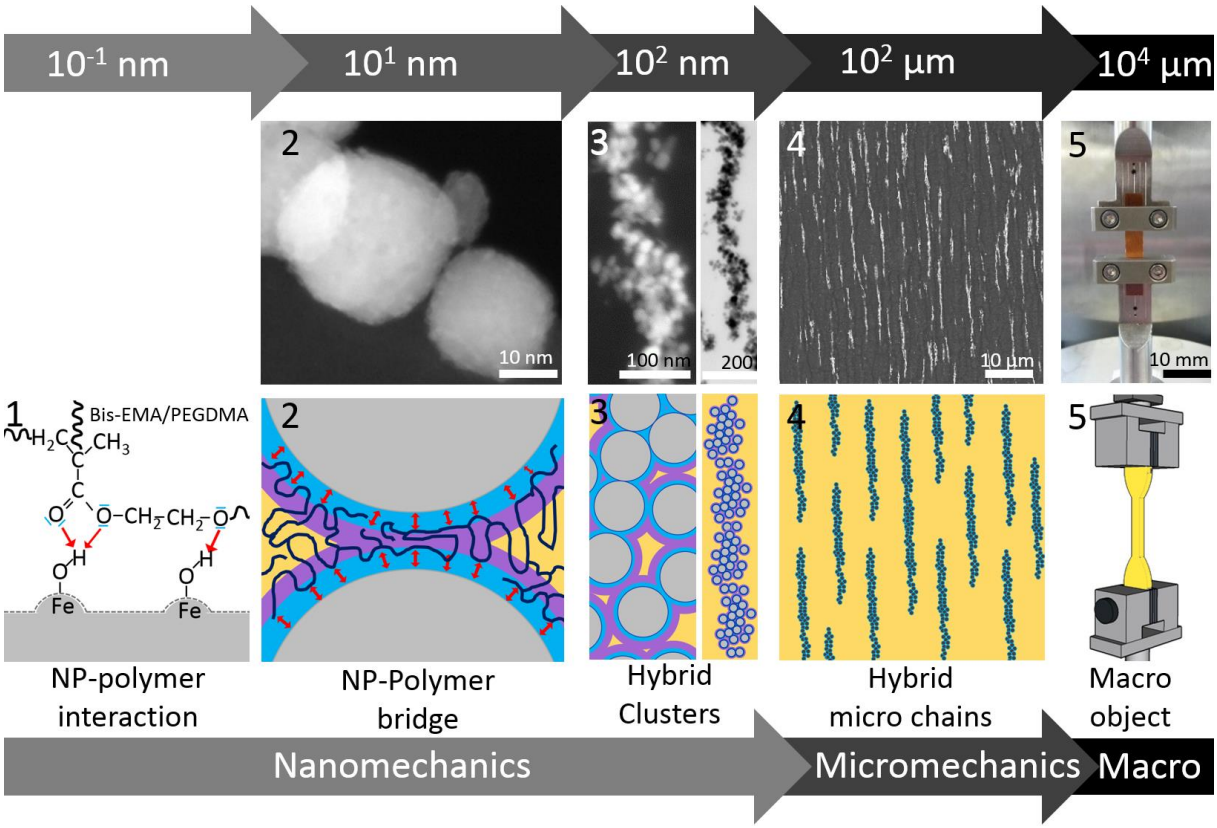

Figure 43 Model of magnetically assembled polymer nanocomposite with a multi-level hierarchy (bottom panel of the images) and the images of structural features at various levels (upper panel of the images). Arrows indicate a bottom-up formation of the material and the length scale of individual levels. Detailed description of the multi-level hierarchy is provided in following text bellow.

Multi-level hierarchy from nano to macro:

Level 1: Molecular level interaction and anchoring of polar groups in backbone of polymer chains with hydroxyl groups on the surface of inorganic nanoparticles.

Level 2: Adsorption of polymer chains due to molecular interaction with NP surface and confinement of polymer chains between close NPs resulting in different relaxation time compared to bulk matrix. Creation of layer of strongly adsorbed (blue) and much looser (purple) bounded segments creating diffuse layer gradually diminishing into bulk unaffected polymer (yellow).

Level 3: Percolation of NPs by direct NP-NP contacts and clustering via polymer segments creating the NP-polymer bridge. Here the interparticle interactions, deformation of polymer bridges plays pivotal role in stiffness of structure.

Level 4: Anisotropic hybrid micro superstructures with specific orientation and spatial arrangement distributed in bulk polymer matrix. Here, the continuum micromechanics models may be applied. The stiffness of the particle structure and surrounding matrix is E_F and E_M, respectively.

Level 5: Macroscopic object with a multi-level hierarchy.

direction isotropic – Trans. dir. iso. in legend of the graph). For PNC assembled in highest magnetic field B=50 mT after t_a=10 seconds and measured in transverse direction, course of storage modulus deviates and shows different elastic fragility when compared to other transversely oriented PNCs. This effect was already addressed via deformation of large laterally merged chains creating superstructures in with an aspect ratio, L/D≈10 (see Figure 37 for 50 mT sample – the length of the superstructure in transverse direction (~1 μm) / diameter of primary aggregates (~100 nm)). These values perfectly fit the linear trends. Also, relative composite's modulus at other temperatures (-50-170 °C) was analysed in identic way as a function of aspect ratio, but not presented here for clarity of the graph. The experimental data were fitted with linear trends having general formula: $y=y_0+\text{Slope}\cdot x$.The slope and offset ($y_0$) of the linear fits are plotted versus temperature in the Figure 44B. Their temperature dependency markedly follows the appearance of reinforcing ratio versus distance from T_g. Realizing the fact that these master curves are constructed from linear fits of experimental data of all PNCs regardless of their orientation to the macroscopic deformation, these temperature dependences needs to be connected to some universal stiffening mechanisms present in all systems – polymer vitrification. The offset (y_0) is proportional to the modification of the relaxation and vitrification properties of the polymer matrix in the proximity of MNPs – and consequently to stiffness of immobilized polymer. While the slope is proportional to the ability of structures to carry the load and undergo the deformation. The both are apparently temperature dependent with a maximum at ~100 °C. This temperature is very close to onset of rapid vitrification for neat matrix markedly seen at its storage modulus – see Figure 37A,B). Polymer chains in vicinity of the nanoparticles vitrify firstly (the increase of peak) and when bulk polymer matrix starts to vitrify as well, the stiffness difference between these two polymer fractions starts to diminish (decrease of peak). This will be commented in more detail soon.

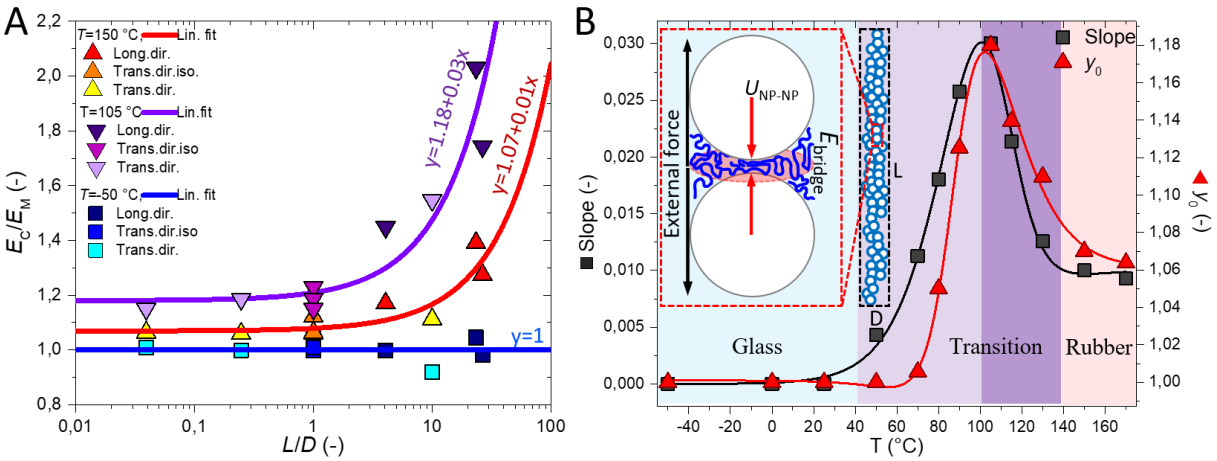

Figure 44 (A) Reinforcing effectivity as function of aspect ratio of the structures in semi log scale. Points represent experimental data fitted with the linear function – solid lines. (B) The slope and offset (y_0) of linear functions versus temperature. Inset in (B) depicts a contribution of individual components to the overall stiffness of hybrid microstructure.

The internal stiffness of the hybrid structure (E_F) was calculated using semi-empirical Halpin-Tsai model (*316*). This model is commonly used for prediction of the stiffness of polymers filled with micro fibers and derived in Equation (17). Model was set to perfectly fit the experimental data by adjusting the stiffness of fibres (E_F). The stiffness of hybrid fiber in rubbery plateau is around $E_{F\ 150\ °C}$~400 MPa. This value is one order of magnitude higher than stiffness of the surrounding rubbery matrix. Temperature dependency of hybrid fiber structure stiffness is plotted in Figure 46A. Halpin-Tsai predicts slightly higher modulus for other longitudinally oriented PNCs (5, 50 mT) (E_F=700-800 MPa). And rule of mixture model as upper limit for Halpin-Tsai model predicts a mean stiffness of hybrid fibers $E_{F\ 150\ °C}$~500 MPa using a simple formula, $E_C = E_F\phi_1 + E_M(1-\phi_1)$.

$$\frac{E_{HT}}{E_M} = \frac{1+A\cdot B\cdot\phi_1}{1-B\cdot\phi_1} \qquad \text{Equation (17)}$$

$$B = \frac{\frac{E_F}{E_M}-1}{\frac{E_F}{E_M}+A} \qquad \text{Equation (18)}$$

$$A = 2\frac{L}{D} \qquad \text{Equation (19)}$$

Where E_{HT} and E_M are moduli of composite and neat matrix, respectively and ϕ_1 is the volume fraction of reinforcing structures in surrounding matrix. Parameter B is the reinforcing ratio given by the Equation (18) where E_F is the tensile modulus of particle structure. Parameter A is the geometrical factor defined by the aspect ratio of the structure in Equation (19) with L and D as a length and width of structures with a respect to deformation direction. Aspect ratio listed in Figure 27A is used for longitudinal direction and inreverse values for transverse direction.

The stiffness of hybrid structure starts to rapidly increase from temperatures somewhere around 130-120 °C which is accompanied by the modulus upturn of its PNC. However, as vitrification of system proceeds the hybrid structure reach the maximum of its stiffness before reaching the T_g of the matrix. Stiffness of the hybrid structure seems to be constant and on the order of glassy matrix modulus far bellow T_g. Thus, it seems that structure was vitrified much earlier and at higher temperatures than surrounding matrix.

Continuum micromechanical interpretation of composite stiffness is only half of the mechanisms relying on load carrying capability of anisotropic structures and their stiffness which originates in nanoscopic interactions. More important question arise: *What causes the mechanical robustness of assemblie*? The finding of bridging laws between continuum macro/micromechanics and nanoscopic interactions might shed a light on the behaviour of complex nanostructures, biological structures and PNCs (*202*, *203*). For example, the extent of stress transfer into glass or carbon micro fibers depends on their length projected in tensile direction while their Young's modulus (E_F) is length independent and solely depends on the internal structure and stiffness of chemical bonds. The stiffness of hybrid structures is complex function of all nanoscopic mechanisms which contribute to nanoscopic deformations and hold the particle assemblies together such as: interparticle attractions (van der Waals, electrostatic,

magnetic, NP-NP interlocking, friction, etc.), deformation of particle atomistic structure, the strength of NP-polymer interactions and temperature dependent Young's modulus of polymer bridges (*297-299*) – see Figure 45 and inset in Figure 44B.

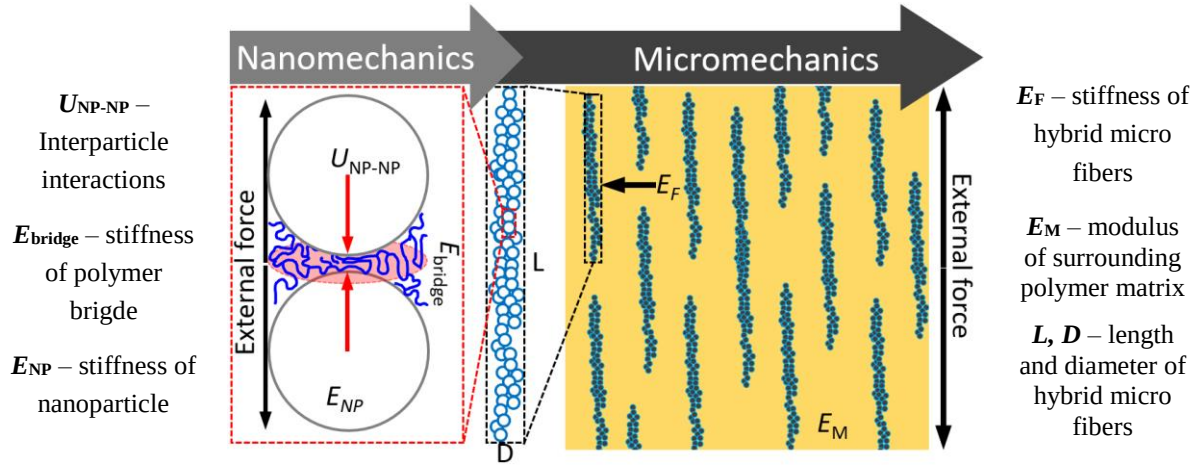

Figure 45 Proposed contribution of nanoscopic deformation mechanisms within the NP-polymer system to the overall macroscopic stiffness (E_F) of hybrid magnetically assembled particle chains (fibers) homogenously oriented in polymer matrix with a modulus (E_M).

The non-zero stiffness of NP-NP interaction might be an interesting concept, but stiffness of these interactions needs to be on the order of stiffness of surrounding medium to be reinforcing effective. This is for example outlined in Figure 15C. It is assumed that stiffness of particle structure and strength of van der Waals attraction is frequency independent in common frequency ranges (*295*) and presumably also temperature independent (or much negligibly compared to polymers). Also, magnetic interactions are expected to become stronger with decreasing temperature (Figure 21C) and thus it would significantly contributes to PNC's stiffness at low temperatures. This makes interpretation of temperature dependency of reinforcing ratio via interparticle forces quite hard. And if these NP-NP interactions contribute to mechanical robustness of PNCs in some way, their effect will be strongest mainly in rubbery region. Despite, mechanical properties of particle aggregates exhibit some elastic features and non-zero stiffness (*249-255*), only stiffness of NP-NP bonds itself cannot explain the viscoelastic behaviour and disappearance of the reinforcement effect in PNCs close to their T_g. This feature is general for all PNCs using matrices of various mechanical properties. Same effect of the temperature on the reinforcement of PNCs is observed in this work. This means that forces which support the load carrying capability of the structures depend on the actual stiffness of surrounding medium and bound polymer layers and their vitrification characteristics.

The contribution of bound layer and particle deformation is discussed further in text. Theory for orientation and temperature dependent reinforcement of magnetically structured PNCs from rubber to glass is schematically depicted in Figure 46B and described in following text. Author believes that this mechanism can be used for description of the temperature dependent

reinforcing effectivity in PNCs by a slight modification depending on the geometry of the particle assemblies varying from system to system.

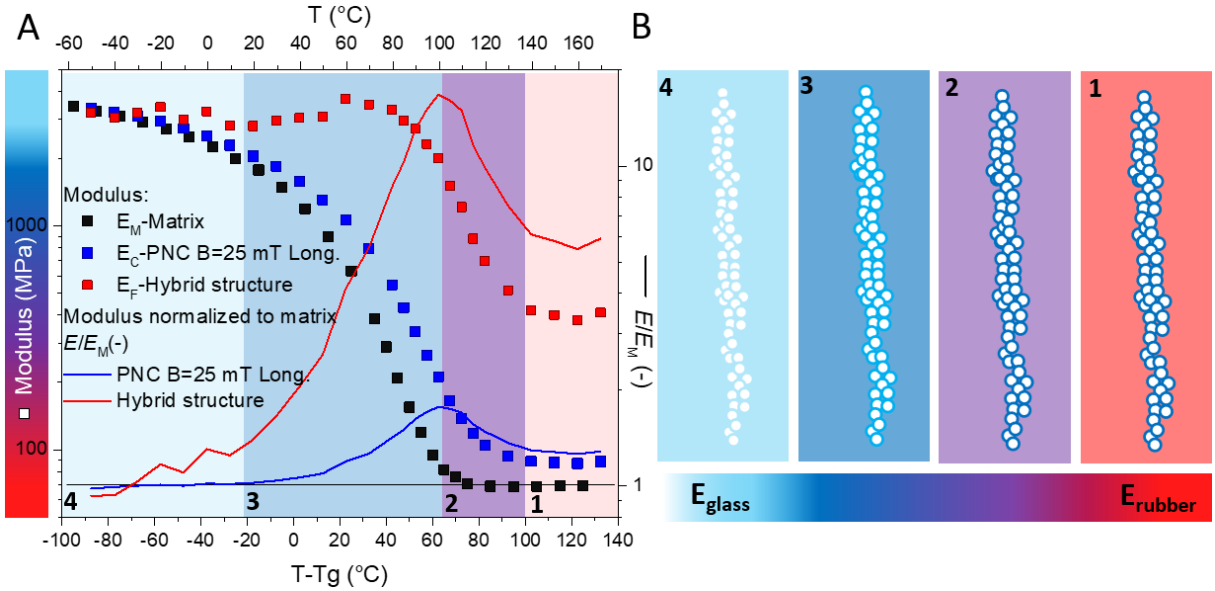

Figure 46 (A) Left *y*-axis – Dependency of calculated stiffness of hybrid structure (E_F) with modulus of neat matrix and PNC assembled in B=25 mT (square symbols □). Right *y*-axis – Relative ratio between stiffness of hybrid structure and its PNC normalized to matrix modulus (solid lines ─). (B) Schematic depiction of vitrification process from rubbery through transition to glassy region. Color bar indicates a stiffness of individual components – hybrid fibers and surrounding matrix. White color represents a stiffness of magnetite particles (~175 GPa).

Region 1 – Rubber

Existence of polymer segments with prolonged relaxation times in the presence of solid inclusion even far above *T*g was outlined – they are termed as '*glassy*'. Such polymer segments bridge MNPs clusters also in rubbery state of bulk matrix and give a rise to the stiffness of micro- and macroscopically percolated hybrid nanostructures. The stiffness of hybrid structure calculated using micromechanical models fairly aggress with this idea. The value of hybrid structure is one order of magnitude higher than modulus of neat rubbery matrix, see Figure 46A. The stress from the matrix is carried by the hybrid structure, due to large mismatch of their moduli, $E_F > E_M$ with 6-times higher stiffness than matrix. Also, structure orientation and its length play a role, thus self-assembled and transversely oriented systems are far less successful in system reinforcement and consequently they exhibit only small reinforcing peak (Figure 41) on contrary to longitudinal orientations.

In the soft polymers, the contribution of particle deformation to overall macroscopic deformation is negligible due to large stiffness mismatch with a surrounding medium – hydrodynamic effect of strain amplification (*288*). For example, tensile modulus of magnetite nanoparticles is reported to be ~175 GPa (*286*). Stress is concentrated outside the particles (*287*) and polymer bridge may experience significant overstraining to compensate the particle strain loss and to maintain total macroscopic strain (*317*). This causes non-affine deformation within

the clusters and vastly contribute to stress carried by polymer bridges. This may be also situation in highly filled PNCs while entropic contribution plays a certain role. Rather non-entropic contributions were ascribed to be responsible form upturn of mechanical reinforcement induced by NP assemblies (*288*). These effects are usually studied independently without concepts of glassy fraction or effect of particle interactions. Cross-linking density, stiffness-temperature dependence and distance of entrapped polymer from its T_g is not known due to expected lower polymerization yield of segments inside clusters. Calculation of local nanoscopic strain in polymer bridge appears as complex problem requiring further research and overlapping of multiple reinforcing mechanisms. Currently, contribution of this mechanism to reinforcement of studied systems cannot be quantitatively addressed.

Region 2 – Increase of reinforcing ratio

This region is relatively narrow however, the most intense reinforcement of PNC occurs mainly here. During cooling, storage modulus of PNC starts to upturn rapidly bellow ~140 °C while stiffness of matrix remains almost constant for longer period of temperatures, see Figure 46A. As temperature decreases, strongly adsorbed and confined polymer segments in the nearness of NPs vitrify as first and bound the whole hybrid structure by stiff polymer layer with a stiffness far exceeding the properties of bulk matrix which still remain in rubbery state ($E_F >> E_M$). At the end of this region, matrix's modulus starts to upturn as well, and it will slowly catch-up with a hybrid structure. In the addition to large mismatch between E_F and E_M, enhanced stiffness on the interface between bulky matrix and hybrid structure might be beneficial for loading the structures. With an increasing load, polymer bridges may experience much extensive strain amplification which may contribute to stiffness of structures as well.

Region 3 – Decrease of reinforcing ratio

In this region bulk matrix is progressively vitrified and its modulus catch-up with the hybrid structure. Matrix stiffness is gradually increasing and mismatch between E_F and E_M is slowly vanishing ($E_F > E_M$). As their ratio becomes smaller and smaller, micromechanical stress transfer is also more ineffective and less load is carried by hybrid structures. Hybrid structure reach its maximum vitrification degree at much higher temperatures when compared to neat matrix, see Figure 46A. Note that, maximum modulus of vitrified glassy structure is comparable with the modulus of matrix modulus far bellow T_g, such as $T=T_g$-100 °C. From this point, only matrix vitrifies and slowly wipes off the mismatch between moduli.

Region 4 – Glass

Since hybrid structure is already vitrified, only bulk matrix vitrifies with a vanishing of mismatch between their moduli around glass transition. Both phases are thus more or less the same glass ($E_F \approx E_M$) and reinforcement of PNCs modulus by the addition of NPs can be described by deformation of atomistic structure of filler phase – volume replacement. Discrepancies and shifting of modulus along *y*-axis may be attributed to significant confinement, anisotropic coil shapes, or enormous physico-chemical cross-linking with NPs.

4 Conclusion

The first part of dissertation thesis deals with a structuring phenomenon of polymer nanocomposites by guide of the external magnetic field. In contrary to self-assembly of nanoparticle, this method offers a possibility to control the morphology of particles assemblies, their orientation and anisotropy in bottom-up manner. Structuring of magnetic PNCs was studied in various systems with different viscosities including dispersed MNPs in acetone and in the presence of small amount of PMMA polymer, MNPs in photopolymerizable methacrylate resin or polyurethane matrix.

In general, NPs and MNPs in polymer liquids often exhibit complex bottom-up aggregation processes observed also in this work, since no surface stabilization or grafting of MNPs was used. By the analysing of the literature aiming on the magnetic PNCs, it seems that successful dispersion of MNPs in the presence of polymers might require non-trivial solutions. The effect of the magnetic interactions ensured by non-zero magnetic moment of dipoles was studied to describe the aggregation nature of MNPs. Calculations of van der Waals and magnetic attraction exhibit the regions where particles are close enough to be magnetically attracted across relatively large distances. The addition of only 1 vol. % of MNPs with sufficiently strong magnetic moment was shown to cause aggregation of MNPs into complex shapes even in absence of the external magnetic field.

The application of magnetic field of various strengths resulted in controlled structuring of magnetic material in polymer matrix into anisotropic one-dimensional particle chains. No regular packing of particles within the structures was observed. The kinetics of assembling process in magnetic field was studied. It is shown that structure in low magnetic field (B=5 mT) are slowly deposited along the field direction however, the growth of the building-blocks maintains self-assembly nature. Also, fractal-like aggregates with an anisotropy and percolation on the micro length scales were fabricated in PNCs filled with 2 vol. % of MNPs. The application of higher magnetic fields (B=25 and 50 mT) led to rapid arrangement of particles and their self-assembled aggregates into high aspect ratio structures homogeneously oriented within the polymeric material. While, relatively small microchains were created after short assembling times (t_a=10 sec.), structures assembled after longer times gradually transform to large microscopic fibers. The similar objects are assembled from the acetone suspensions of MNPs in presence of small amount of PMMA. Lower viscosity of the system is favourable for extremely fast assembling due to vanishing of kinetical barrier. It has been shown that the controlling of assembling process by the strength of external field, particle volume fraction, viscosity of medium and assembling time leads to variety of magnetic structures which may find their usage in PNCs technology and/or fundamental types of studies. For example, implementation of controlled structuring of nanostructure of liquid material in the additive fabrication technology might lead to bottom-up fabrication of mechanically robust materials with multi-level hierarchies.

The second part of dissertation thesis is focused on the mechanical properties of PNCs. Mechanical response was studied for the photopolymer and polyurethane samples containing low volume fraction of MNPs structured into one-dimensional assemblies by dynamic mechanical analysis in linear deformation regime. Significant anisotropy of magnetic PNCs was observed for longitudinally and transversely oriented structures. On the other hand, reinforcement of polymer matrix was observed only above the glass transition of matrix which is classic signature of PNCs. Because there is no strictly accepted theory for PNCs reinforcement in the scientific community, various concepts are discussed in more detail alongside the measured mechanical properties of prepared PNCs. Reinforcement effect of particle structures in the polymer matrix exhibits significant temperature dependence with a maximum in the temperature region around T_g+60°C. Longitudinally oriented structures exhibit considerably larger reinforcing capability. Anisotropy of PNCs systems was described by the different load carrying capability which is higher for longitudinally oriented structures while transversely oriented structures contribute only negligibly to mechanical robustness on PNC. The structure of magnetically assembled PNCs on the different length scales was analysed by hierarchic model of material with various contributions of individual levels of material to mechanical properties. At the micro scale level, approximation of anisotropic particle structures by solid hybrid fibers with a non-zero stiffness was utilized in the combination with micromechanics model for composite system. Temperature dependent stiffness of hybrid structures was calculated using Halpin-Tsai model exhibiting much higher stiffness than surrounding matrix. The intrinsic stiffness of magnetically structures were attributed to vitrification of polymer segments in the vicinity and confined by MNPs. These polymer segments penetrate thorough the particle structures and transmit the stress. The presence of polymer bridge with sufficiently high molecular weight and stiffness is absolutely essential for the mechanical robustness of PNCs. Proposed theory of reinforcement can be generally applied for all PNCs creating nano-, submicro-, micro- and macro particle structures. In cases studied here, anisotropic micro particle structures are created by magnetic guidance. In the future research, induced particles structures with controlled morphologies inside the polymer matrix could be utilized for gaining of better knowledge and understanding in the field of PNCs and/or even provide final answers for various disagreements and uncertainties between individual concepts established in this field.

References

1. G. M. Whitesides, B. Grzybowski, Self-assembly at all scales. *Science* 295, 2418-2421 (2002).
2. M. A. Boles, M. Engel, D. V. Talapin, Self-Assembly of Colloidal Nanocrystals: From Intricate Structures to Functional Materials. *Chemical Reviews* 116, 11220-11289 (2016).
3. O. D. Velev, S. Gupta, Materials Fabricated by Micro- and Nanoparticle Assembly - The Challenging Path from Science to Engineering. *Advanced Materials* 21, 1897-1905 (2009).
4. K. J. M. Bishop, C. E. Wilmer, S. Soh, B. A. Grzybowski, Nanoscale Forces and Their Uses in Self-Assembly. *Small* 5, 1600-1630 (2009).
5. J. B. Hooper, K. S. Schweizer, Contact aggregation, bridging, and steric stabilization in dense polymer-particle mixtures. *Macromolecules* 38, 8858-8869 (2005).
6. J. B. Hooper, K. S. Schweizer, Real space structure and scattering patterns of model polymer nanocomposites. *Macromolecules* 40, 6998-7008 (2007).
7. G. Nichols *et al.*, A review of the terms agglomerate and aggregate with a recommendation for nomenclature used in powder and particle characterization. *J. Pharm. Sci.* 91, 2103-2109 (2002).
8. J. B. Hooper, K. S. Schweizer, T. G. Desai, R. Koshy, P. Keblinski, Structure, surface excess and effective interactions in polymer nanocomposite melts and concentrated solutions. *Journal of Chemical Physics* 121, 6986-6997 (2004).
9. J. B. Hooper, K. S. Schweizer, Theory of phase separation in polymer nanocomposites. *Macromolecules* 39, 5133-5142 (2006).
10. C. Housmans, M. Sferrazza, S. Napolitano, Kinetics of Irreversible Chain Adsorption. *Macromolecules* 47, 3390-3393 (2014).
11. B. Carroll, S. W. Cheng, A. P. Sokolov, Analyzing the Interfacial Layer Properties in Polymer Nanocomposites by Broadband Dielectric Spectroscopy. *Macromolecules* 50, 6149-6163 (2017).
12. S. E. Harton *et al.*, Immobilized Polymer Layers on Spherical Nanoparticles. *Macromolecules* 43, 3415-3421 (2010).
13. S. W. Cheng *et al.*, Interfacial Properties of Polymer Nanocomposites: Role of Chain Rigidity and Dynamic Heterogeneity Length Scale. *Macromolecules* 50, 2397-2406 (2017).
14. N. Jouault, D. Zhao, S. K. Kumar, Role of Casting Solvent on Nanoparticle Dispersion in Polymer Nanocomposites. *Macromolecules* 47, 5246-5255 (2014).
15. S. K. Kumar, N. Jouault, B. Benicewicz, T. Neely, Nanocomposites with Polymer Grafted Nanoparticles. *Macromolecules* 46, 3199-3214 (2013).
16. P. Akcora *et al.*, Anisotropic self-assembly of spherical polymer-grafted nanoparticles. *Nature Materials* 8, 354-U121 (2009).
17. H. R. Dennis *et al.*, Effect of melt processing conditions on the extent of exfoliation in organoclay-based nanocomposites. *Polymer* 42, 9513-9522 (2001).
18. S. S. Ray, M. Okamoto, Polymer/layered silicate nanocomposites: a review from preparation to processing. *Progress in Polymer Science* 28, 1539-1641 (2003).
19. D. R. Paul, L. M. Robeson, Polymer nanotechnology: Nanocomposites. *Polymer* 49, 3187-3204 (2008).
20. J. Alvarado, G. Acosta, F. Perez, Study of the effect of the dispersion of functionalized nanoparticles TiO2 with photocatalytic activity in LDPE. *Polym. Degrad. Stabil.* 134, 376-382 (2016).

21. H. Kim, Y. Miura, C. W. Macosko, Graphene/Polyurethane Nanocomposites for Improved Gas Barrier and Electrical Conductivity. *Chemistry of Materials* 22, 3441-3450 (2010).
22. Q. F. Li *et al.*, Responsive assemblies: Gold nanoparticles with mixed ligands in microphase separated block copolymers. *Advanced Materials* 20, 1462-+ (2008).
23. P. Lepcio *et al.*, Bulk polymer nanocomposites with preparation protocol governed nanostructure: the origin and properties of aggregates and polymer bound clusters. *Soft Matter* 14, 2094-2103 (2018).
24. D. Zhao, D. Schneider, G. Fytas, S. K. Kumar, Controlling the Thermomechanical Behavior of Nanoparticle/Polymer Films. *Acs Nano* 8, 8163-8173 (2014).
25. M. E. Mackay *et al.*, General strategies for nanoparticle dispersion. *Science* 311, 1740-1743 (2006).
26. J. Kao, K. Thorkelsson, P. Bai, B. J. Rancatore, T. Xu, Toward functional nanocomposites: taking the best of nanoparticles, polymers, and small molecules. *Chemical Society Reviews* 42, 2654-2678 (2013).
27. B. Yuan, L. Cademartiri, Flexible One-Dimensional Nanostructures: A Review. *Journal of Materials Science & Technology* 31, 607-615 (2015).
28. J. W. Liu, H. W. Liang, S. H. Yu, Macroscopic-Scale Assembled Nanowire Thin Films and Their Functionalities. *Chemical Reviews* 112, 4770-4799 (2012).
29. M. Grzelczak, J. Vermant, E. M. Furst, L. M. Liz-Marzan, Directed Self-Assembly of Nanoparticles. *Acs Nano* 4, 3591-3605 (2010).
30. Y. J. Min, M. Akbulut, K. Kristiansen, Y. Golan, J. Israelachvili, The role of interparticle and external forces in nanoparticle assembly. *Nature Materials* 7, 527-538 (2008).
31. N. T. Nguyen, Micro-magnetofluidics: interactions between magnetism and fluid flow on the microscale. *Microfluidics and Nanofluidics* 12, 1-16 (2012).
32. M. F. Shao *et al.*, Preparation of Fe3O4@SiO2@Layered Double Hydroxide Core-Shell Microspheres for Magnetic Separation of Proteins. *Journal of the American Chemical Society* 134, 1071-1077 (2012).
33. T. C. Halsey, ELECTRORHEOLOGICAL FLUIDS. *Science* 258, 761-766 (1992).
34. S. O. Lumsdon, E. W. Kaler, O. D. Velev, Two-dimensional crystallization of microspheres by a coplanar AC electric field. *Langmuir* 20, 2108-2116 (2004).
35. J. M. McMullan, N. J. Wagner, Directed self-assembly of colloidal crystals by dielectrophoretic ordering observed with small angle neutron scattering (SANS). *Soft Matter* 6, 5443-5450 (2010).
36. J. M. McMullan, N. J. Wagner, Directed Self-Assembly of Colloidal Crystals by Dielectrophoretic Ordering. *Langmuir* 28, 4123-4130 (2012).
37. M. E. Leunissen, H. R. Vutukuri, A. van Blaaderen, Directing Colloidal Self-Assembly with Biaxial Electric Fields. *Advanced Materials* 21, 3116-+ (2009).
38. J. Rayeendran, J. A. Wood, A. Docoslis, Contact-Free Templating of 3-D Colloidal Structures Using Spatially Nonuniform AC Electric Fields. *Langmuir* 32, 9619-9632 (2016).
39. S. Gangwal, O. J. Cayre, O. D. Velev, Dielectrophoretic Assembly of Metallodielectric Janus Particles in AC Electric Fields. *Langmuir* 24, 13312-13320 (2008).
40. K. D. Hermanson, S. O. Lumsdon, J. P. Williams, E. W. Kaler, O. D. Velev, Dielectrophoretic assembly of electrically functional microwires from nanoparticle suspensions. *Science* 294, 1082-1086 (2001).
41. M. Sam, N. Moghimian, R. B. Bhiladvala, Field-directed chaining of nanowires: towards transparent electrodes. *Materials Letters* 163, 205-208 (2016).

42. A. I. Oliva-Aviles, F. Aviles, V. Sosa, Electrical and piezoresistive properties of multi-walled carbon nanotube/polymer composite films aligned by an electric field. *Carbon* 49, 2989-2997 (2011).
43. M. Monti, M. Natali, L. Torre, J. M. Kenny, The alignment of single walled carbon nanotubes in an epoxy resin by applying a DC electric field. *Carbon* 50, 2453-2464 (2012).
44. R. B. Ladani *et al.*, Multifunctional properties of epoxy nanocomposites reinforced by aligned nanoscale carbon. *Materials & Design* 94, 554-564 (2016).
45. M. S. Kumar *et al.*, DC electric field assisted alignment of carbon nanotubes on metal electrodes. *Solid-State Electron.* 47, 2075-2080 (2003).
46. M. S. Kumar *et al.*, Influence of electric field type on the assembly of single walled carbon nanotubes. *Chemical Physics Letters* 383, 235-239 (2004).
47. C. A. Martin *et al.*, Electric field-induced aligned multi-wall carbon nanotube networks in epoxy composites. *Polymer* 46, 877-886 (2005).
48. L. Valentini, S. B. Bon, J. M. Kenny, Anisotropic Electrical Transport Properties of Aligned Carbon Nanotube/PMMA Films Obtained by Electric-Field-Assisted Thermal Annealing. *Macromolecular Materials and Engineering* 293, 867-871 (2008).
49. S. Y. Wu *et al.*, Aligning multilayer graphene flakes with an external electric field to improve multifunctional properties of epoxy nanocomposites. *Carbon* 94, 607-618 (2015).
50. J. K. Kawasaki, C. B. Arnold, Synthesis of Platinum Dendrites and Nanowires Via Directed Electrochemical Nanowire Assembly. *Nano Letters* 11, 781-785 (2011).
51. A. Nerowski, J. Opitz, L. Baraban, G. Cuniberti, Bottom-up synthesis of ultrathin straight platinum nanowires: Electric field impact. *Nano Research* 6, 303-311 (2013).
52. A. Nerowski, M. Poetschke, M. Bobeth, J. Opitz, G. Cuniberti, Dielectrophoretic Growth of Platinum Nanowires: Concentration and Temperature Dependence of the Growth Velocity. *Langmuir* 28, 7498-7504 (2012).
53. A. Nerowski *et al.*, Effect of Waveform of ac Voltage on the Morphology and Crystallinity of Electrochemically Assembled Platinum Nanowires. *Langmuir* 30, 5655-5661 (2014).
54. J. L. Liu *et al.*, Electrophoretic deposition of fluorescent Cu and Au sheets for light-emitting diodes. *Nanoscale* 8, 395-402 (2016).
55. M. S. Wang, L. He, Y. D. Yin, Magnetic field guided colloidal assembly. *Materials Today* 16, 110-116 (2013).
56. J. B. Tracy, T. M. Crawford, Magnetic field-directed self-assembly of magnetic nanoparticles. *Mrs Bulletin* 38, 915-920 (2013).
57. D. Jiles, *Introduction to magnetism and magnetic materials*. (Chapman and Hall, ed. 1st, 1991).
58. S. A. Majetich, M. Sachan, Magnetostatic interactions in magnetic nanoparticle assemblies: energy, time and length scales. *Journal of Physics D-Applied Physics* 39, R407-R422 (2006).
59. S. Sierra-Bermudez, L. P. Maldonado-Camargo, F. Orange, M. J. F. Guinel, C. Rinaldi, Assessing magnetic nanoparticle aggregation in polymer melts by dynamic magnetic susceptibility measurements. *J. Magn. Magn. Mater.* 378, 64-72 (2015).
60. L. Maldonado-Camargo, C. Rinaldi, Breakdown of the Stokes-Einstein Relation for the Rotational Diffusivity of Polymer Grafted Nanoparticles in Polymer Melts. *Nano Letters* 16, 6767-6773 (2016).
61. K. Chiba, S. Chikazumi, MAGNETOCRYSTALLINE ANISOTROPY OF MAGNETITE. *J. Magn. Magn. Mater.* 31-4, 813-814 (1983).

62. W. Williams, D. J. Dunlop, SIMULATION OF MAGNETIC HYSTERESIS IN PSEUDO-SINGLE-DOMAIN GRAINS OF MAGNETITE. *Journal of Geophysical Research-Solid Earth* 100, 3859-3871 (1995).
63. Q. S. Liu *et al.*, ENVIRONMENTAL MAGNETISM: PRINCIPLES AND APPLICATIONS. *Reviews of Geophysics* 50, 50 (2012).
64. K. P. Ge, Q. S. Liu, Effects of the grain size distribution on magnetic properties of magnetite: constraints from micromagnetic modeling. *Chinese Science Bulletin* 59, 4763-4773 (2014).
65. P. Panda, K. W. Bong, T. A. Hatton, P. S. Doyle, Branched Networks by Directed Assembly of Shape Anisotropic Magnetic Particles. *Langmuir* 27, 13428-13435 (2011).
66. S. E. Kushnir, P. E. Kazin, L. A. Trusov, Y. D. Tretyakov, Self-organization of micro- and nanoparticles in ferrofluids. *Russian Chemical Reviews* 81, 560-570 (2012).
67. B. Bharti, A. L. Fameau, M. Rubinstein, O. D. Velev, Nanocapillarity-mediated magnetic assembly of nanoparticles into ultraflexible filaments and reconfigurable networks. *Nature Materials* 14, 1104-+ (2015).
68. E. P. Furlani, Analysis of particle transport in a magnetophoretic microsystem. *Journal of Applied Physics* 99, 11 (2006).
69. G. J. Cheng, D. Romero, G. T. Fraser, A. R. H. Walker, Magnetic-field-induced assemblies of cobalt nanoparticles. *Langmuir* 21, 12055-12059 (2005).
70. L. He, M. Wang, J. Ge, Y. Yin, Magnetic Assembly Route to Colloidal Responsive Photonic Nanostructures. *Accounts of Chemical Research* 45, 1431-1440 (2012).
71. S. L. Tripp, S. V. Pusztay, A. E. Ribbe, A. Wei, Self-assembly of cobalt nanoparticle rings. *Journal of the American Chemical Society* 124, 7914-7915 (2002).
72. Y. Takeno *et al.*, Morphology and magnetic flux distribution in superparamagnetic, single-crystalline Fe3O4 nanoparticle rings. *Appl. Phys. Lett.* 105, 5 (2014).
73. D. Lisjak, P. Jenus, A. Mertelj, Influence of the Morphology of Ferrite Nanoparticles on the Directed Assembly into Magnetically Anisotropic Hierarchical Structures. *Langmuir* 30, 6588-6595 (2014).
74. S. Kralj, D. Makovec, Magnetic Assembly of Superparamagnetic Iron Oxide Nanoparticle Clusters into Nano chains and Nanobundles. *Acs Nano* 9, 9700-9707 (2015).
75. A. Snezhko, I. S. Aranson, Magnetic manipulation of self-assembled colloidal asters. *Nature Materials* 10, 698-703 (2011).
76. J. H. E. Promislow, A. P. Gast, Low-energy suspension structure of a magnetorheological fluid. *Physical Review E* 56, 642-651 (1997).
77. J. Lin *et al.*, Gold-coated iron (Fe@Au) nanoparticles: Synthesis, characterization, and magnetic field-induced self-assembly. *Journal of Solid State Chemistry* 159, 26-31 (2001).
78. W. L. Zhou *et al.*, Nanostructures of gold coated iron core-shell nanoparticles and the nanobands assembled under magnetic field. *European Physical Journal D* 16, 289-292 (2001).
79. K. Butter, P. H. H. Bomans, P. M. Frederik, G. J. Vroege, A. P. Philipse, Direct observation of dipolar chains in iron ferrofluids by cryogenic electron microscopy. *Nature Materials* 2, 88-91 (2003).
80. Y. Sahoo *et al.*, Field-directed self-assembly of magnetic nanoparticles. *Journal of Physical Chemistry B* 108, 3380-3383 (2004).
81. Y. Lalatonne, J. Richardi, M. P. Pileni, Van der Waals versus dipolar forces controlling mesoscopic organizations of magnetic nanocrystals. *Nature Materials* 3, 121-125 (2004).
82. R. Dreyfus *et al.*, Microscopic artificial swimmers. *Nature* 437, 862-865 (2005).

83. J. H. Gao, B. Zhang, X. X. Zhang, B. Xu, Magnetic-dipolar-interaction-induced self-assembly affords wires of hollow nanocrystals of cobalt selenide. *Angewandte Chemie-International Edition* 45, 1220-1223 (2006).
84. J. P. Ge, Y. X. Hu, M. Biasini, W. P. Beyermann, Y. D. Yin, Superparamagnetic magnetite colloidal nanocrystal clusters. *Angewandte Chemie-International Edition* 46, 4342-4345 (2007).
85. Y. Hu, L. He, Y. Yin, Magnetically Responsive Photonic Nanochains. *Angewandte Chemie-International Edition* 50, 3747-3750 (2011).
86. Q. Zhang *et al.*, Photonic Labyrinths: Two-Dimensional Dynamic Magnetic Assembly and in Situ Solidification. *Nano Letters* 13, 1770-1775 (2013).
87. T. Ding, K. Song, K. Clays, C.-H. Tung, Fabrication of 3D Photonic Crystals of Ellipsoids: Convective Self-Assembly in Magnetic Field. *Advanced Materials* 21, 1936-1940 (2009).
88. J. J. Weis, Orientational structure of quasi-two-dimensional dipolar hard spheres. *Mol. Phys.* 93, 361-364 (1998).
89. J. J. Weis, Simulation of quasi-two-dimensional dipolar systems. *J. Phys.-Condes. Matter* 15, S1471-S1495 (2003).
90. J. J. Weis, Low density quasi-two-dimensional dipolar hard spheres in an external field. *Mol. Phys.* 103, 7-10 (2005).
91. J. Richardi, M. P. Pileni, J. J. Weis, Self-organization of magnetic nanoparticles: A Monte Carlo study. *Physical Review E* 77, 9 (2008).
92. J. Richardi, M. P. Pileni, J. J. Weis, Self-organization of confined dipolar particles in a parallel field. *Journal of Chemical Physics* 130, 6 (2009).
93. C. Salzemann, J. Richardi, I. Lisiecki, J. J. Weis, M. P. Pileni, Mesoscopic Void Structures in Cobalt Nanocrystal Films Formed from Drying Concentrated Colloidal Solutions. *Physical Review Letters* 102, 4 (2009).
94. J. Richardi, J. J. Weis, Low density mesostructures of confined dipolar particles in an external field. *Journal of Chemical Physics* 135, 10 (2011).
95. J. Richardi, J. J. Weis, Influence of short range potential on field induced chain aggregation in low density dipolar particles. *Journal of Chemical Physics* 138, 4 (2013).
96. C. Y. Hong *et al.*, Ordered structures in Fe3O4 kerosene-based ferrofluids. *Journal of Applied Physics* 81, 4275-4277 (1997).
97. C. Petit, J. Legrand, V. Russier, M. P. Pileni, Three dimensional arrays of cobalt nanocrystals: Fabrication and magnetic properties. *Journal of Applied Physics* 91, 1502-1508 (2002).
98. A. T. Ngo, M. P. Pileni, Nanoparticles of cobalt ferrite: Influence of the applied field on the organization of the nanocrystals on a substrate and on their magnetic properties. *Advanced Materials* 12, 276-279 (2000).
99. A. T. Ngo, M. P. Pileni, Cigar-shaped ferrite nanocrystals: Orientation of the easy magnetic axes. *Journal of Applied Physics* 92, 4649-4652 (2002).
100. A. T. Ngo, M. P. Pileni, Assemblies of cigar-shaped ferrite nanocrystals: orientation of the easy magnetization axes. *Colloid Surf. A-Physicochem. Eng. Asp.* 228, 107-117 (2003).
101. Y. Lalatonne *et al.*, Mesoscopic structures of nanocrystals: Collective magnetic properties due to the alignment of nanocrystals. *Journal of Physical Chemistry B* 108, 1848-1854 (2004).
102. Y. Lalatonne, L. Motte, J. Richardi, M. P. Pileni, Influence of short-range interactions on the mesoscopic organization of magnetic nanocrystals. *Physical Review E* 71, 10 (2005).

103. V. Germain, J. Richardi, A. Ingert, M. P. Pileni, Mesostructures of cobalt nanocrystals. 1. Experiment and theory. *Journal of Physical Chemistry B* 109, 5541-5547 (2005).
104. A. P. Hynninen, M. Dijkstra, Phase diagram of dipolar hard and soft spheres: Manipulation of colloidal crystal structures by an external field. *Physical Review Letters* 94, 4 (2005).
105. J. W. Swan, J. L. Bauer, Y. F. Liu, E. M. Furst, Directed colloidal self-assembly in toggled magnetic fields. *Soft Matter* 10, 1102-1109 (2014).
106. L. Ye, T. Pearson, Y. Cordeau, O. T. Mefford, T. M. Crawford, Triggered self-assembly of magnetic nanoparticles. *Scientific Reports* 6, 9 (2016).
107. J. H. E. Promislow, A. P. Gast, Magnetorheological fluid structure in a pulsed magnetic field. *Langmuir* 12, 4095-4102 (1996).
108. M. Klokkenburg *et al.*, In situ imaging of field-induced hexagonal columns in magnetite ferrofluids. *Physical Review Letters* 97, 4 (2006).
109. P. Y. Keng *et al.*, Colloidal Polymerization of Polymer-Coated Ferromagnetic Nanoparticles into Cobalt Oxide Nanowires. *Acs Nano* 3, 3143-3157 (2009).
110. L. J. Hill, J. Pyun, Colloidal Polymers via Dipolar Assembly of Magnetic Nanoparticle Monomers. *Acs Applied Materials & Interfaces* 6, 6022-6032 (2014).
111. J. P. Ge, L. He, Y. X. Hu, Y. D. Yin, Magnetically induced colloidal assembly into field-responsive photonic structures. *Nanoscale* 3, 177-183 (2011).
112. H. Kim *et al.*, Structural colour printing using a magnetically tunable and lithographically fixable photonic crystal. *Nat. Photonics* 3, 534-540 (2009).
113. L. He *et al.*, Magnetic Assembly of Nonmagnetic Particles into Photonic Crystal Structures. *Nano Letters* 10, 4708-4714 (2010).
114. J. P. Ge, Y. X. Hu, T. R. Zhang, T. Huynh, Y. D. Yin, Self-assembly and field-responsive optical diffractions of superparamagnetic colloids. *Langmuir* 24, 3671-3680 (2008).
115. J. P. Ge, Y. X. Hu, Y. D. Yin, Highly tunable superparamagnetic colloidal photonic crystals. *Angewandte Chemie-International Edition* 46, 7428-7431 (2007).
116. J. P. Ge, L. He, J. Goebl, Y. D. Yin, Assembly of Magnetically Tunable Photonic Crystals in Nonpolar Solvents. *Journal of the American Chemical Society* 131, 3484-+ (2009).
117. J. P. Ge, Y. D. Yin, Magnetically tunable colloidal photonic structures in alkanol solutions. *Advanced Materials* 20, 3485-+ (2008).
118. J. P. Ge *et al.*, Magnetochromatic Microspheres: Rotating Photonic Crystals. *Journal of the American Chemical Society* 131, 15687-15694 (2009).
119. L. He *et al.*, Assembly and Photonic Properties of Superparamagnetic Colloids in Complex Magnetic Fields. *Langmuir* 27, 13444-13450 (2011).
120. L. He, M. S. Wang, Q. Zhang, Y. Lu, Y. D. Yin, Magnetic Assembly and Patterning of General Nanoscale Materials through Nonmagnetic Templates. *Nano Letters* 13, 264-271 (2013).
121. S. M. Taheri *et al.*, Self-assembly of smallest magnetic particles. *Proceedings of the National Academy of Sciences of the United States of America* 112, 14484-14489 (2015).
122. A. Ahniyaz, Y. Sakamoto, L. Bergstrom, Magnetic field-induced assembly of oriented superlattices from maghemite nanocubes. *Proceedings of the National Academy of Sciences of the United States of America* 104, 17570-17574 (2007).
123. C. J. Chen, R. K. Chiang, Y. R. Jeng, Crystallization and Magnetic Properties of 3D Micrometer-Scale Simple-Cubic Maghemite Superlattices. *Journal of Physical Chemistry C* 115, 18142-18148 (2011).

124. G. Singh *et al.*, Magnetic field-induced self-assembly of iron oxide nanocubes. *Faraday Discuss.* 181, 403-421 (2015).
125. Y. Tang, Q. W. Chen, R. S. Chen, Magnetic field induced controllable self-assembly of maghemite nanocrystals: From 3D arrays to 1D nanochains. *Applied Surface Science* 347, 202-207 (2015).
126. G. Singh *et al.*, Self-assembly of magnetite nanocubes into helical superstructures. *Science* 345, 1149-1153 (2014).
127. H. L. Niu, Q. W. Chen, H. F. Zhu, Y. S. Lin, X. Zhang, Magnetic field-induced growth and self-assembly of cobalt nanocrystallites. *Journal of Materials Chemistry* 13, 1803-1805 (2003).
128. B. P. Jia, L. Gao, Morphological transformation of Fe3O4 spherical aggregates from solid to hollow and their self-assembly under an external magnetic field. *Journal of Physical Chemistry C* 112, 666-671 (2008).
129. J. H. Schenkel, A. Samanta, B. J. Ravoo, Self-Assembly of Soft Hybrid Materials Directed by Light and a Magnetic Field. *Advanced Materials* 26, 1076-1080 (2014).
130. S. Abramson, V. Dupuis, S. Neveu, P. Beaunier, D. Montero, Preparation of Highly Anisotropic Cobalt Ferrite/Silica Microellipsoids Using an External Magnetic Field. *Langmuir* 30, 9190-9200 (2014).
131. Q. A. Pankhurst, J. Connolly, S. K. Jones, J. Dobson, Applications of magnetic nanoparticles in biomedicine. *Journal of Physics D-Applied Physics* 36, R167-R181 (2003).
132. S. C. McBain, H. H. P. Yiu, J. Dobson, Magnetic nanoparticles for gene and drug delivery. *Int. J. Nanomed.* 3, 169-180 (2008).
133. D. C. Li, J. Rogers, S. L. Biswal, Probing the Stability of Magnetically Assembled DNA-Linked Colloidal Chains. *Langmuir* 25, 8944-8950 (2009).
134. D. Choi *et al.*, Transport of living cells with magnetically assembled nanowires. *Biomed. Microdevices* 9, 143-148 (2007).
135. S. Ghosh, S. R. P. Kumar, I. K. Puri, S. Elankumaran, Magnetic assembly of 3D cell clusters: visualizing the formation of an engineered tissue. *Cell Prolif.* 49, 134-144 (2016).
136. G. R. Souza *et al.*, Three-dimensional tissue culture based on magnetic cell levitation. *Nature Nanotechnology* 5, 291-296 (2010).
137. J. Jestin *et al.*, Anisotropic reinforcement of nanocomposites tuned by magnetic orientation of the filler network. *Advanced Materials* 20, 2533-+ (2008).
138. D. Fragouli *et al.*, Dynamical Formation of Spatially Localized Arrays of Aligned Nanowires in Plastic Films with Magnetic Anisotropy. *Acs Nano* 4, 1873-1878 (2010).
139. A. S. Robbes *et al.*, Nanocomposite Materials with Controlled Anisotropic Reinforcement Triggered by Magnetic Self-Assembly. *Macromolecules* 44, 8858-8865 (2011).
140. K. E. Roskov, J. E. Atkinson, L. M. Bronstein, R. J. Spontak, Magnetic field-induced alignment of nanoparticles in electrospun microfibers. *Rsc Advances* 2, 4603-4607 (2012).
141. H. Y. Yuan *et al.*, Facile Assembly of Aligned Magnetic Nanoparticle Chains in Polymer Nanocomposite Films by Magnetic Flow Coating. *Acs Applied Materials & Interfaces* 9, 11290-11298 (2017).
142. Z. Rigbi, J. E. Mark, EFFECTS OF A MAGNETIC-FIELD APPLIED DURING THE CURING OF A POLYMER LOADED WITH MAGNETIC FILLER. *Journal of Polymer Science Part B-Polymer Physics* 23, 1267-1269 (1985).

143. G. B. Sohoni, J. E. Mark, ANISOTROPIC REINFORCEMENT IN ELASTOMERS CONTAINING MAGNETIC FILLER PARTICLES. *Journal of Applied Polymer Science* 34, 2853-2859 (1987).
144. C. Bellan, G. Bossis, Field dependence of viscoelastic properties of MR elastomers. *International Journal of Modern Physics B* 16, 2447-2453 (2002).
145. F. Xu *et al.*, Three-Dimensional Magnetic Assembly of Microscale Hydrogels. *Advanced Materials* 23, 4254-4260 (2011).
146. D. Lorenzo *et al.*, Formation and magnetic manipulation of periodically aligned microchains in thin plastic membranes. *Journal of Applied Physics* 112, (2012).
147. P. Song *et al.*, Mechanical properties of silicone composites reinforced with micron- and nano-sized magnetic particles. *Express Polymer Letters* 7, 546-553 (2013).
148. P. J. Krommenhoek, J. B. Tracy, Magnetic Field-Directed Self-Assembly of Magnetic Nanoparticle Chains in Bulk Polymers. *Particle & Particle Systems Characterization* 30, 759-763 (2013).
149. S. R. Mishra, M. D. Dickey, O. D. Velev, J. B. Tracy, Selective and directional actuation of elastomer films using chained magnetic nanoparticles. *Nanoscale* 8, 1309-1313 (2016).
150. S. Marchi, A. Casu, F. Bertora, A. Athanassiou, D. Fragouli, Highly Magneto-Responsive Elastomeric Films Created by a Two-Step Fabrication Process. *Acs Applied Materials & Interfaces* 7, 19112-19118 (2015).
151. C. Hintze *et al.*, Soft magnetic Elastomers with controllable Stiffness: Experiments and Modelling. *Kgk-Kautschuk Gummi Kunststoffe* 67, 53-59 (2014).
152. D. Le Roy *et al.*, Anisotropic ferromagnetic polymer: A first step for their implementation in microfluidic systems. *AIP Adv.* 6, 6 (2016).
153. D. Fragouli *et al.*, Nanocomposite Pattern-Mediated Magnetic Interactions for Localized Deposition of Nanomaterials. *Acs Applied Materials & Interfaces* 5, 7253-7257 (2013).
154. C. Peters *et al.*, Visible Light Curing of Epon SU-8 Based Superparamagnetic Polymer Composites with Random and Ordered Particle Configurations. *Acs Applied Materials & Interfaces* 7, 193-200 (2015).
155. F. Lin *et al.*, Orientation Control of Graphene Flakes by Magnetic Field: Broad Device Applications of Macroscopically Aligned Graphene. *Advanced Materials* 29, 7 (2017).
156. Y. Ominato, M. Koshino, Orbital magnetism of graphene flakes. *Phys. Rev. B* 87, 8 (2013).
157. L. L. Wu *et al.*, Magnetically Induced Anisotropic Orientation of Graphene Oxide Locked by in Situ Hydrogelation. *Acs Nano* 8, 4640-4649 (2014).
158. B. W. Steinert, D. R. Dean, Magnetic field alignment and electrical properties of solution cast PET-carbon nanotube composite films. *Polymer* 50, 898-904 (2009).
159. Y. Zhang *et al.*, Controlled assembly of Fe3O4 magnetic nanoparticles on graphene oxide. *Nanoscale* 3, 1446-1450 (2011).
160. M. Z. Kassaee, E. Motamedi, M. Majdi, Magnetic Fe3O4-graphene oxide/polystyrene: Fabrication and characterization of a promising nanocomposite. *Chemical Engineering Journal* 172, 540-549 (2011).
161. J. F. Shen *et al.*, One Step Synthesis of Graphene Oxide-Magnetic Nanoparticle Composite. *Journal of Physical Chemistry C* 114, 1498-1503 (2010).
162. H. Le Ferrand *et al.*, Magnetic assembly of transparent and conducting graphene-based functional composites. *Nature Communications* 7, 9 (2016).
163. J. Billaud, F. Bouville, T. Magrini, C. Villevieille, A. R. Studart, Magnetically aligned graphite electrodes for high-rate performance Li-ion batteries. *Nat. Energy* 1, 6 (2016).

164. D. Fragouli *et al.*, Polymeric Films with Electric and Magnetic Anisotropy Due to Magnetically Assembled Functional Nanofibers. *Acs Applied Materials & Interfaces* 6, 4535-4541 (2014).
165. M. A. Correa-Duarte *et al.*, Alignment of carbon nanotubes under low magnetic fields through attachment of magnetic nanoparticles. *Journal of Physical Chemistry B* 109, 19060-19063 (2005).
166. G. Korneva *et al.*, Carbon nanotubes loaded with magnetic particles. *Nano Letters* 5, 879-884 (2005).
167. R. M. Erb, R. Libanori, N. Rothfuchs, A. R. Studart, Composites Reinforced in Three Dimensions by Using Low Magnetic Fields. *Science* 335, 199-204 (2012).
168. R. Libanori, R. M. Erb, A. R. Studart, Mechanics of Platelet-Reinforced Composites Assembled Using Mechanical and Magnetic Stimuli. *Acs Applied Materials & Interfaces* 5, 10794-10805 (2013).
169. R. M. Erb *et al.*, Locally Reinforced Polymer-Based Composites for Elastic Electronics. *Acs Applied Materials & Interfaces* 4, 2860-2864 (2012).
170. R. Libanori, F. B. Reusch, R. M. Erb, A. R. Studart, Ultrahigh Magnetically Responsive Microplatelets with Tunable Fluorescence Emission. *Langmuir* 29, 14674-14680 (2013).
171. H. S. Lim *et al.*, Anisotropically Alignable Magnetic Boron Nitride Platelets Decorated with Iron Oxide Nanoparticles. *Chemistry of Materials* 25, 3315-3319 (2013).
172. O. Trotsenko, A. Tokarev, A. Gruzd, T. Enright, S. Minko, Magnetic field assisted assembly of highly ordered percolated nanostructures and their application for transparent conductive thin films. *Nanoscale* 7, 7155-7161 (2015).
173. R. Gines *et al.*, Ceramic-polymer composites with improved dielectric and tribological properties for semi-active damping. *Composites Part B-Engineering* 72, 80-86 (2015).
174. J. J. Martin, B. E. Fiore, R. M. Erb, Designing bioinspired composite reinforcement architectures via 3D magnetic printing. *Nature Communications* 6, (2015).
175. D. Kokkinis, M. Schaffner, A. R. Studart, Multimaterial magnetically assisted 3D printing of composite materials. *Nature Communications* 6, 10 (2015).
176. D. Carnelli *et al.*, Cement-based composites reinforced with localized and magnetically oriented Al2O3 microplatelets. *Cement and Concrete Research* 78, 245-251 (2015).
177. H. Le Ferrand, F. Bouville, T. P. Niebel, A. R. Studart, Magnetically assisted slip casting of bioinspired heterogeneous composites. *Nature Materials* 14, 1172-+ (2015).
178. S. Ghosh, I. K. Puri, Soft polymer magnetic nanocomposites: microstructure patterning by magnetophoretic transport and self-assembly. *Soft Matter* 9, 2024-2029 (2013).
179. S. Ghosh, M. Tehrani, M. S. Al-Haik, I. K. Puri, Patterning the Stiffness of Elastomeric Nanocomposites by Magnetophoretic Control of Cross-linking Impeder Distribution. *Materials* 8, 474-485 (2015).
180. K. Gizynski, T. Lee, B. A. Grzybowski, Dynamic Self-Assembly of Magnetic/Polymer Composites in Rotating Frames of Reference. *Advanced Materials* 29, 6 (2017).
181. A. R. A. Fattah, S. Ghosh, I. K. Puri, Printing microstructures in a polymer matrix using a ferrofluid droplet. *J. Magn. Magn. Mater.* 401, 1054-1059 (2016).
182. A. R. A. Fattah, S. Ghosh, I. K. Puri, Printing Three-Dimensional Heterogeneities in the Elastic Modulus of an Elastomeric Matrix. *Acs Applied Materials & Interfaces* 8, 11018-11023 (2016).
183. Y. C. Huang *et al.*, Matrix-Free Polymer Nanocomposite Thermoplastic Elastomers. *Macromolecules* 50, 4742-4753 (2017).
184. M. Motornov *et al.*, Field-Directed Self-Assembly with Locking Nanoparticles. *Nano Letters* 12, 3814-3820 (2012).

185. M. G. Zahedi *et al.*, Magnetic-Field-Induced Formation of Superparamagnetic Microwires in Suspension. *Journal of Physical Chemistry C* 118, 28220-28226 (2014).
186. H. Denver, T. Heiman, E. Martin, A. Gupta, D. A. Borca-Tasciuc, Fabrication of polydimethylsiloxane composites with nickel nanoparticle and nanowire fillers and study of their mechanical and magnetic properties. *Journal of Applied Physics* 106, 5 (2009).
187. I. Lisiecki, M. P. Pileni, Ordering at Various Scales: Magnetic Nanocrystals. *Journal of Physical Chemistry C* 116, 3-14 (2012).
188. M. Varon *et al.*, Dipolar Magnetism in Ordered and Disordered Low-Dimensional Nanoparticle Assemblies. *Scientific Reports* 3, 5 (2013).
189. T. P. Almeida *et al.*, Visualized effect of oxidation on magnetic recording fidelity in pseudo-single-domain magnetite particles. *Nature Communications* 5, 6 (2014).
190. T. P. Almeida *et al.*, Observing thermomagnetic stability of nonideal magnetite particles: Good paleomagnetic recorders? *Geophys. Res. Lett.* 41, 7041-7047 (2014).
191. T. P. Almeida *et al.*, Direct visualization of the thermomagnetic behavior of pseudo-single-domain magnetite particles. *Sci. Adv.* 2, 5 (2016).
192. T. P. Almeida *et al.*, Direct observation of the thermal demagnetization of magnetic vortex structures in nonideal magnetite recorders. *Geophys. Res. Lett.* 43, 8426-8434 (2016).
193. C. Phatak, A. K. Petford-Long, M. De Graef, Recent advances in Lorentz microscopy. *Curr. Opin. Solid State Mat. Sci.* 20, 107-114 (2016).
194. T. Prozorov, T. P. Almeida, A. Kovacs, R. E. Dunin-Borkowski, Off-axis electron holography of bacterial cells and magnetic nanoparticles in liquid. *Journal of the Royal Society Interface* 14, 10 (2017).
195. M. T. Lopez-Lopez, J. D. G. Duran, L. Y. Iskakova, A. Y. Zubarev, Mechanics of Magnetopolymer Composites: A Review. *J. Nanofluids* 5, 479-495 (2016).
196. Y. Liu, A. L. Hamon, J. B. Bai, Directly measuring interfacial shear strength between Polymethyl methacrylate and graphene nanoplatelets. *Materials Letters* 182, 244-247 (2016).
197. G. R. Wang *et al.*, Tuning the Interfacial Mechanical Behaviors of Monolayer Graphene/PMMA Nanocomposites. *Acs Applied Materials & Interfaces* 8, 22554-22562 (2016).
198. L. Gong *et al.*, Optimizing the Reinforcement of Polymer-Based Nanocomposites by Graphene. *Acs Nano* 6, 2086-2095 (2012).
199. L. Gong *et al.*, Interfacial Stress Transfer in a Graphene Monolayer Nanocomposite. *Advanced Materials* 22, 2694-+ (2010).
200. C. C. Xu, T. Xue, W. Qiu, Y. L. Kang, Size Effect of the Interfacial Mechanical Behavior of Graphene on a Stretchable Substrate. *Acs Applied Materials & Interfaces* 8, 27099-27106 (2016).
201. T. Jiang, R. Huang, Y. Zhu, Interfacial Sliding and Buckling of Monolayer Graphene on a Stretchable Substrate. *Advanced Functional Materials* 24, 396-402 (2014).
202. J. Jancar, Review of the role of the interphase in the control of composite performance on micro- and nano-length scales. *Journal of Materials Science* 43, 6747-6757 (2008).
203. J. Jancar *et al.*, Current issues in research on structure-property relationships in polymer nanocomposites. *Polymer* 51, 3321-3343 (2010).
204. N. Jouault *et al.*, Well-Dispersed Fractal Aggregates as Filler in Polymer-Silica Nanocomposites: Long-Range Effects in Rheology. *Macromolecules* 42, 2031-2040 (2009).

205. N. Jouault, F. Dalmas, F. Boue, J. Jestin, Multiscale characterization of filler dispersion and origins of mechanical reinforcement in model nanocomposites. *Polymer* 53, 761-775 (2012).
206. J. Jancar, L. Recman, Particle size dependence of the elastic modulus of particulate filled PMMA near its T-g. *Polymer* 51, 3826-3828 (2010).
207. J. Jancar, R. S. Hoy, A. J. Lesser, E. Jancarova, J. Zidek, Effect of Particle Size, Temperature, and Deformation Rate on the Plastic Flow and Strain Hardening Response of PMMA Composites. *Macromolecules* 46, 9409-9426 (2013).
208. J. Jancar, R. S. Hoy, E. Jancarova, J. Zidek, Effect of temperature, strain rate and particle size on the yield stresses and post-yield strain softening of PMMA and its composites. *Polymer* 63, 196-207 (2015).
209. J. F. Moll *et al.*, Mechanical Reinforcement in Polymer Melts Filled with Polymer Grafted Nanoparticles. *Macromolecules* 44, 7473-7477 (2011).
210. J. Oberdisse, Aggregation of colloidal nanoparticles in polymer matrices. *Soft Matter* 2, 29-36 (2006).
211. J. Jancar, Accepted Review. *Progress in Polymer Science*.
212. Y. H. Song, Q. Zheng, Concepts and conflicts in nanoparticles reinforcement to polymers beyond hydrodynamics. *Progress in Materials Science* 84, 1-58 (2016).
213. J. Kalfus, J. Jancar, Relaxation processes in PVAc-HA nanocomposites. *Journal of Polymer Science Part B-Polymer Physics* 45, 1380-1388 (2007).
214. J. Kalfus, J. Jancar, Immobilization of polyvinylacetate macromolecules on hydroxyapatite nanoparticles. *Polymer* 48, 3935-3937 (2007).
215. J. Kalfus, J. Jancar, Elastic response of nanocomposite poly(vinylacetate)-hydroxyapatite with varying particle shape. *Polymer Composites* 28, 365-371 (2007).
216. J. Kalfus, J. Jancar, Viscoelastic response of nanocomposite poly(vinyl acetate)-hydroxyapatite with varying particle shape-dynamic strain softening and modulus recovery. *Polymer Composites* 28, 743-747 (2007).
217. A. Banc *et al.*, Origin of Small-Angle Scattering from Contrast-Matched Nanoparticles: A Study of Chain and Filler Structure in Polymer Nanocomposites. *Macromolecules* 48, 6596-6605 (2015).
218. N. Jouault *et al.*, Polymer Chain Behavior in Polymer Nanocomposites with Attractive Interactions. *Acs Macro Letters* 5, 523-527 (2016).
219. J. Berriot *et al.*, Filler-elastomer interaction in model filled rubbers, a H-1 NMR study. *J. Non-Cryst. Solids* 307, 719-724 (2002).
220. N. Jouault *et al.*, Bound Polymer Layer in Nanocomposites. *Acs Macro Letters* 2, 371-374 (2013).
221. A. Dorigato, M. Sebastiani, A. Pegoretti, L. Fambri, Effect of Silica Nanoparticles on the Mechanical Performances of Poly(Lactic Acid). *J. Polym. Environ.* 20, 713-725 (2012).
222. A. Dorigato, A. Pegoretti, A. Penati, Effect of the polymer-filler interaction on the thermo-mechanical response of polyurethane-clay nanocomposites from blocked prepolymer. *J. Reinf. Plast. Compos.* 30, 325-335 (2011).
223. A. Dorigato, A. Pegoretti, Development and thermo-mechanical behavior of nanocomposite epoxy adhesives. *Polym. Adv. Technol.* 23, 660-668 (2012).
224. A. Dorigato, A. Pegoretti, Fracture behaviour of linear low density polyethylene - fumed silica nanocomposites. *Engineering Fracture Mechanics* 79, 213-224 (2012).
225. A. Dorigato, M. D'Amato, A. Pegoretti, Thermo-mechanical properties of high density polyethylene - fumed silica nanocomposites: effect of filler surface area and treatment. *J. Polym. Res.* 19, 11 (2012).

226. A. Dorigato, Y. Dzenis, A. Pegoretti, Filler aggregation as a reinforcement mechanism in polymer nanocomposites. *Mech Mater* 61, 79-90 (2013).
227. A. Pegoretti, A. Dorigato, A. Penati, Tensile mechanical response of polyethylene-clay nanocomposites. *Express Polymer Letters* 1, 123-131 (2007).
228. F. Bondioli, A. Dorigato, P. Fabbri, M. Messori, A. Pegoretti, High-density polyethylene reinforced with submicron titania particles. *Polymer Engineering and Science* 48, 448-457 (2008).
229. A. Dorigato, A. Pegoretti, A. Penati, Linear low-density polyethylene/silica micro- and nanocomposites: dynamic rheological measurements and modelling. *Express Polymer Letters* 4, 115-129 (2010).
230. D. Pedrazzoli, A. Pegoretti, K. Kalaitzidou, Interfacial interactions in silica-reinforced polypropylene nanocomposites and their impact on the mechanical properties. *Polymer Composites* 37, 2018-2026 (2016).
231. A. Hashemi *et al.*, Enhanced Glassy State Mechanical Properties of Polymer Nanocomposites via Supramolecular Interactions. *Nano Letters* 15, 5465-5471 (2015).
232. J. Berriot, H. Montes, F. Lequeux, D. Long, P. Sotta, Evidence for the shift of the glass transition near the particles in silica-filled elastomers. *Macromolecules* 35, 9756-9762 (2002).
233. S. Merabia, P. Sotta, D. R. Long, A Microscopic Model for the Reinforcement and the Nonlinear Behavior of Filled Elastomers and Thermoplastic Elastomers (Payne and Mullins Effects). *Macromolecules* 41, 8252-8266 (2008).
234. M. Tauban, J. Y. Delannoy, P. Sotta, D. R. Long, Effect of Filler Morphology and Distribution State on the Linear and Nonlinear Mechanical Behavior of Nanofilled Elastomers. *Macromolecules* 50, 6369-6384 (2017).
235. R. Scotti *et al.*, Shape controlled spherical (0D) and rod-like (1D) silica nanoparticles in silica/styrene butadiene rubber nanocomposites: Role of the particle morphology on the filler reinforcing effect. *Polymer* 55, 1497-1506 (2014).
236. Z. Zheng, Y. H. Song, R. Q. Yang, Q. Zheng, Direct Evidence for Percolation of Immobilized Polymer Layer around Nanoparticles Accounting for Sol-Gel Transition in Fumed Silica Dispersions. *Langmuir* 31, 13478-13487 (2015).
237. T. Koga *et al.*, New insight into hierarchical structures of carbon black dispersed in polymer matrices: A combined small-angle scattering study. *Macromolecules* 41, 453-464 (2008).
238. D. Yamaguchi *et al.*, Hierarchically Self-Organized Dissipative Structures of Filler Particles in Poly(styrene-ran-butadiene) Rubbers. *Macromolecules* 50, 7739-7759 (2017).
239. G. P. Baeza *et al.*, Multiscale Filler Structure in Simplified Industrial Nanocomposite Silica/SBR Systems Studied by SAXS and TEM. *Macromolecules* 46, 317-329 (2013).
240. Y. C. Lin, H. L. Chen, T. Hashimoto, S. A. Chen, Mechanism of Hierarchical Structure Formation of Polymer/Nanoparticle Hybrids. *Macromolecules* 49, 7535-7550 (2016).
241. A. C. Genix, J. Oberdisse, Nanoparticle self-assembly: from interactions in suspension to polymer nanocomposites. *Soft Matter* 14, 5161-5179 (2018).
242. T. A. Witten, M. Rubinstein, R. H. Colby, REINFORCEMENT OF RUBBER BY FRACTAL AGGREGATES. *Journal De Physique Ii* 3, 367-383 (1993).
243. D. W. Schaefer, R. S. Justice, How nano are nanocomposites? *Macromolecules* 40, 8501-8517 (2007).
244. S. N. Raja *et al.*, Tetrapod Nanocrystals as Fluorescent Stress Probes of Electrospun Nanocomposites. *Nano Letters* 13, 3915-3922 (2013).
245. S. N. Raja *et al.*, Mechanisms of Local Stress Sensing in Multifunctional Polymer Films Using Fluorescent Tetrapod Nanocrystals. *Nano Letters* 16, 5060-5067 (2016).

246. A. Bouty *et al.*, Nanofiller Structure and Reinforcement in Model Silica/Rubber Composites: A Quantitative Correlation Driven by Interfacial Agents. *Macromolecules* 47, 5365-5378 (2014).
247. L. X. Song *et al.*, Visualizing the Toughening Mechanism of Nanofiller with 3D X-ray Nano-CT: Stress-Induced Phase Separation of Silica Nanofiller and Silicone Polymer Double Networks. *Macromolecules* 50, 7249-7257 (2017).
248. X. D. Li, Z. H. Xu, R. Z. Wang, In situ observation of nanograin rotation and deformation in nacre. *Nano Letters* 6, 2301-2304 (2006).
249. S. K. Friedlander, K. Ogawa, M. Ullmann, Elastic behavior of nanoparticle chain aggregates: A hypothesis for polymer-filler behavior. *Journal of Polymer Science Part B-Polymer Physics* 38, 2658-2665 (2000).
250. Y. J. Suh, S. V. Prikhodko, S. K. Friedlander, Nanostructure manipulation device for transmission electron microscopy: application to titania nanoparticle chain aggregates. *Microsc. microanal.* 8, 497-501 (2002).
251. Y. J. Suh, S. K. Friedlander, Origins of the elastic behavior of nanoparticle chain aggregates: Measurements using nanostructure manipulation device. *Journal of Applied Physics* 93, 3515-3523 (2003).
252. W. Z. Rong, A. E. Pelling, A. Ryan, J. K. Gimzewski, S. K. Friedlander, Complementary TEM and AFM force spectroscopy to characterize the nanomechanical properties of nanoparticle chain aggregates. *Nano Letters* 4, 2287-2292 (2004).
253. R. Bandyopadhyaya, W. Z. Rong, S. K. Friedlander, Dynamics of chain aggregates of carbon nanoparticles in isolation and in polymer films: Implications for nanocomposite materials. *Chemistry of Materials* 16, 3147-3154 (2004).
254. A. Dalis, S. K. Friedlander, Molecular dynamics simulations of the straining of nanoparticle chain aggregates: the case of copper. *Nanotechnology* 16, S626-S631 (2005).
255. W. Z. Rong, W. Q. Ding, L. Madler, R. S. Ruoff, S. K. Friedlander, Mechanical properties of nanoparticle chain aggregates by combined AFM and SEM: Isolated aggregates and networks. *Nano Letters* 6, 2646-2655 (2006).
256. M. Sarikaya *et al.*, Biomimetic model of a sponge-spicular optical fiber - mechanical properties and structure. *Journal of Materials Research* 16, 1420-1428 (2001).
257. U. G. K. Wegst, H. Bai, E. Saiz, A. P. Tomsia, R. O. Ritchie, Bioinspired structural materials. *Nature Materials* 14, 23-36 (2015).
258. U. G. K. Wegst, M. F. Ashby, The mechanical efficiency of natural materials. *Philos. Mag.* 84, 2167-2181 (2004).
259. M. A. Meyers, P. Y. Chen, A. Y. M. Lin, Y. Seki, Biological materials: Structure and mechanical properties. *Progress in Materials Science* 53, 1-206 (2008).
260. M. A. Meyers, P. Y. Chen, M. I. Lopez, Y. Seki, A. Y. M. Lin, Biological materials: A materials science approach. *Journal of the Mechanical Behavior of Biomedical Materials* 4, 626-657 (2011).
261. D. Y. Borin, G. V. Stepanov, S. Odenbach, in *13th International Conference on Electrorheological Fluids and Magnetorheological Suspensions (ERMR)*, U. Gazi, I. F. M. D. D. G. Tech Univ Dresden, Eds. (Iop Publishing Ltd, Gazi Univ, Ankara, TURKEY, 2012), vol. 412.
262. Z. Varga, G. Filipcsei, M. Zrinyi, Magnetic field sensitive functional elastomers with tuneable elastic modulus. *Polymer* 47, 227-233 (2006).
263. Y. Han, W. Hong, L. A. E. Faidley, Field-stiffening effect of magneto-rheological elastomers. *Int. J. Solids Struct.* 50, 2281-2288 (2013).

264. P. S. Antonel *et al.*, Magnetic and elastic properties of CoFe2O4- polydimethylsiloxane magnetically oriented elastomer nanocomposites. *Journal of Applied Physics* 110, 8 (2011).
265. J. L. Mietta *et al.*, Anisotropic Magnetoresistance and Piezoresistivity in Structured Fe3O4-Silver Particles in PDMS Elastomers at Room Temperature. *Langmuir* 28, 6985-6996 (2012).
266. B. Torre *et al.*, "Magnetic Force Microscopy and Energy Loss Imaging of Superparamagnetic Iron Oxide Nanoparticles". *Scientific Reports* 1, 8 (2011).
267. K. Keshoju, L. Sun, Mechanical characterization of magnetic nanowire-polydimethylsiloxane composites. *Journal of Applied Physics* 105, 5 (2009).
268. K. Ikemura, K. Ichizawa, M. Yoshida, S. Ito, T. Endo, UV-VIS spectra and photoinitiation behaviors of acylphosphine oxide and bisacylphosphine oxide derivatives in unfilled, light-cured dental resins. *Dent. Mater. J.* 27, 765-774 (2008).
269. M. J. Donahue, D. G. Porter. (National Institute of Standards and Technology, 1999).
270. T. Nardi *et al.*, UV-cured transparent magnetic polymer nanocomposites. *Polymer* 54, 4472-4479 (2013).
271. V. Melinte *et al.*, Preparation and properties of photopolymerized hybrid composites with covalently attached magnetite nanoparticles. *Chemical Engineering Journal* 259, 542-551 (2015).
272. C. Xu, K. Ohno, V. Ladmiral, R. J. Composto, Dispersion of polymer-grafted magnetic nanoparticles in homopolymers and block copolymers. *Polymer* 49, 3568-3577 (2008).
273. A. S. Robbes *et al.*, Homogeneous Dispersion of Magnetic Nanoparticles Aggregates in a PS Nanocomposite: Highly Reproducible Hierarchical Structure Tuned by the Nanoparticles' Size. *Macromolecules* 43, 5785-5796 (2010).
274. Y. Jiao, P. Akcora, Assembly of Polymer-Grafted Magnetic Nanoparticles in Polymer Melts. *Macromolecules* 45, 3463-3470 (2012).
275. M. Ashjari, A. R. Mahdavian, N. G. Ebrahimi, Y. Mosleh, Efficient Dispersion of Magnetite Nanoparticles in the Polyurethane Matrix Through Solution Mixing and Investigation of the Nanocomposite Properties. *J. Inorg. Organomet. Polym. Mater.* 20, 213-219 (2010).
276. J. Zidek, J. Kucera, J. Jancar, Nearest Particle Distance and the Statistical Distribution of Agglomerates from a Model of a Finite Set of Particles. *Cmc-Computers Materials & Continua* 24, 183-208 (2011).
277. J. Zidek, Personal Discussion. (2018).
278. S. Melle, O. G. Calderon, M. A. Rubio, G. G. Fuller, Rotational dynamics in dipolar colloidal suspensions: video microscopy experiments and simulations results. *Journal of Non-Newtonian Fluid Mechanics* 102, 135-148 (2002).
279. P. Dominguez-Garcia, S. Melle, J. M. Pastor, M. A. Rubio, Scaling in the aggregation dynamics of a magnetorheological fluid. *Physical Review E* 76, 13 (2007).
280. J. W. Swan *et al.*, Multi-scale kinetics of a field-directed colloidal phase transition. *Proceedings of the National Academy of Sciences of the United States of America* 109, 16023-16028 (2012).
281. R. A. Landa *et al.*, Magnetic and elastic anisotropy in magnetorheological elastomers using nickel-based nanoparticles and nanochains. *Journal of Applied Physics* 114, 11 (2013).
282. C. Chevigny, N. Jouault, F. Dalmas, F. Boue, J. Jestin, Tuning the Mechanical Properties in Model Nanocomposites: Influence of the Polymer-Filler Interfacial Interactions. *Journal of Polymer Science Part B-Polymer Physics* 49, 781-791 (2011).

283. F. J. Li, S. D. Zhang, J. Z. Liang, J. Z. Wang, Effect of polyethylene glycol on the crystallization and impact properties of polylactide-based blends. *Polym. Adv. Technol.* 26, 465-475 (2015).
284. K. W. Putz, M. J. Palmeri, R. B. Cohn, R. Andrews, L. C. Brinson, Effect of cross-link density on interphase creation in polymer nanocomposites. *Macromolecules* 41, 6752-6756 (2008).
285. Y. Zare, H. Garmabi, Analysis of Tensile Modulus of PP/Nanoclay/CaCO3 Ternary Nanocomposite Using Composite Theories. *Journal of Applied Polymer Science* 123, 2309-2319 (2012).
286. D. Chicot *et al.*, Mechanical properties of magnetite (Fe3O4), hematite (alpha-Fe2O3) and goethite (alpha-FeO center dot OH) by instrumented indentation and molecular dynamics analysis. *Materials Chemistry and Physics* 129, 862-870 (2011).
287. R. Hentschke, The Payne effect revisited. *Express Polymer Letters* 11, 278-292 (2017).
288. P. Sotta *et al.*, Nonentropic Reinforcement in Elastomer Nanocomposites. *Macromolecules* 50, 6314-6322 (2017).
289. E. Guth, THEORY OF FILLER REINFORCEMENT. *Journal of Applied Physics* 16, 20-25 (1945).
290. H. M. Smallwood, Limiting Law of the Reinforcement of Rubber. *Journal of Applied Physics* 15, 758-766 (1944).
291. G. Huber, T. A. Vilgis, On the mechanism of hydrodynamic reinforcement in elastic composites. *Macromolecules* 35, 9204-9210 (2002).
292. G. Heinrich, M. Kluppel, T. A. Vilgis, Reinforcement of elastomers. *Curr. Opin. Solid State Mat. Sci.* 6, 195-203 (2002).
293. F. Lu, H. H. Kausch, W. J. Cantwell, M. Fischer, The effect of crosslink density on the fracture toughness of core-shell modified epoxy resins. *J. Mater. Sci. Lett.* 15, 1018-1021 (1996).
294. H. G. H. van Melick, L. E. Govaert, H. E. H. Meijer, On the origin of strain hardening in glassy polymers. *Polymer* 44, 2493-2502 (2003).
295. H. L. Xu, Y. H. Song, Q. X. Zhang, Q. Zheng, Contributions of silica network and interfacial fraction in reinforcement and Payne effect of polypropylene glycol nanocomposites. *Polymer* 138, 139-145 (2018).
296. H. Montes, F. Lequeux, J. Berriot, Influence of the glass transition temperature gradient on the nonlinear viscoelastic behavior in reinforced elastomers. *Macromolecules* 36, 8107-8118 (2003).
297. R. Hentschke, J. Hager, N. W. Hojdis, Molecular Modeling Approach to the Prediction of Mechanical Properties of Silica-Reinforced Rubbers. *Journal of Applied Polymer Science* 131, 9 (2014).
298. J. Hager, R. Hentschke, N. W. Hojdis, H. A. Karimi-Varzaneh, Computer Simulation of Particle-Particle Interaction in a Model Polymer Nanocomposite. *Macromolecules* 48, 9039-9049 (2015).
299. J. Meyer, R. Hentschke, J. Hager, N. W. Hojdis, H. A. Karimi-Varzaneh, Molecular Simulation of Viscous Dissipation due to Cyclic Deformation of a Silica-Silica Contact in Filled Rubber. *Macromolecules* 50, 6679-6689 (2017).
300. J. Jancar, The Thickness Dependence of Elastic Modulus of Organosilane Interphases. *Polymer Composites* 29, 1372-1377 (2008).
301. H. Mortazavian, C. J. Fennell, F. D. Blum, Structure of the Interfacial Region in Adsorbed Poly(vinyl acetate) on Silica. *Macromolecules* 49, 298-307 (2016).
302. S. Y. Kim, C. F. Zukoski, Molecular Weight Effects on Particle and Polymer Microstructure in Concentrated Polymer Solutions. *Macromolecules* 46, 6634-6643 (2013).

303. B. J. Anderson, C. F. Zukoski, Rheology and Microstructure of an Unentangled Polymer Nanocomposite Melt. *Macromolecules* 41, 9326-9334 (2008).
304. H. Mortazavian, C. J. Fennell, F. D. Blum, Surface Bonding Is Stronger for Poly(methyl methacrylate) than for Poly(vinyl acetate). *Macromolecules* 49, 4211-4219 (2016).
305. J. Moll, S. K. Kumar, Glass Transitions in Highly Attractive Highly Filled Polymer Nanocomposites. *Macromolecules* 45, 1131-1135 (2012).
306. Q. Chen *et al.*, Mechanical Reinforcement of Polymer Nanocomposites from Percolation of a Nanoparticle Network. *Acs Macro Letters* 4, 398-402 (2015).
307. A. N. Rissanou *et al.*, Structural and Conformational Properties of Poly(ethylene oxide)/Silica Nanocomposites: Effect of Confinement. *Macromolecules* 50, 6273-6284 (2017).
308. G. Chen *et al.*, Mechanical and dynamic properties of resin blend and composite systems: A molecular dynamics study. *Composite Structures* 190, 160-168 (2018).
309. J. S. Meth, S. R. Lustig, Polymer interphase structure near nanoscale inclusions: Comparison between random walk theory and experiment. *Polymer* 51, 4259-4266 (2010).
310. A. Mujtaba *et al.*, Detection of Surface-Immobilized Components and Their Role in Viscoelastic Reinforcement of Rubber-Silica Nanocomposites. *Acs Macro Letters* 3, 481-485 (2014).
311. A. Mujtaba *et al.*, Mechanical Properties and Cross-Link Density of Styrene-Butadiene Model Composites Containing Fillers with Bimodal Particle Size Distribution. *Macromolecules* 45, 6504-6515 (2012).
312. S. W. Wu, M. Qiu, Z. H. Tang, B. C. Guo, Interphase Percolation Mechanism Underlying Elastomer Reinforcement. *Journal of Physical Chemistry C* 121, 28594-28603 (2017).
313. B. Bar-On, H. D. Wagner, Structural motifs and elastic properties of hierarchical biological tissues - A review. *J. Struct. Biol.* 183, 149-164 (2013).
314. B. Bar-On, H. D. Wagner, The emergence of an unusual stiffness profile in hierarchical biological tissues. *Acta Biomater.* 9, 8099-8109 (2013).
315. B. Bar-On, H. D. Wagner, New insights into the Young's modulus of staggered biological composites. *Mater. Sci. Eng. C-Mater. Biol. Appl.* 33, 603-607 (2013).
316. J. C. Halpin Affdl, J. L. Kardos, The Halpin-Tsai equations: A review. 16, 344–352 (1976).
317. P. Y. J. Tsai, S. Ghosh, P. D. Wu, I. K. Puri, Tailoring Material Stiffness by Filler Particle Organization. *Acs Applied Materials & Interfaces* 8, 27449-27453 (2016).

Author's publications and other outputs

Scientific conferences:

CEITEC PhD retreat, Valtice, 2015 – Active participant with a poster and abstract in book of abstracts: *Short fiber reinforced thermoplastic composites*

Chemistry & Life 2015, Brno, 2015 – Active participant with a poster, abstract in book of abstracts and article in conference proceeding book: *Force-assembled Fe_3O_4 particle chains in polyurethane matrix*

Creating Life in 3D, Brno, 2015 - Active participant with a poster: *Force-assembled Fe_3O_4 particle chains in polyurethane matrix*

Structure and Dynamics of Polymer Nanocomposites, Montpellier, 2015, – Active participant with a presentation and abstract in book of abstracts: *Magnetic force-assembled polymer nanocomposites*

CEITEC PhD retreat 2, Telc, 2017 – Active participant with a poster and abstract in book of abstracts: *Magnetic field directed self-assembly as route for biomimetics*

Deformation, yield and fracture of polymers, Rolduc, 2018 – Active participant with a poster and abstract in book of abstracts: *Mechanical anisotropy induced by magnetically assembled particle fibrous assemblies in photopolymer matrix*

Research projects:

Magnetic field directed self-assembly as route for bottom-up build-up approach inspired by nature – research team leader

Control of nanoparticle self-assembly in polymer liquids and effect of nanostructure on the thermo-mechanical properties of resulted nanocomposites – member of research team

Nízkohustotní funkční nanokompozity (GAČR) – research team member

Výzkum odpadních termoplastů (TAČR) – research team member

Mechanismy a kinetika samouspořádávání nanočástic v hierarchických polymerních kompozitech (GAČR) – research team member

Publications:

Zboncak, M.; Ondreas, F.; Jancar, J. Force-Assembled Fe_3O_4 Particle Chains in Polyurethane Matrix. *Materials Science Forum,* 221-225 (2016).

P. Lepcio, F. Ondreas, K. Zarybnicka, M. Zboncak, O. Caha, J. Jancar, Bulk polymer nanocomposites with preparation protocol governed nanostructure: the origin and properties of aggregates and polymer bound clusters. *Soft Matter* 14, 2094-2103 (2018).

M. Zboncak, J. Jancar, Toughening of PMMA by short poly(p-phenylene-2,6-benzobisoxazole) fibers. *Express Polymer Letters* 12, 753-766 (2018).

Internships:

TU Wien, Institute of Materials Science and Technology – Research group of Jürgen Stampfl

Weizmann Institute of Science, Materials and Interfaces – Research group of Daniel H. Wagner

Pedagogical experience:

Participation on the teaching of the course Composite materials and their technologies II